NASA CR-174995

TURBINE BLADE AND VANE HEAT FLUX SENSOR DEVELOPMENT

PHASE II - FINAL REPORT

by W.H. Atkinson, M.A. Cyr, and R.R. Strange

United Technologies Corporation
Pratt & Whitney Group
Engineering Division

October 1985

(NASA-CR-174995) TURBINE BLADE AND VANE HEAT FLUX SENSOR DEVELOPMENT, PHASE 2 Final Report, Sep. 1982 - Jul. 1985 (Pratt and Whitney Aircraft Group) 85 p HC A05/MF A01 CSCL 21E G3/07

N86-12226

Unclas
04829

Prepared for

NATIONAL AERONAUTICS AND SPACE ADMINISTRATION

NASA LEWIS RESEARCH CENTER
21000 BROOKPARK ROAD
CLEVELAND, OHIO 44135

Contract NAS3-23529

NASA

1. REPORT NO.	2. GOVERNMENT AGENCY	3. RECIPIENT'S CATALOG NO.
CR-174995	NASA-Lewis	

4. TITLE AND SUBTITLE	5. REPORT DATE
Turbine Blade and Vane Heat Flux Sensor Development Phase II - Final Report	October 1985
	6. PERFORMING ORG. CODE
7. AUTHOR(S) William H. Atkinson, Marcia A. Cyr Richard R. Strange	8. PERFORMING ORG. REPT. NO. PWA 5914-39
9. PERFORMING ORG. NAME AND ADDRESS UNITED TECHNOLOGIES CORPORATION Pratt & Whitney Group Engineering Division	10. WORK UNIT NO.
	11. CONTRACT OR GRANT NO. NAS3-23529
12. SPONSORING AGENCY NAME AND ADDRESS National Aeronautics and Space Administration Lewis Research Center 21000 Brookpark Road	13. TYPE REPT./PERIOD COVERED 9/82 - 7/85
	14. SPONSORING AGENCY CODE

15. SUPPLEMENTARY NOTES

16. ABSTRACT:

This report covers Phase II of a two-phase program which had as its objective the development of heat flux sensors for gas turbine blades and vanes and demonstration of heat transfer measurement methods. In Phase I, two heat flux sensor types were identified and fabricated: embedded thermocouple sensors and Gardon gauge sensors.

In Phase II, reported herein, the performance of these heat flux sensors fabricated in Phase I was evaluated in a cylinder in cross flow experiment and compared with two other heat flux measurement methods, the slug calorimeter and a dynamic method based on fluctuating gas and surface temperature. Two cylinders, each instrumented with an embedded thermocouple sensor, a Gardon gauge, and a slug calorimeter, were fabricated. Each sensor type was calibrated using a quartz lamp bank facility. The instrumented cylinders were then tested in an atmospheric pressure combustor rig at conditions up to gas stream temperatures of 1700K and velocities to Mach 0.74. The test data was then compared to other measurements and analytical prediction.

17. KEY WORDS (SUGGESTED BY AUTHOR(S))	18. DISTRIBUTION STATEMENT
Heat Flux Sensors Turbine Blade and Vane Heat Transfer Heat Transfer Coefficients Cylinder in Cross Flow	Unclassified - Unlimited

19. SECURITY CLASS THIS (REPT)	20. SECURITY CLASS THIS (PAGE)	21. NO. PGS	22. PRICE *

* For sale by the National Technical Information Service, Springfield, VA 22161

FOREWORD

This Final Report presents the results of a development program conducted by Pratt & Whitney to develop heat flux sensors suitable for installation in hot section airfoils of advanced aircraft gas turbine engines. This effort was conducted for the National Aeronautics and Space Administration under Contract NAS3-23529. This program was conducted under the direction of Mr. Raymond Holanda who served as the NASA Program Manager. The Program Manager at United Technologies Corporation, Pratt & Whitney, was Mr. William H. Atkinson. Dick Strange and Marcia Cyr contributed significantly to the analytical effort. The cylinders were instrumented by Bob Guenard. Fred Fries and Bob Williston ran most of the cylinder in cross flow tests.

TABLE OF CONTENTS

LIST OF ILLUSTRATIONS

LIST OF ILLUSTRATIONS (continued)

LIST OF ILLUSTRATIONS (continued)

LIST OF ILLUSTRATIONS (continued)

LIST OF TABLES

SECTION 1.0
SUMMARY

The overall objective of this two phase program is to develop heat flux sensors suitable for installation in hot section airfoils of advanced aircraft gas turbine engines. The first phase consisted of design, fabrication, calibration and testing of two heat flux sensor types (Ref. 21). The second phase, which is covered in this report, tested these sensors and other sensor types in a cylinder in cross flow experiment conducted in an atmospheric pressure combustor test rig to evaluate the performance of the sensors.

A literature survey conducted into cylinder-in-cross-flow tests and measurement methods indicated testing of heat flux sensors was mostly done at low temperatures and low Mach numbers. Although this information provided the basis for analytical predictions in the current test program, it was not directly applicable since the combustor exit environment has higher temperatures and higher Mach numbers. Sensor types developed under phase I were used as well as a transient slug sensor type. The results from these sensors were compared to other measurements and with analytical predictions. The results for the cylinder-in-cross-flow test program are identified below:

- Sensor types developed under Phase I demonstrated the capability to withstand hot section environmental conditions.

- Sensor types from Phase I showed reasonable agreement in heat flux measurements.

- Non-one-dimensional heat flow was shown to present serious problems in the interpretation of the heat flux sensor data.

- The results from the sputtered thermocouple sensors were unrealistically high and possible causes were identified.

SECTION 2.0
INTRODUCTION

Designing durable turbine airfoils which use a minimum amount of cooling air requires detailed knowledge of heat flux characteristics within the hot section of advanced aircraft gas turbine engines. To acquire this knowledge, accurate and durable heat flux sensors need to be developed. These sensors would provide a diagnostic tool enabling the modification and verification of analytical procedures used to design turbine airfoils having improved durability and longer life. These, in turn, would promote a longer component life while minimizing the amount of cooling required, thus advancing fuel efficiency and reducing maintenance costs.

Considerable development has been done on both low and high temperature heat flux sensors for such diverse purposes as basic boundary layer experiments, solar power and energy conservation investigations, research on thermal protection systems for advanced aircraft and spacecraft, and application in advanced aircraft combustors. However, none of these applications combines the requirement for materials compatibility, miniaturization, and survivability in a hostile environment that is necessary for a viable turbine airfoil heat flux sensor. Due to the inherent limitations of current sensors, it has been impossible to collect hard empirical data relating to the heat transfer taking place in operating turbine airfoils in aircraft gas turbine engines. As an undesirable alternative, investigators have been forced to rely on heat flux predictions derived from ad hoc analytical models, which are in themselves, unverifiable due to the very lack of empirical data.

As part of the HOST program, development of heat flux sensors suitable for use on turbine airfoils was initiated at Pratt & Whitney under Contract NAS3-23529. The objectives of this program were to develop heat flux sensors for gas turbine blades and vanes and demonstrate a variety of heat transfer measurement methods on a test piece of simple geometry in an atmospheric pressure combustor rig. The second phase of this program, the cylinder in cross flow experiment, which is reported herein, was designed to demonstrate the performance of various heat transfer measurement techniques by determining the heat transfer coefficient to a cooled cylinder in an atmospheric pressure combustor rig. The rig was characterized and heat flux sensor data was obtained up to gas stream temperature of 1700K and velocities to Mach 0.74. The experiment included various methods for measuring heat flux and determining the heat transfer coefficient:

1. A method based on measuring the temperature difference across an internally cooled wall(Steady - state sensors including the embedded thermocouple and Gardon gauge sensors developed under Phase I of this contract).

2. A method based on a step change in heat flux (slug calorimeter)

3. A method based on fluctuating gas and surface temperature measurements using a dynamic gas temperature probe of dual wire design and a sputtered thin film surface thermocouple.

SECTION 3.0
SURVEY AND EVALUATION OF CYLINDER IN CROSS FLOW EXPERIMENTS

A survey was conducted to identify various heat transfer measurement techniques that could be used for the cylinder in cross flow experiment. This survey consisted of a literature search, consultation with authorities in the field of heat transfer measurements, and a review of state-of-the-art sensors.

LITERATURE SURVEY

The United Technologies Research Center Library was used to conduct a computer assisted literature survey on heat-transfer measurements for cylinder in cross flow experiments as well as the modeling of those experiments. A complete listing of the literature reviewed is contained in Appendix A.

As described in the literature, most testing was conducted at low temperatures in wind tunnels with grids placed upstream of the cylinders to generate free stream turbulence. The cylinders were typically heated with strip heaters to permit measurement of heat transfer rates. Dils and Follansbee (Ref. 4), however, conducted the experiment with an unheated cylinder downstream of a combustor. In both types of experiments, gas temperature fluctuations were measured by means of fine wire thermocouples and surface temperatures were measured with embedded thermocouples (Ref. 19) or sputtered thermocouples (Ref. 4). Velocity measurements of the exhaust gas were made by laser velocimetry (Ref. 4) and hot wire anemometry (Refs. 19, 12). From these measurements, calculations can be made for the turbulent shear stress of the cylinder, frequency spectra, and boundary layer shape parameters (Ref. 28).

Heat flux to cylinders in cross flow is influenced strongly by the free stream turbulence (Ref. 10). As turbulence is increased, the heat transfer coefficient increases. This correlation can be found by using the parameter $TuRe^{1/2}$ where Tu is the turbulence intensity and Re is the Reynolds number as shown in Figure 1 (Ref. 7). These observations have been confirmed at low Reynolds numbers in cold flows as well as at high Reynolds numbers in hot flows. The heat transfer coefficients found in hot flows are uniformly higher than those found in low-turbulence cold flows.

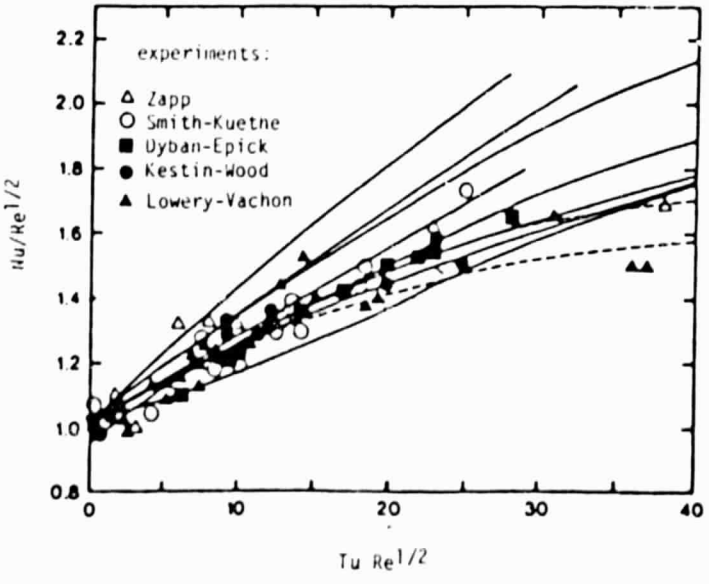

Figure 1 Effect of Turbulence Intensity on Heat Transfer-Adapted from Reference 7

CONSULTATIONS

Discussions in the fields of heat flux and fluid flow measurements were held with authorities from educational institutions, industry and the government. None were aware of the existence of commercially available heat flux sensors that would survive in the gas turbine hot section.

SURVEY OF STATE-OF-THE-ART INSTRUMENTATION

In parallel with the literature survey, a survey was conducted of the commercially available instrumentation for heat flux measurements in an atmospheric pressure combustor rig. This survey showed that there were no commercially available sensors that possessed the characteristics of high temperature capability, extreme ruggedness, nonperturbing qualities, and small size demanded by this application. However, it was found that the heat transfer coefficient could be obtained by combining the fine dual wire thermocouple probe and the sputtered thermocouple surface temperature sensor, two experimental methods that were developed at Pratt & Whitney under NASA contracts NAS3-22002 and NAS3-23154.

SECTION 4.0
HEAT FLUX SENSOR DESIGN

Following evaluation of various sensor types, two types of steady state heat flux sensors were chosen by NASA to be designed for use in turbine blades and vanes and for the cylinder in cross flow experiment. These were embedded thermocouple sensors and Gardon gauge sensors. The development of these sensors is described in Reference 22 (NASA contractor report CR-168297). The third sensor, a slug calorimeter sensor for transient measurements, was chosen to be included in the cylinder.

CHOICE OF TEST GEOMETRY

For the atmospheric pressure combustor test, a simple geometry was selected to allow comparison with theoretical calculations and published data. Published test and theoretical data was available only for simple geometries such as plates in channel flow or cylinders and spheres in cross flow. A cylindrical test piece was chosen because: 1) cylinders are well documented in the literature, 2) they could be easily supported in front of a combustor and 3) they are representative of airfoil leading edge geometries. The cylinder size was determined by trade offs among many factors. Small cylinders would maximize the heat transfer coefficient, minimize combustor blockage and minimize Reynolds number which, in turn, minimizes the turbulence effects. However, larger cylinder sizes were favored due to construction considerations. Angular resolution of the sensors also decreased with decreasing cylinder diameter. Therefore, if the sensor is required to cover no more than $\pm$ 6 degrees of the cylinder surface and a minimum practical sensor diameter of 1.5 mm is used, then at least a 1.5 cm diameter cylinder is needed. A compromise was reached with Hastelloy-X tubing, which has an outside diameter of 1.6 cm and a wall thickness of 1.5 mm.

Calculations were performed to determine the necessary internal heat transfer coefficient to cool the cylinder. Based on those calculations the test cylinder was designed to be cooled by channel flow to increase the internal heat transfer coefficient. This was accomplished by inserting an internal tube with a 0.8 cm outside diameter into the center of the larger cylinder which restricted the coolant flow to an annulus.

Mechanical Design

Embedded thermocouple sensors require installation of lead wires in both the hot and cold side of the tube wall. These sensors were designed with three single conductor swaged wires to maximize the thermocouple wire size to increase durability while keeping the required slots small. Figure 2 illustrates the design for the embedded thermocouple sensors. In this design, both an Alumel and Chromel wire are embedded on the cold side of the tube and an Alumel wire is embedded on the hot side. The sensor output is obtained as a differential signal from the Alumel wires. The Chromel/Alumel thermocouple yields a reference temperature.

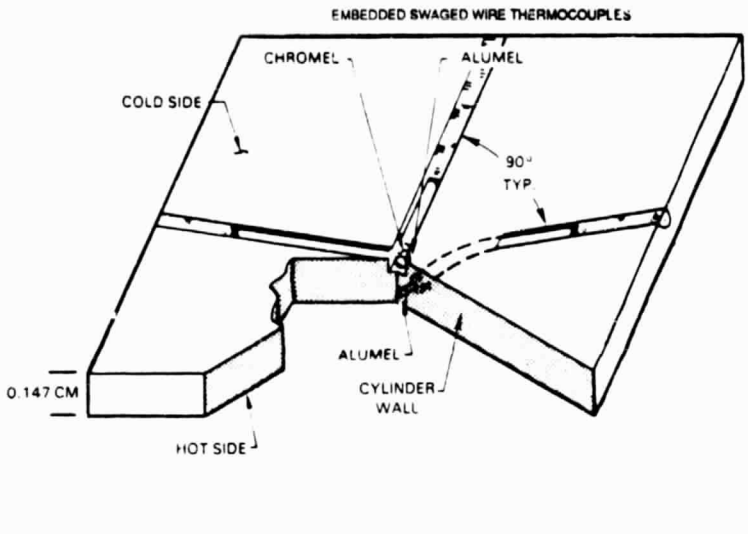

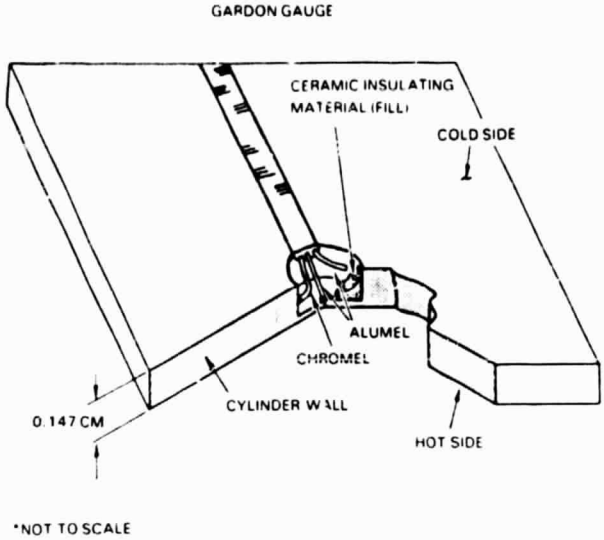

*NOT TO SCALE

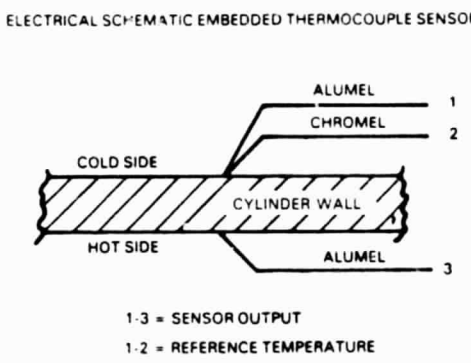

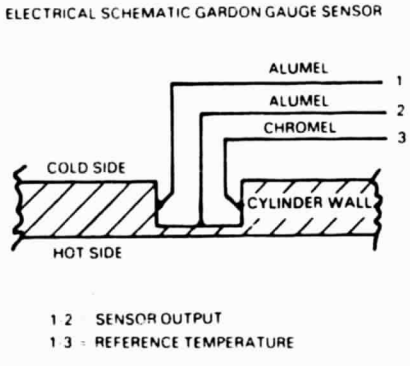

Figure 2 Schematic of the Embedded Thermocouple Heat Flux Sensor

Figure 3 Schematic of the Gardon Gauge Heat Flux Sensor

The Gardon gauge sensors require installation of lead wires on only the cold side of the tube. To minimize machining and maximize durability, these sensors were designed with a single sheathed three conductor cable. Figure 3 shows a schematic of the Gardon gauge sensors. In this design, two Alumel wires and one Chromel wire are installed in a single sheath that is embedded in the cold side surface. This unique three conductor cable was produced to our specifications by Idaho Labs[1].

The sensor was formed by electro-machining the cavity into the tube. One Alumel lead was attached to the bottom center of the cavity; the other Alumel lead and the Chromel lead were attached to the wall of the cavity near the bottom. Sensor output was obtained from the two Alumel wires, while a reference temperature was obtained from the Chromel and Alumel wires attached to the wall. The cavity made for the Gardon gauge was filled with a ceramic cement which provided aerodynamic integrity on the cold side as well as support and oxidation protection for the fine thermocouple wires.

---

[1] Idaho Laboratories Corporation
2101 Hemmert Avenue
Idaho Falls, ID 83401

The slug calorimeter sensors required installation of lead wires only on the cold side of the tube. Thermocouple wire size was maximized to increase durability by using two single conductor swaged wires. Figure 4 shows a schematic for the slug calorimeter sensor. In this design, a slug was formed from the base material by eloxing a ring around the sensing area. The Chromel and Alumel wires were then resistance welded to the cold surface of the slug. The eloxed ring was then filled with a ceramic cement to provide thermal insulation, ensure one-directional heat flow, and to restore aerodynamic integrity.

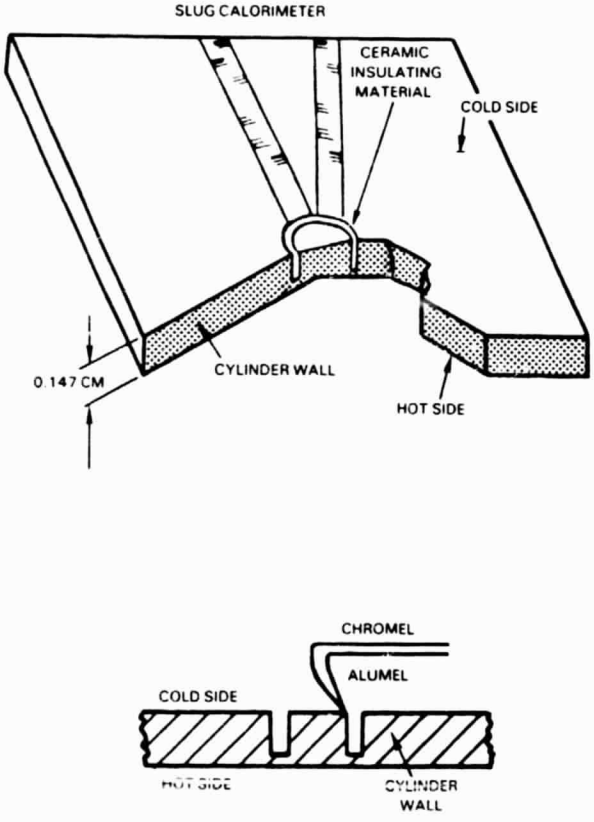

Figure 4 Schematic of Slug Calorimeter Heat Flux Sensor

SECTION 5.0
FABRICATION OF HEAT FLUX SENSORS

FABRICATION OF SENSORS INTO CYLINDER

The procedures for the fabrication of embedded thermocouple sensors and Gardon gauge sensors into turbine airfoils were developed under Phase 1 of this contract and are described in Reference 22. The procedures were adapted for the installation of sensors into the test pieces used during this second phase of the contract.

The test pieces used in the heat transfer experiment were cooled Hastelloy-X cylinders, 16 mm in diameter with a 1.5 mm wall thickness. The cylinder was cut in half along the axis of the cylinder to allow access for the installation of the sensors. The sensors were then eloxed into the cylinder with a 51 mm space between sensors. This distance was chosen so that the individual sensors could be centered in the combustor gas path without heating the other sensors. Figure 5 shows the cylinder halves and the machined sensor areas as well as the leadwire conduit tube.

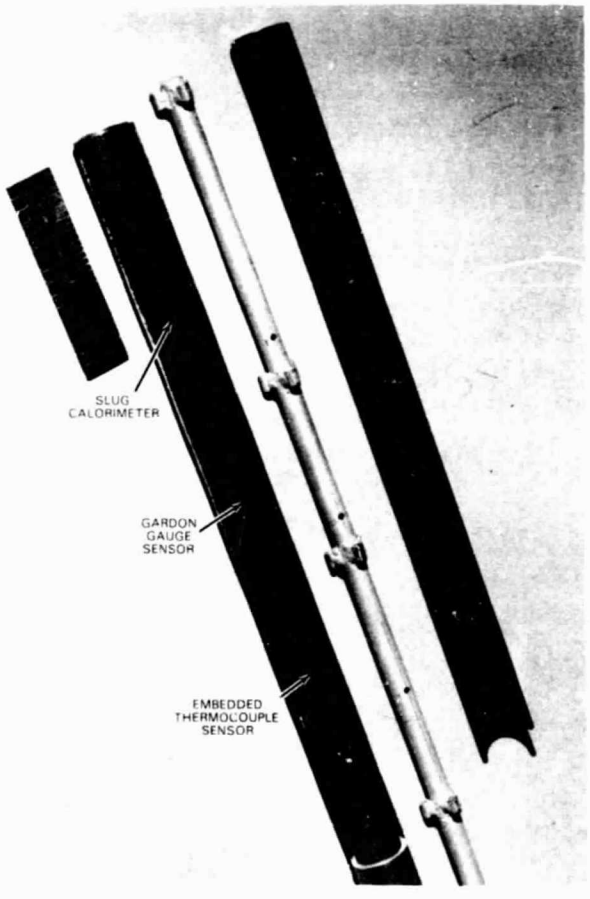

Figure 5 Cylinder Halves and Leadwire Conduit Tube

The embedded thermocouple sensor, the Gardon gauge sensor, and the slug calorimeter selected for testing were fabricated into the cylinder wall. Figures 6 through 9 show a sequence of photographs taken during installation of the embedded thermocouple sensor. The embedded thermocouple sensor was formed by machining a groove into the hot side wall and two grooves into the cold side wall to accept the thermocouple wires. The grooves were 0.3 mm wide and 0.3 mm deep and were cut by electrical discharge machining. At the thermocouple junction end of the groove, the depth was reduced to 0.13 mm to keep the thermocouple junctions as close to the surface as possible. The Alumel-Alumel junctions were directly opposite each other on the cylinder wall and the grooves were approximately 90 degrees apart to reduce the structural impact. The thermocouple wire used was 0.25 mm diameter single conductor swaged Chromel and Alumel wire. The swaged thermocouple wires were installed in the grooves and held in place by fillet wires of Chromel P, which were resistance welded in place as shown in Figures 6 and 7. After the thermoelectric junctions were made by resistance welding, the area around the thermocouple junction was filled with powdered MgO insulation material to protect the thermoelectric junctions. A Hastelloy-X cap was then welded over the sensing area. After the wires and caps were installed, the area was manually smoothed to restore aerodynamic integrity. The completed embedded thermocouple sensor is shown in Figures 8 and 9.

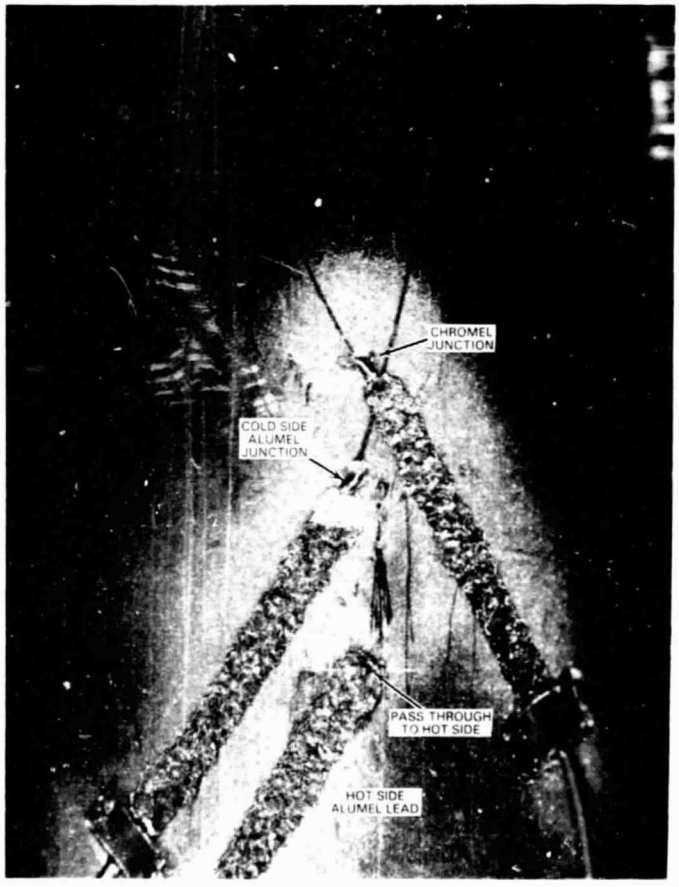

Figure 6 Cold Side of Embedded Thermocouple Sensor After Installation of Leadwires

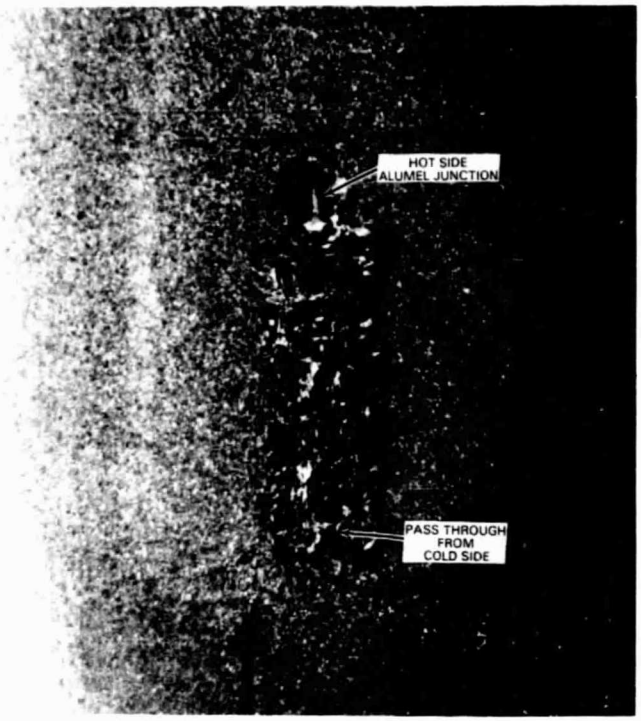

Figure 7 Hot Side of Embedded Thermocouple Sensor After Installation of Leadwires

Figure 8 Cold Side of Completed Embedded Thermocouple Sensor

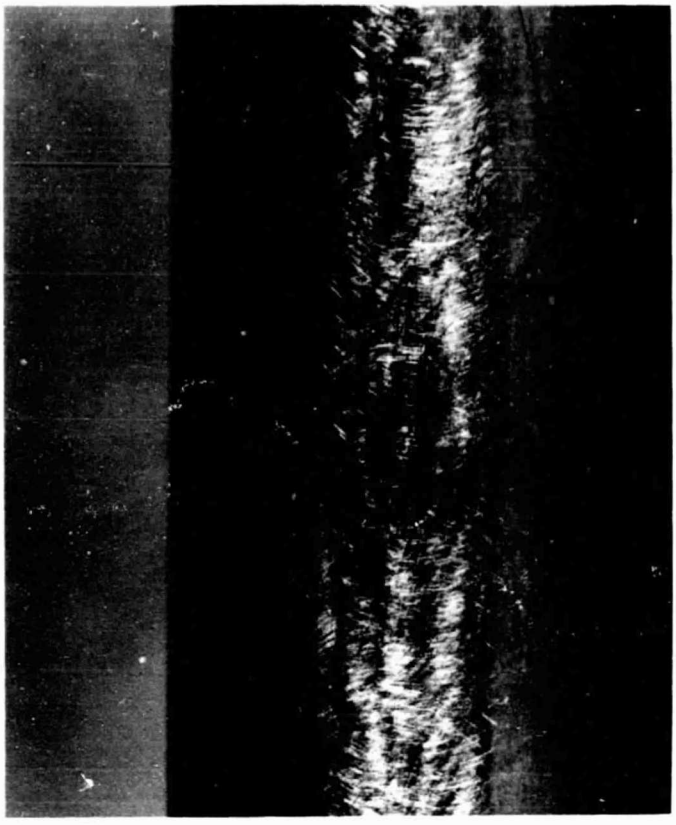

Figure 9 Hot Side of Completed Embedded Thermocouple Sensor

Figures 10 through 12 show a sequence of photographs taken during construction of the Gardon gauge sensor. The Gardon gauge sensor was fabricated by machining a cavity 1.5 mm in diameter into the cold side surface to a depth that left a sensor foil .22 mm $\pm$ .04 mm thick at the bottom of the cavity. This dimension was determined by using Pratt & Whitney's TCAL program to optimize the sensor performance. A curvature was used on the end of the tool to produce a uniform thickness at the bottom of the hole in the curved tube wall. Next, a 0.55 mm deep groove was machined into the cold side wall for the leadwire. Special eloxing tools were required to maintain constant dimensions for the curved surfaces of the cylinder. The wire used to fabricate these sensors was a three conductor swaged wire 0.5 mm in diameter with two Alumel and one Chromel conductor. The thermocouple wire was installed in the channel utilizing the technique discussed above using Chromel P as a fillet wire. One Alumel wire was attached by resistance welding in the center at the bottom of the cavity and another Alumel wire was attached to the sidewall of the cavity near the bottom. The Chromel wire was attached to the sidewall near the bottom of the cavity directly opposite the Alumel wire as shown in Figure 10. The area where the leadwire was installed was ground relatively smooth as shown in Figure 11. The cavity of the Gardon gauge was filled with M-Bond GA100 ceramic cement. This cement provided both structural protection and oxidation resistance for the small wires. After the ceramic was given an oven cure, the surface was manually smoothed to restore aerodynamic integrity. Figure 12 shows the completed Gardon gauge sensor.

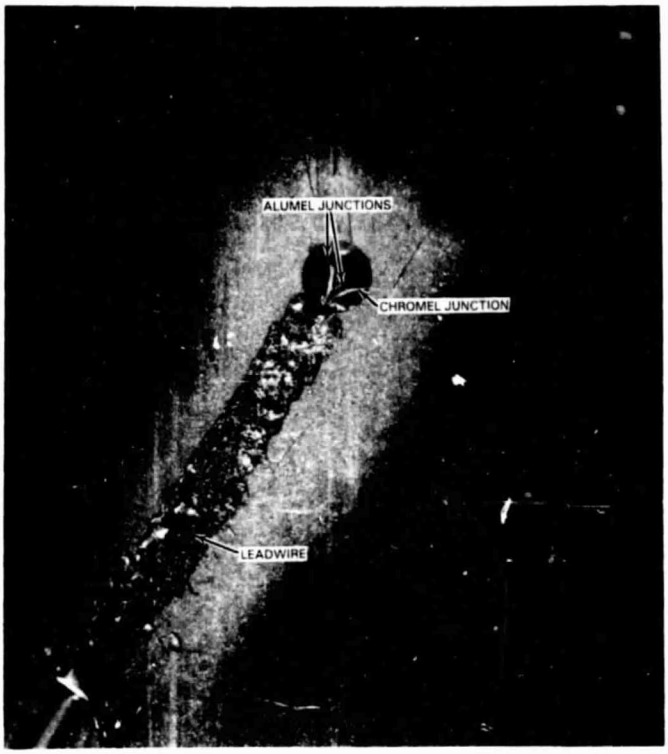

Figure 10 Gardon Gauge After Installation of Leadwires

Figure 11 Gardon Gauge After Smoothing Leadwire Installation

Figure 12 Completed Gardon Gauge

The construction of the slug calorimeter is shown in Figures 13 through 15. The slug calorimeter sensor was fabricated by machining a ring .19 mm wide and .25 mm deep around a slug of material 1.5 mm in diameter on the cold side surface of the cylinder. Two grooves .3 mm wide and .3 mm deep were machined into the cold side wall for the leadwires. The wires used for these sensors were .25 mm single conductor swaged Chromel and Alumel wires. The thermocouples were installed in the grooves and held in place with fillet wires of Chromel P. The thermocouple junction was made at the side of the slug on the cold surface as shown in Figure 13. After the thermoelectric junction was made, the surface was manually smoothed to restore aerodynamic integrity (Figure 14). The ring was then filled with M-Bond GA100 ceramic cement to provide thermal isolation for the sensor area. The cement was then given an oven cure. The completed slug calorimeter sensor is shown in Figure 15.

Following fabrication of the sensors a leadwire conduit tube was installed in the cylinder and the sensor leads were led out through it (Figure 16). Spacers were installed on the leadwire conduit to keep it centered in the cylinder. The cylinder halves were welded together as shown in Figure 17. The completed cylinder test piece is shown in Figure 18.

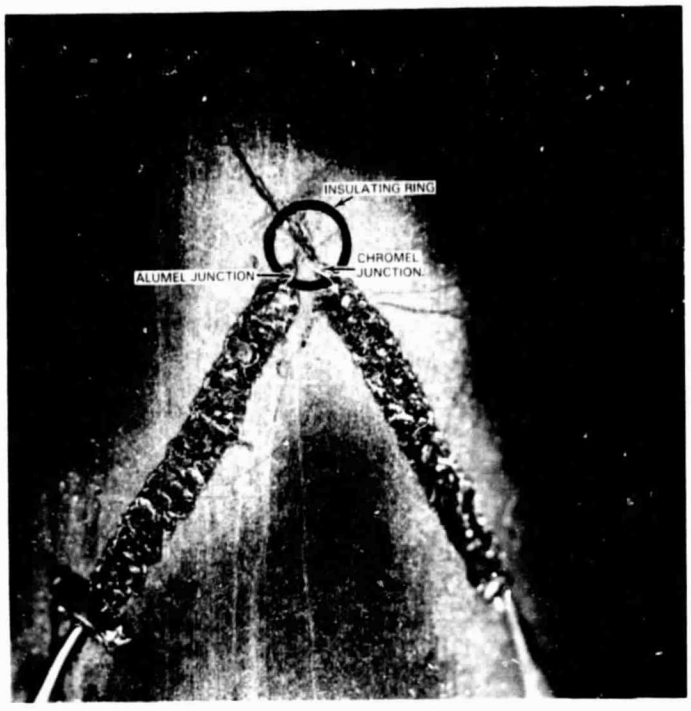

Figure 13 Slug Calorimeter After Installation of Leadwires

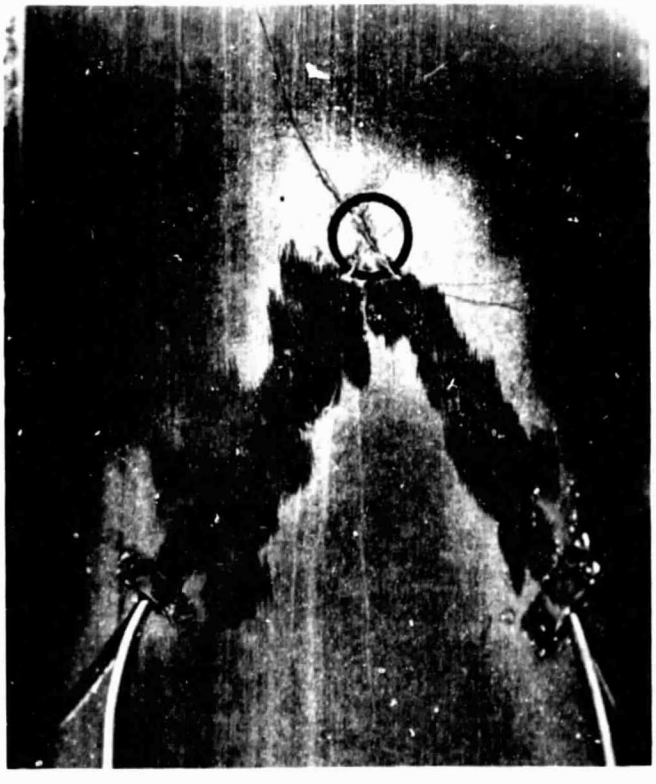

Figure 14 Slug Calorimeter After Smoothing Leadwire Installation

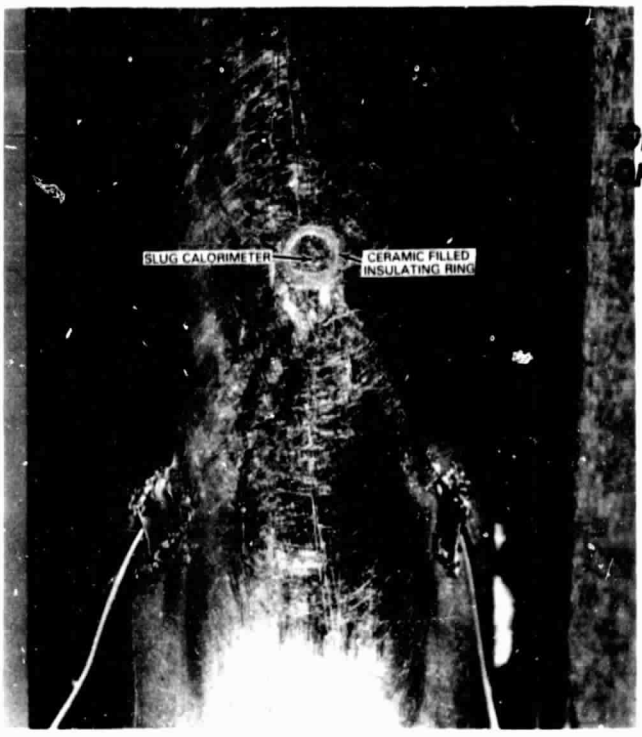

Figure 15 Completed Slug Calorimeter

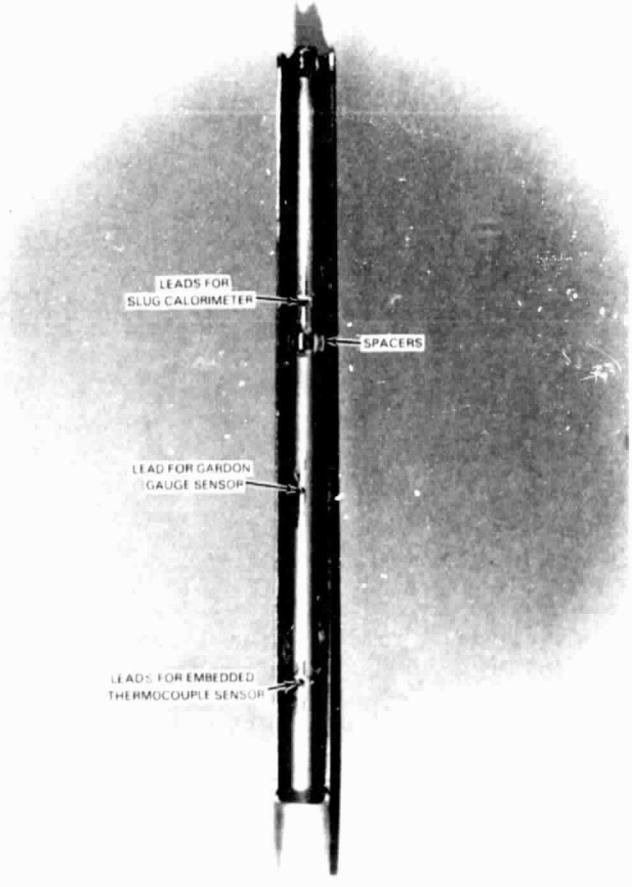

Figure 16 Cylinder After Installation of Leadwire Conduit

Figure 17 End View of Cylinder After Welding

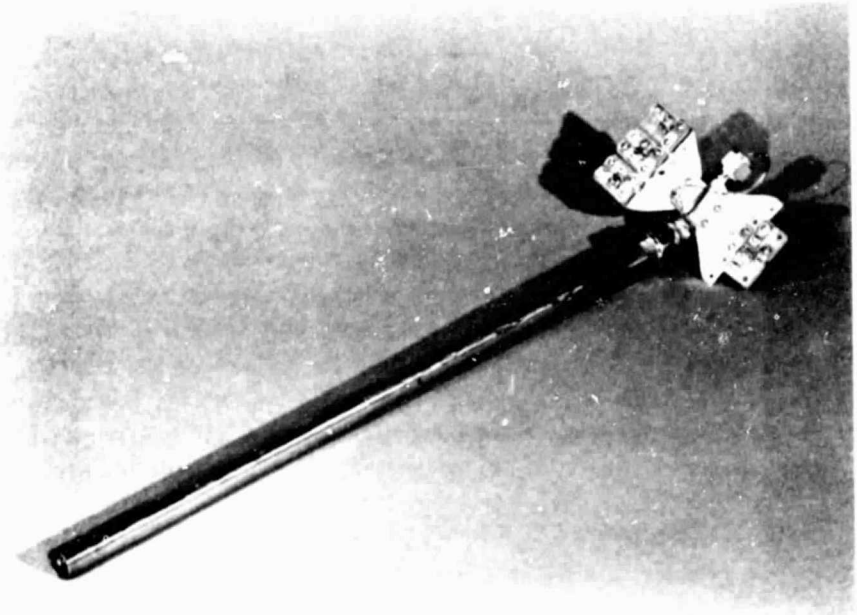

Figure 18 Completed Cylinder

The probe that was to be used to measure dynamic gas temperature fluctuations was the dual fine wire thermocouple probe that was developed at Pratt & Whitney under NASA Contract NAS3-23154. This probe is shown in Figure 19. Details of the construction of these probes can be found in Reference 25.

The cylinders for the sputtered thermocouple surface temperature sensors were made from solid NiCoCrAlY rods. The rods were cast in Pratt & Whitney's Material Laboratory as 31 cm long 1.9 cm diameter rods. The rods were ground to a diameter of 1.6 cm and drilled with carbide tipped tools to produce a .6 cm hole for coolant flow. The thermocouples were sputtered onto the cylinder as described in Reference 27. The completed cylinder with sputtered thermocouple installed is shown in Figure 20.

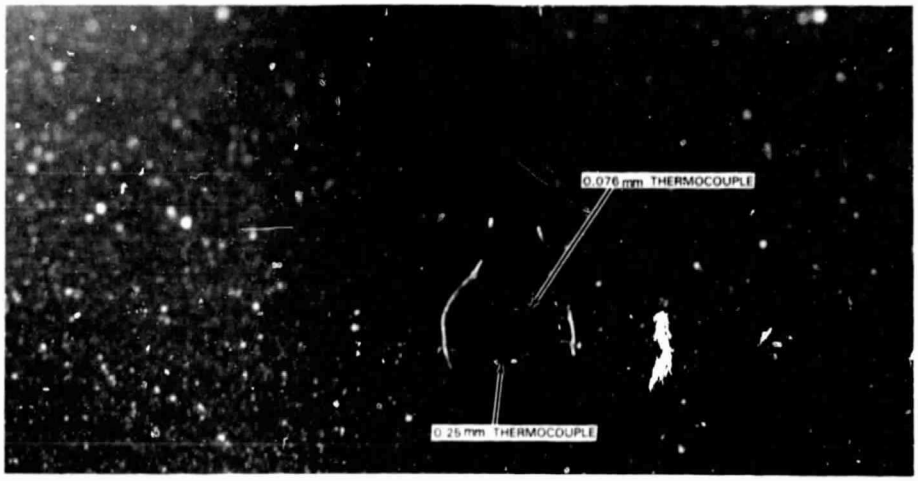

Figure 19 Dual Fine Wire Thermocouple Probe

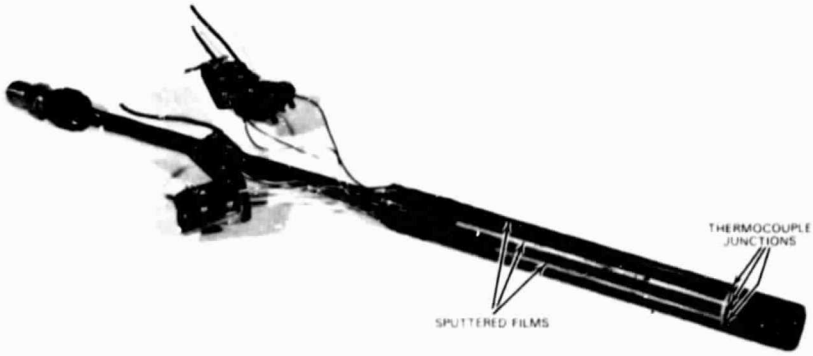

Figure 20 Cylinder with Sputtered Thermocouple Surface Temperature Sensors

SECTION 6.0
CALIBRATION

After fabrication, a program was undertaken to provide calibrations of the heat flux sensors to determine the output versus transmitted heat flux relationship. Due to variations between sensors because of manufacturing tolerances, individual sensor calibrations were performed to obtain maximum accuracy.

CALIBRATION TEST FACILITY

A quartz lamp bank test facility was used for all testing. The cylinders were cooled with internal cooling air. The heat source was a quartz lamp bank with six parallel quartz halogen bulbs each rated at 6 KW. The bulbs were 25.4 cm long and the width of the lamp assembly was 7.6 cm. This lamp assembly was capable of producing a maximum heat flux incident on the sensors of 1.7 MW/m^2. During routine operation, the lamp was operated to approximately 1.0 MW/m^2 to maximize lamp life.

A photograph of the lamp face is shown in Figure 21. The reflector on the lamp is water cooled and the bulbs are air cooled to permit continuous operation. The cylinder under test was positioned below the lamp and was surrounded with polished water-cooled shields to concentrate the energy onto the cylinder. The cylinder was positioned so that the surface of the sensors was parallel to the plane of the lamps and as close to the lamps as possible. The heat flux output of the lamp was monitored by a reference heat flux sensor mounted in the shield. After the shields were positioned for the cylinder calibration, the cylinder was removed from the lamp assembly and a second reference sensor was mounted at the location the cylinder would occupy during calibration. A calibration of the assembly was then performed to determine the relationship between the heat flux incident at the cylinder sensor location to that at the reference sensor location. This relationship was used to correct the data measured by the reference sensor during the cylinder calibration. The position of the two reference sensors was exchanged and the calibration was repeated to eliminate the effect of any bias between the two sensor on the reference sensor calibrations.

SENSOR CALIBRATIONS

In order to calibrate the sensors on the cylinder, the completed cylinder was positioned under the lamp bank with the sensor being calibrated centered directly under the heat source. A typical setup is shown in Figure 22. The cylinders were coated with "Zynolite 1000F Hi-Temp"[2] black paint to provide a constant known emittance/absorptance of 0.89 for calibration. Data from the calibrations was acquired with a microcomputer system (see Reference 22). The data at each calibration point was output to a printer and was also stored on disk for later analysis.

[2]Zynolite Products Company, 15700 South Avalon, Compton, CA 90224

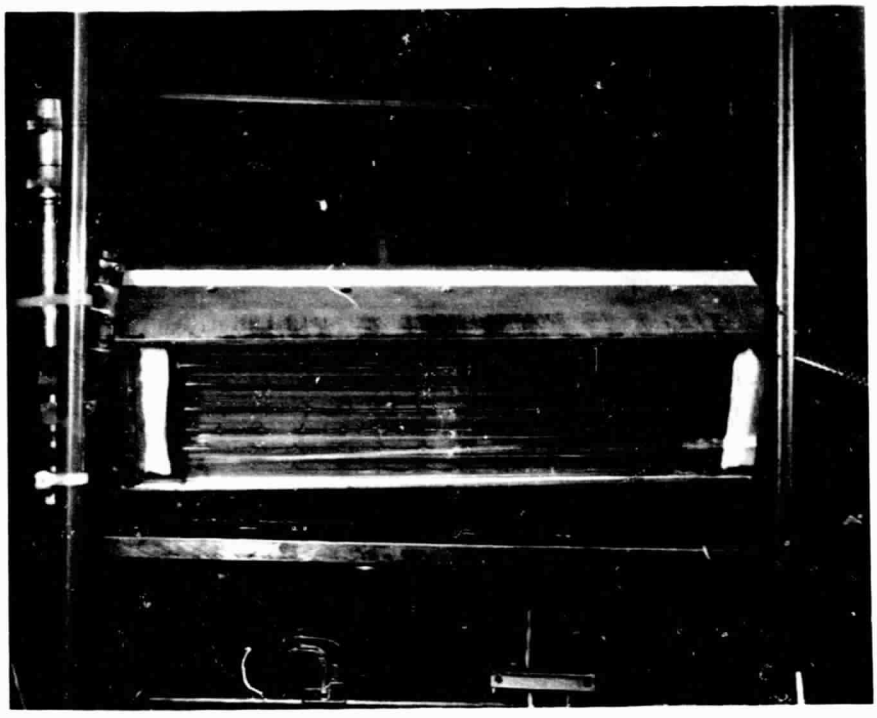

Figure 21 Face of 36 Kilowatt Calibration Lamp

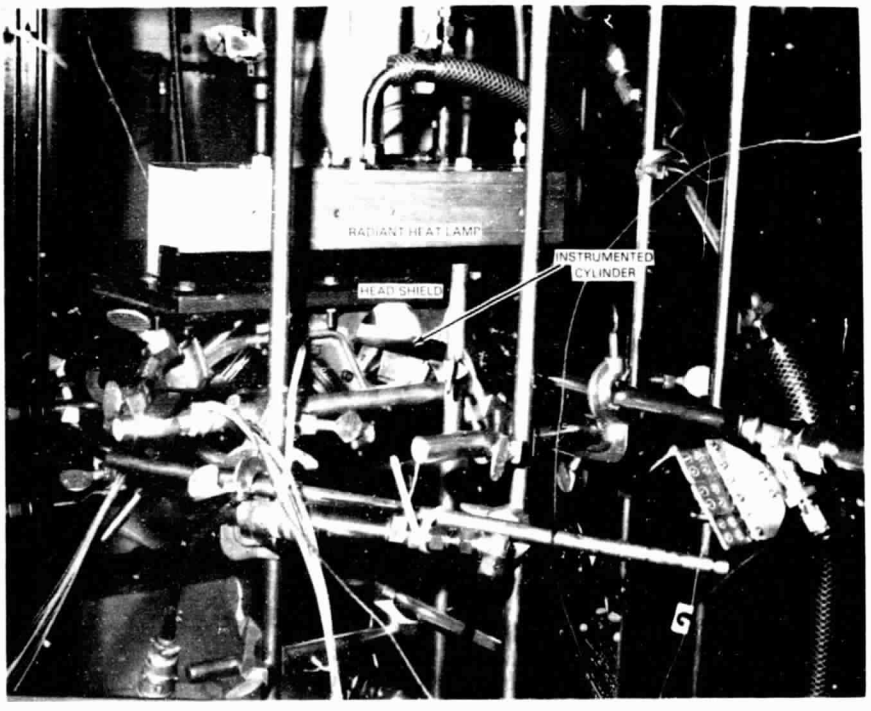

Figure 22 Typical Setup for Sensor Calibration

The calibrations for the embedded thermocouple and Gardon gauge sensors were conducted under two sets of conditions: varying incident heat load at constant sensor temperature and varying incident heat load at constant coolant flow. The heat flux transmitted through the cylinder wall was calculated by determining the heat absorbed and subtracting the heat losses from the front face by convection and reradiation. The absorbed heat flux is equal to the incident heat flux as measured by the reference sensor, corrected to the test sensor location, times the absorptance of the cylinder surface. The convective loss is equal to the convection heat transfer coefficient (determined during an earlier test program (Ref. 22) times the temperature differential between the sensor surface and the ambient air temperature. The re-radiation loss is the emittance of the cylinder times the Stefan-Boltzman constant times the difference in the fourth powers of the sensor surface temperature and the sink temperature. The sink temperature was experimentally determined as 400K for this calculation. A detailed error analysis of this calibration procedure is presented in Reference 21.

Since the slug calorimeter was a transient sensor, a different calibration procedure was used. To obtain a calibration, the quartz lamp bank was set to a known heat flux level. After the lamp stabilized, as determined from the reference sensor, the cylinder was rapidly moved under the lamp. Cooling air was later turned on to prevent over-heating the sensor. This was done under computer control by activating an actuator in the coolant line when a specified sensor temperature was reached. Because the cylinder was not heated uniformly, non-one-dimensional heat flow became important as the cylinder became hotter. To avoid this error source, only the data taken from the early portion of the heating transient was used. Transient calibrations were also performed on the Gardon gauge sensors using the same procedure used for the slug calorimeters.

Two cylinders were fabricated, each with an embedded thermocouple sensor, a Gardon gauge sensor and a slug calorimeter. The calibration results on these sensors are presented in Figures 23 through 31.

For the embedded thermocouple sensors and the Gardon gauge sensors, the first plot in each figure shows sensor output vs. heat flux transmitted through the sensor. A least square fit was performed on the data to obtain sensor sensitivity (output per unit heat flux transmitted). The second plot in each figure shows the variation of the calibration data from that least square line with sensor temperature. All the data falls within the $\pm$ 5% of the 1 megawatt per meter squared error bands. The sensor sensitivities also show no significant variation with sensor temperature. Some sensors do show a relatively large scatter in sensor sensitivity at high temperature. This scatter is due to the high temperature, low heat flux data where small errors in any of the calibration parameters can result in large errors in sensor sensitivity. This data is not representative of realistic test conditions. Figures 25 and 28 show typical calibration runs for the slug calorimeter sensors. The data from these runs were reduced to obtain a calibration factor: heating rate (degrees/sec) per unit heat flux absorbed (megawatt per meter squared). The data from the calibrations of the slug calorimeters is summarized in Figure 29 which shows a probability plot of the calibration

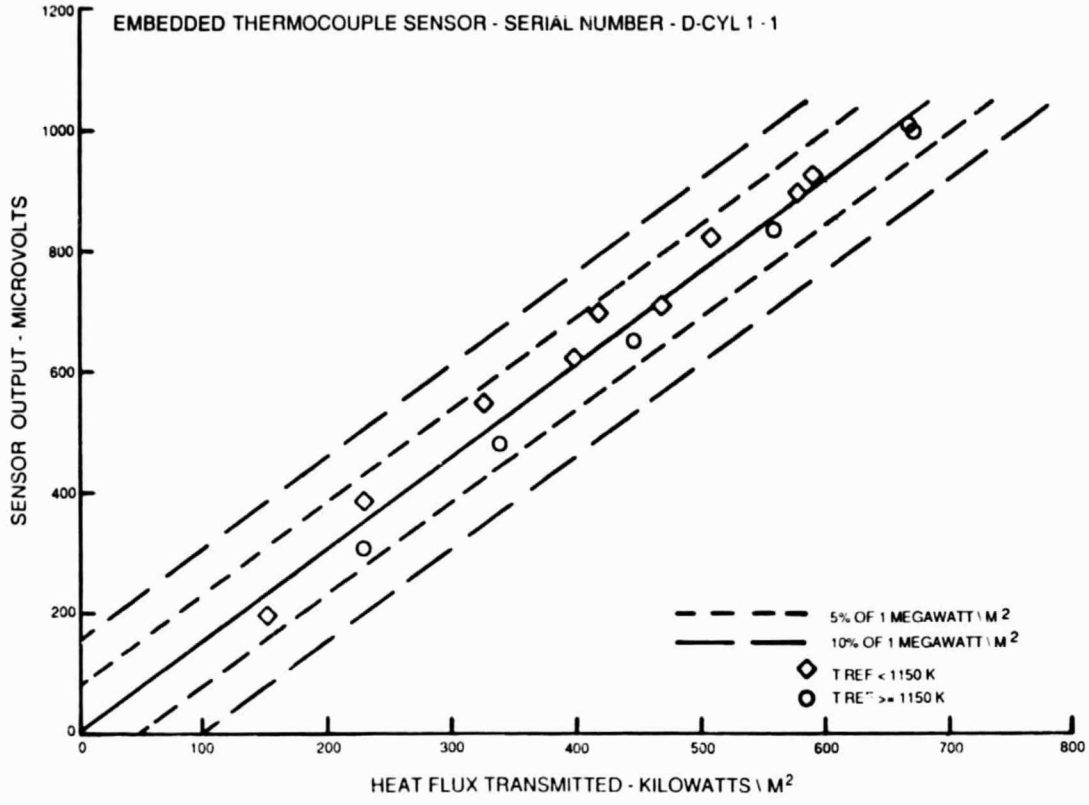

Figure 23a Calibration Results for Embedded Thermocouple Sensor in Cylinder 1

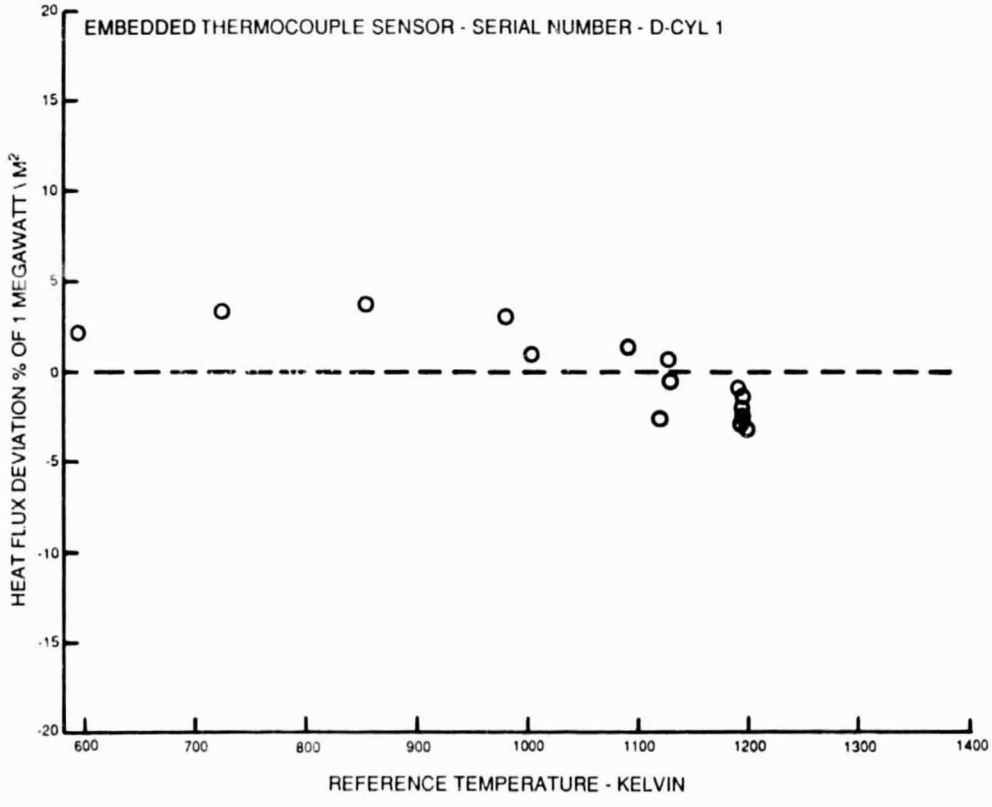

Figure 23b Calibration Results for Embedded Thermocouple Sensor in Cylinder 1

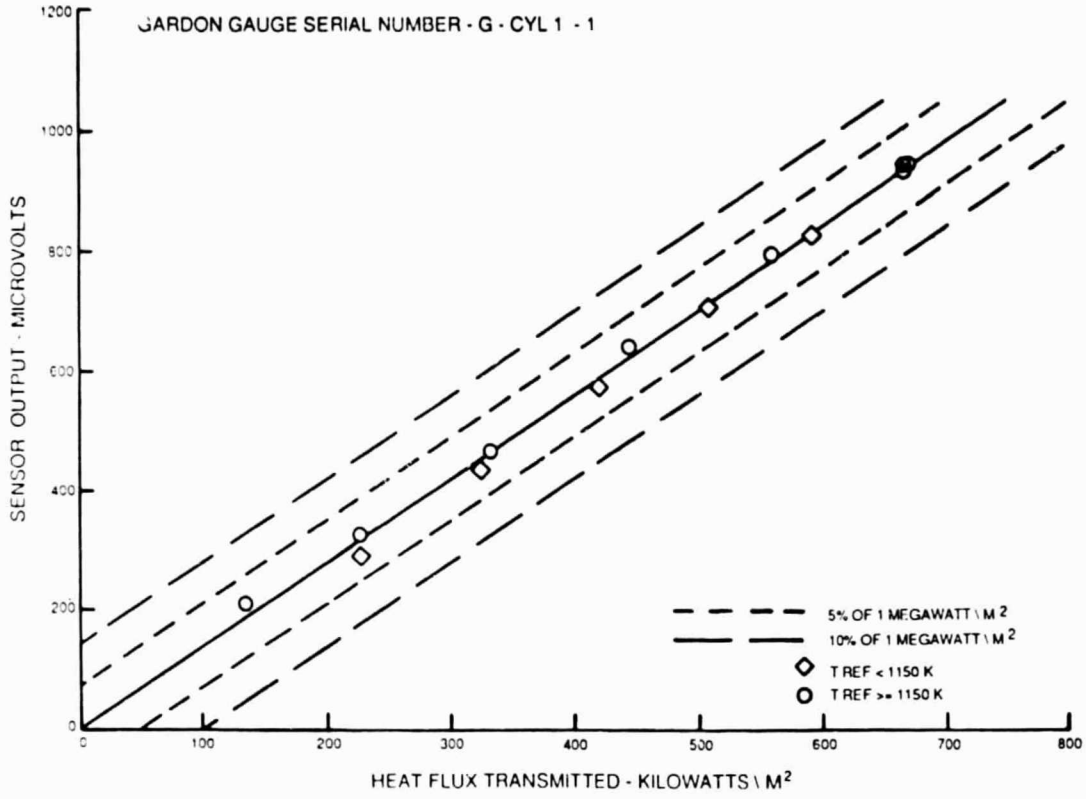

Figure 24a Calibration Results for Gardon Gauge Sensor in Cylinder 1

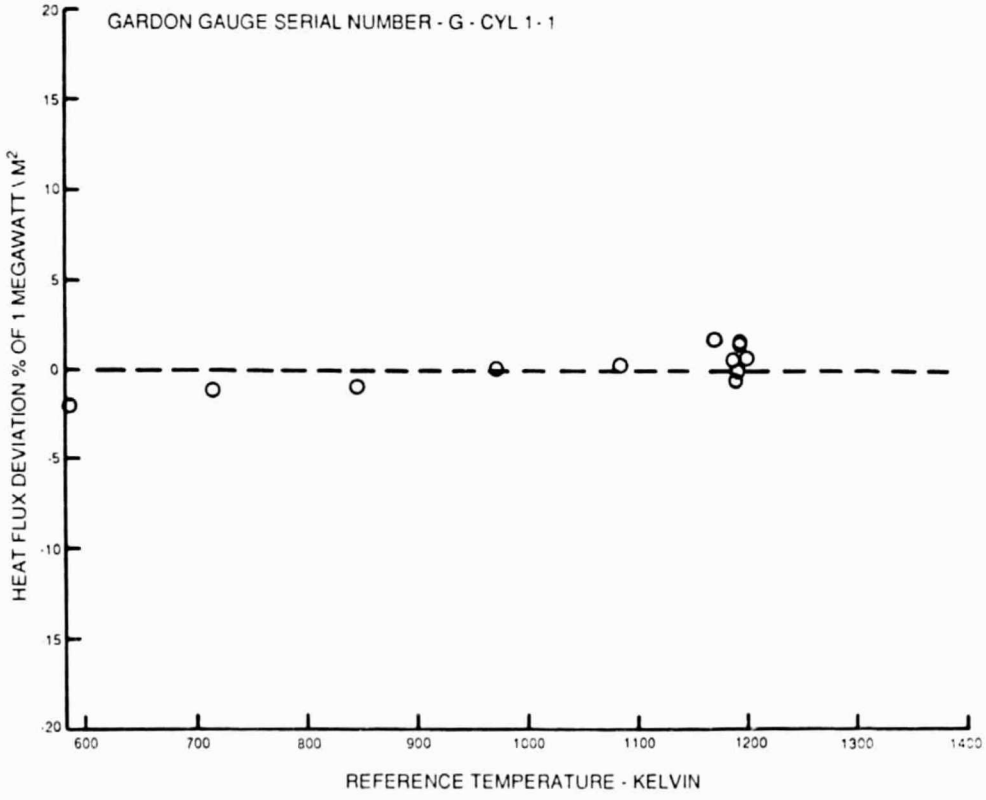

Figure 24b Calibration Results for Gardon Gauge Sensor in Cylinder 1

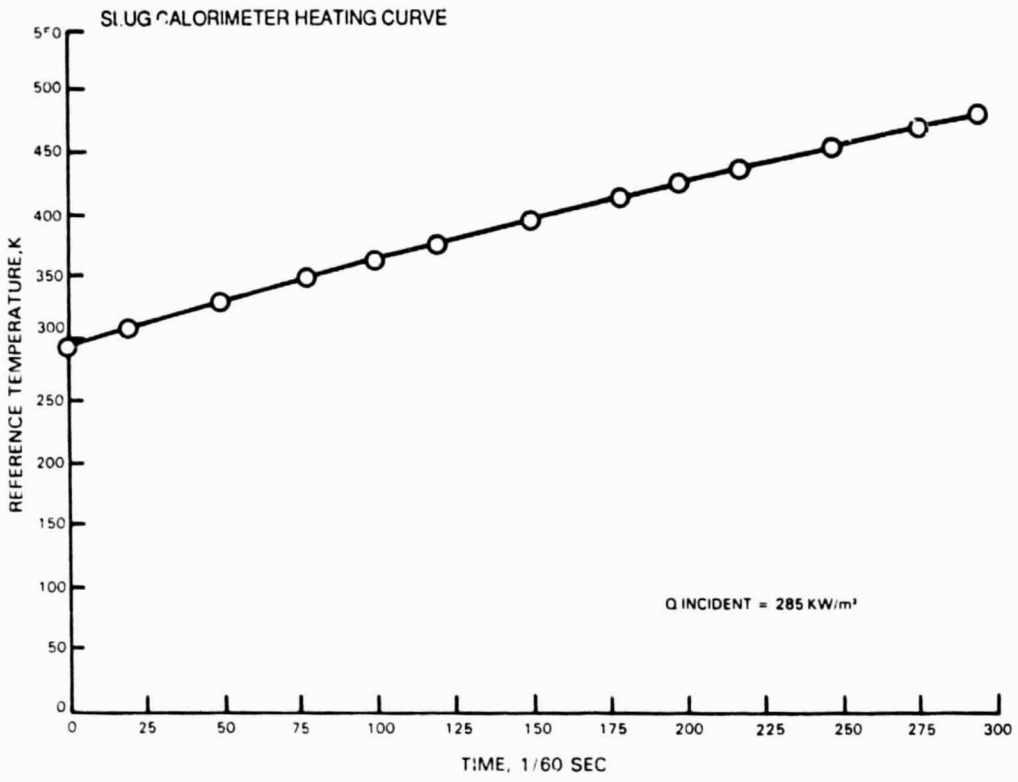

Figure 25 Typical Calibration Point for Slug Calorimeter in Cylinder 1

factor obtained during the various calibration runs. This data has been normalized to 365K to correct for variation in specific heat of the slug material with temperature. While the data from cylinder 2 does show significantly greater scatter than the data from cylinder 1, all data for both cylinders fall within ± 5% of the mean result for that cylinder. Figure 30 shows a typical transient run for a Gardon gauge sensor. The data from the Gardon gauge sensors is summarized in Figure 31. Due to the fact that the Gardon gauge foil is much thinner than the slug calorimeter, the sensitivity of the Gardon gauge is approximately an order of magnitude higher. It can be seen that for both Gardon gauge sensors the calibration constant (heating rate per heat flux absorbed) increases slightly with increasing heat flux. This is to be expected since losses through the edges of the Gardon gauge will have less effect at more rapid heating rates.

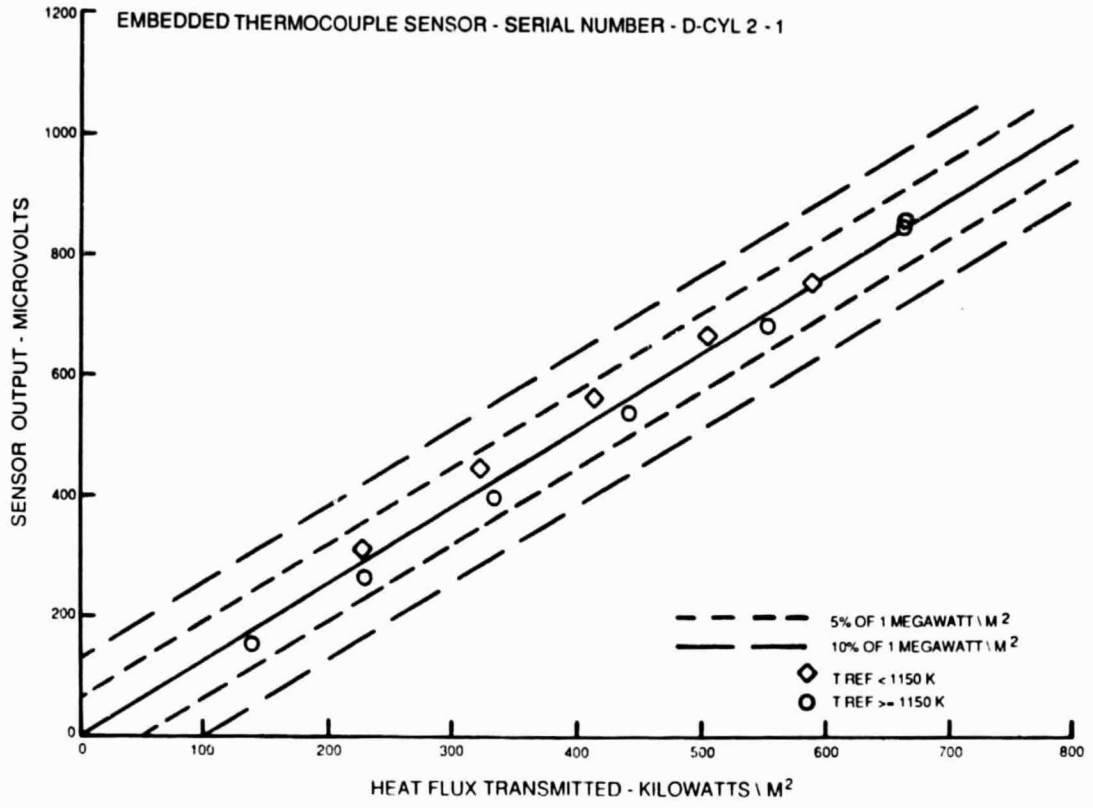

Figure 26a Calibration Results for Embedded Thermocouple Sensor in Cylinder 2

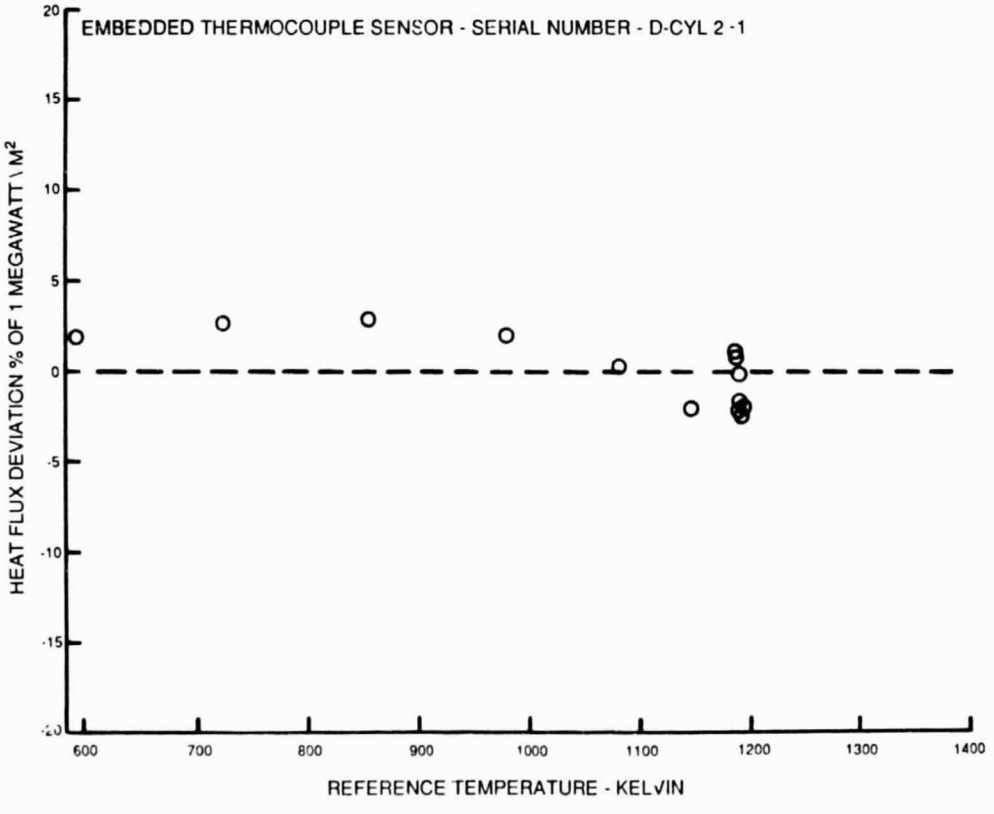

Figure 26b Calibration Results for Embedded Thermocouple Sensor in Cylinder 2

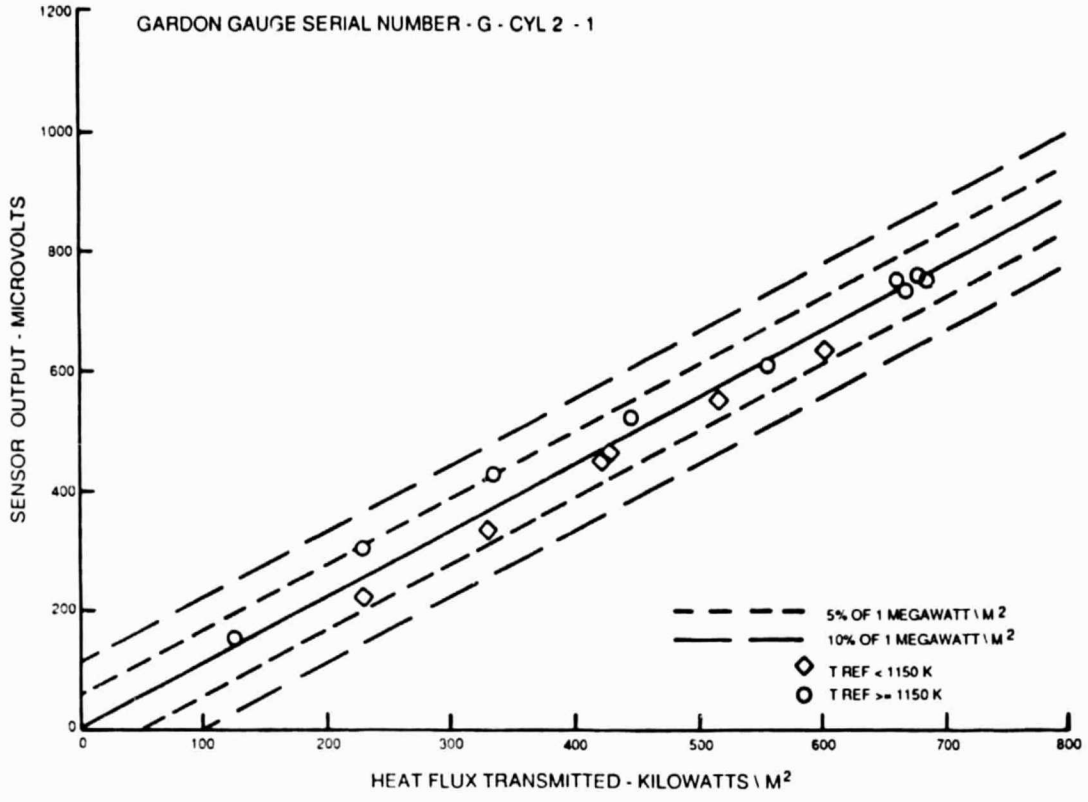

Figure 27a Calibration Results for Gardon Gauge Sensor in Cylinder 2

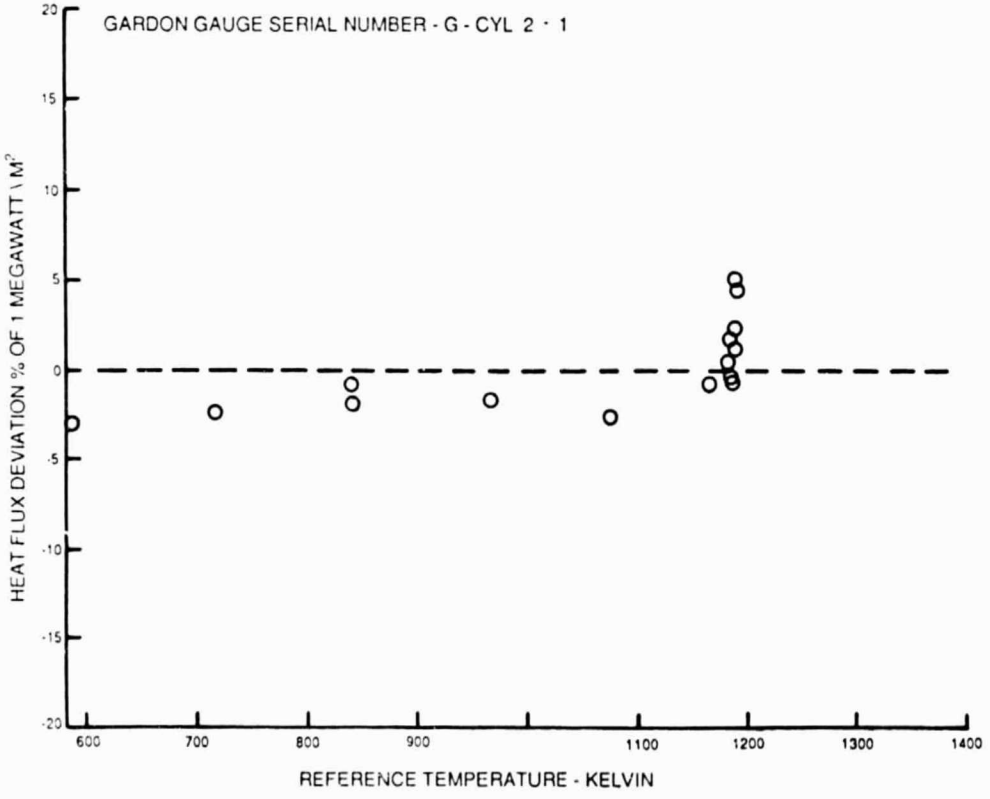

Figure 27b Calibration Results for Gardon Gauge Sensor in Cylinder 2

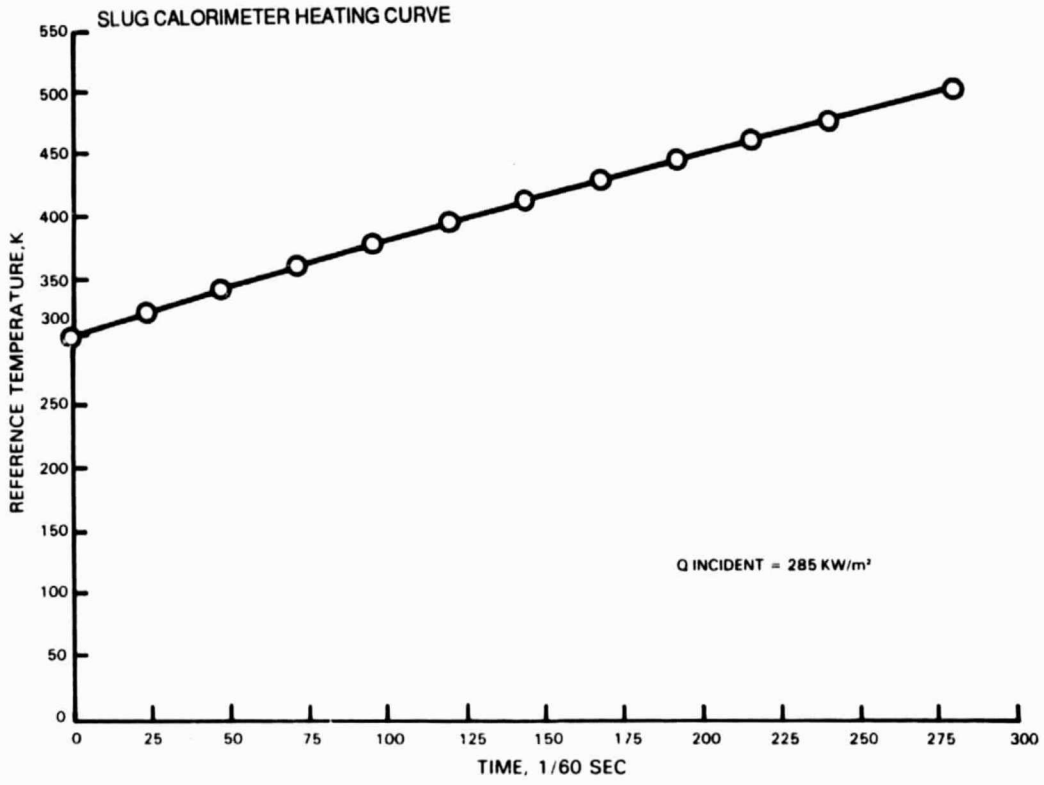

Figure 28 Typical Calibration Point for Slug Calorimeter in Cylinder 2

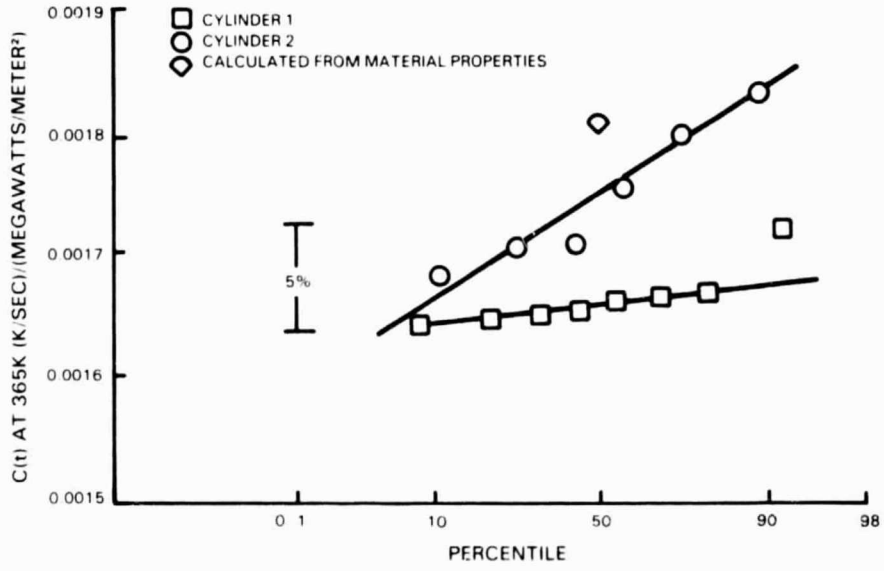

Figure 29 Probability Plot Summarizing Slug Calorimeter Calibration Results

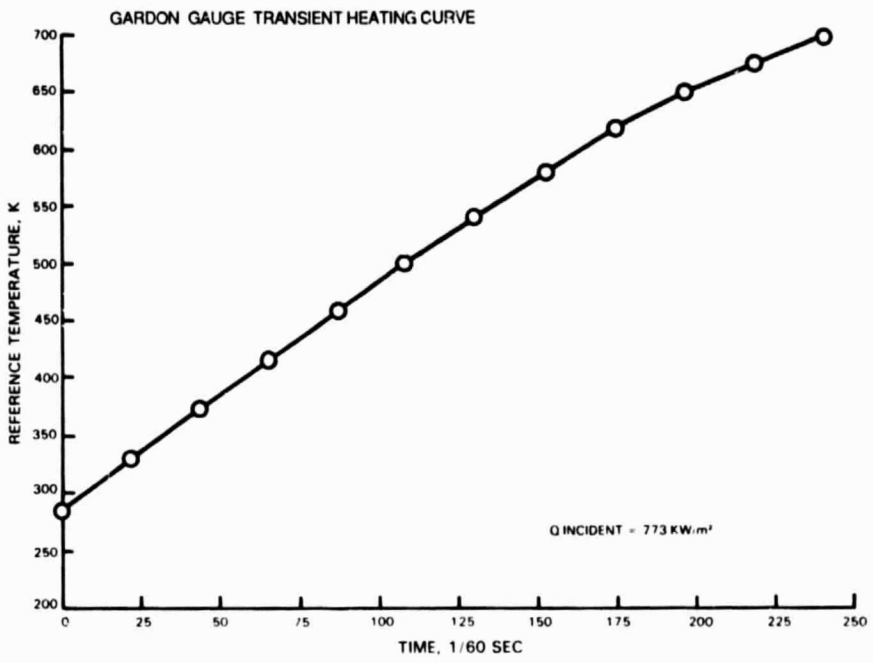

Figure 30 Typical Calibration Point for Gardon Gauge in Cylinder 1 - Transient Run

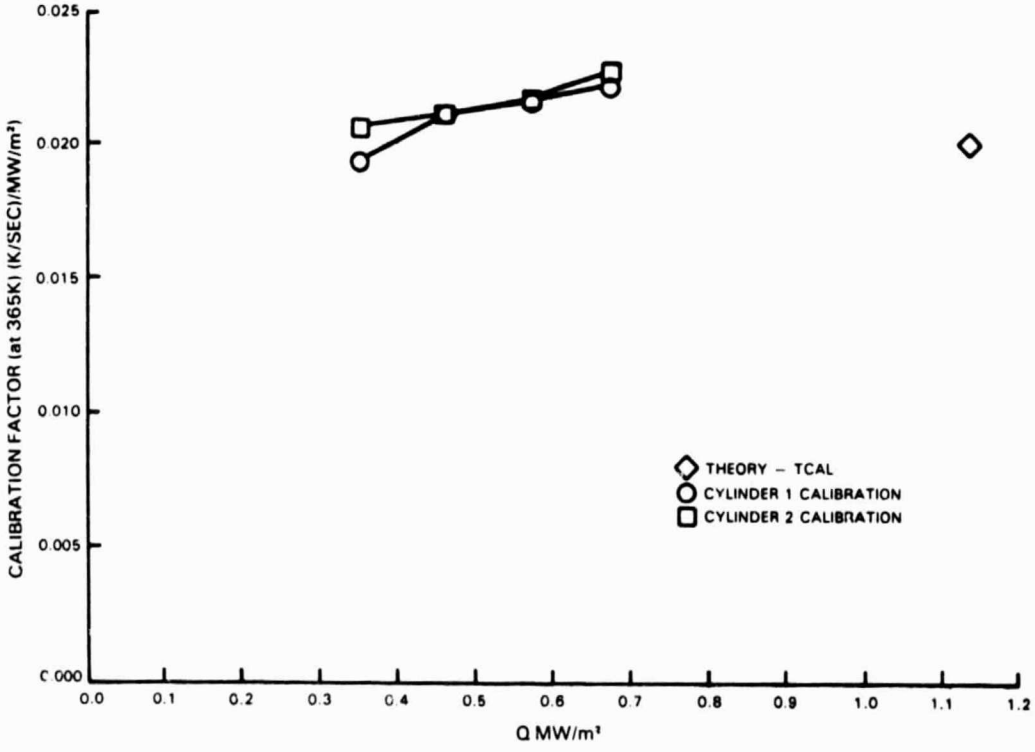

Figure 31 Transient Gardon Gauge Calibration Summary

SECTION 7.0
RIG TESTING

Rig testing of the instrumented cylinders, sputtered thermocouple sensors and dual fine wire thermocouple probes was a two step process. In the first step, characterization tests of the burner were conducted and in the second step, data from the various sensors were acquired.

BURNER CHARACTERIZATION TESTING

The cylinder in crossflow experiment was conducted with the use of a Becon[3] atmospheric pressure combustor rig. A schematic of that rig is shown in Figure 32. The combustor was composed of five modules which could be combined or adapted to perform a variety of tasks with a minimum of effort. At the front of the combustor, a fuel nozzle plate contained the fuel nozzle system. The primary section was composed of an annular diffuser and a combustor liner which controlled the air flow and combustion in the primary zone. The ignitor, a flame monitor, and auxiliary instrumentation ports were included in a standard instrumentation ring located aft of the primary section. The secondary section was composed of an annular diffuser and a combustor liner which controlled mixing in the secondary zone. An exhaust nozzle plate secured a variety of cooled or uncooled exhaust nozzles to the secondary section. For this test program a 5 cm diameter nozzle was used.

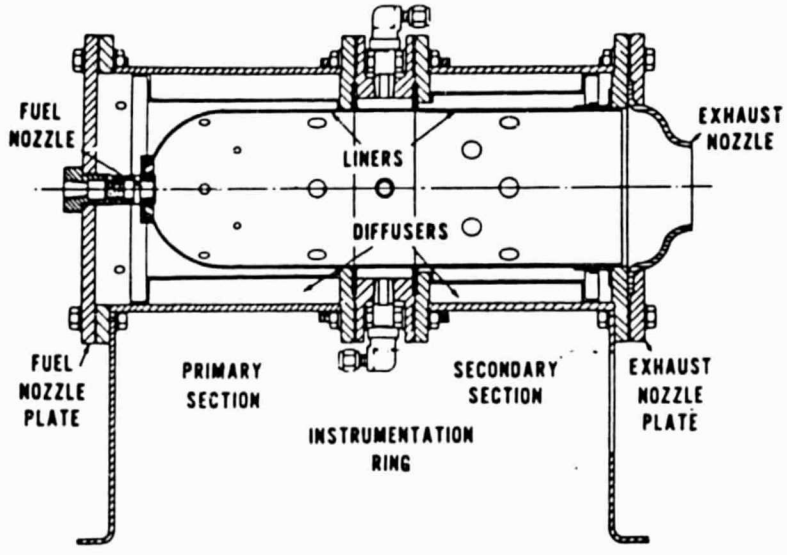

Figure 32 Schematic of Atmospheric Pressure Combustor Rig

To better define the environment for the cylinder in cross flow test, a test program was conducted to characterize the exit gas temperature and pressure profiles from this rig. Data was taken with an aspirating temperature probe that was traversed through the gas path downstream of the nozzle. Pressure data was taken at these same traverse points by dead-ending the aspirating probe to a pressure gauge and turning off the vacuum pump to the probe. Pressure and temperature data were taken at various set points. Figures 33 through 36 show characterization results from the burner at 1700 K and 1533 K with the probe 5 cm. from the nozzle.

[3]Becon Incorporated, 46 Schweir Rd., South Windsor, CT 06074

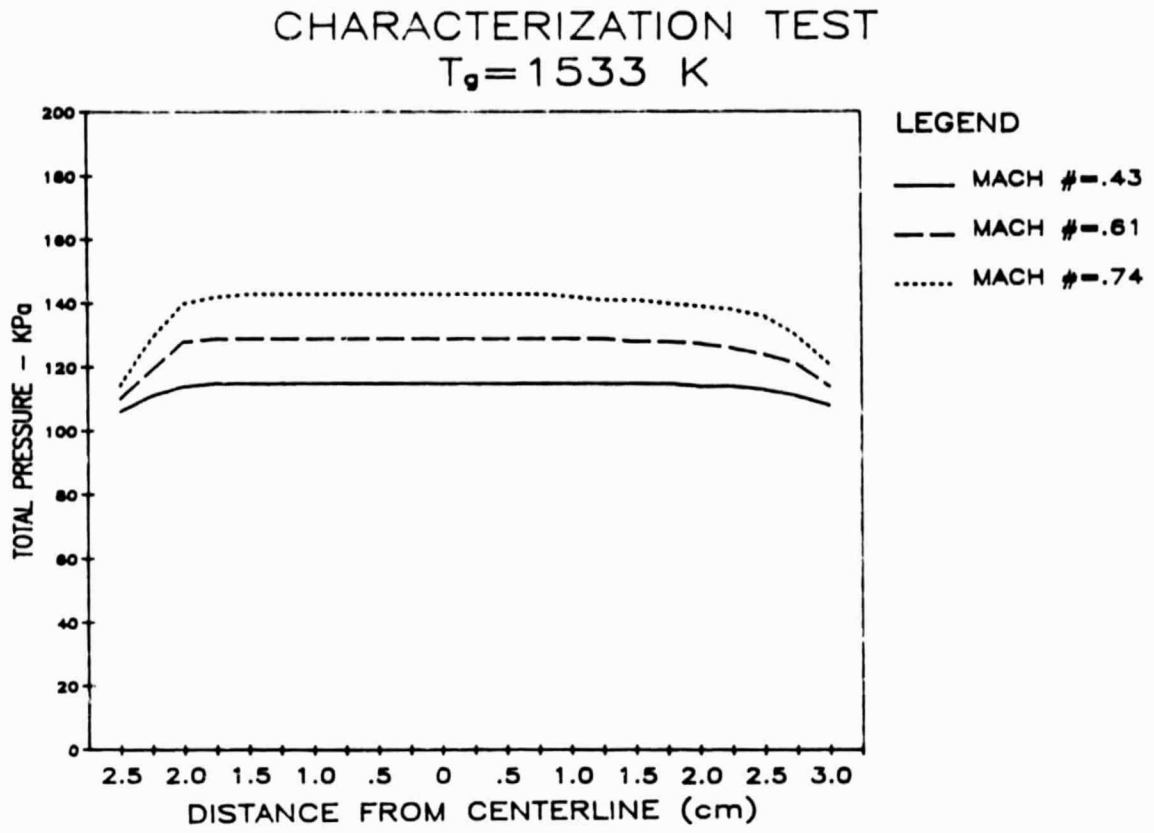

Figure 33 Combustor Total Pressure Profiles at 1533K Combustor Exit Temperature - Horizontal Traverse

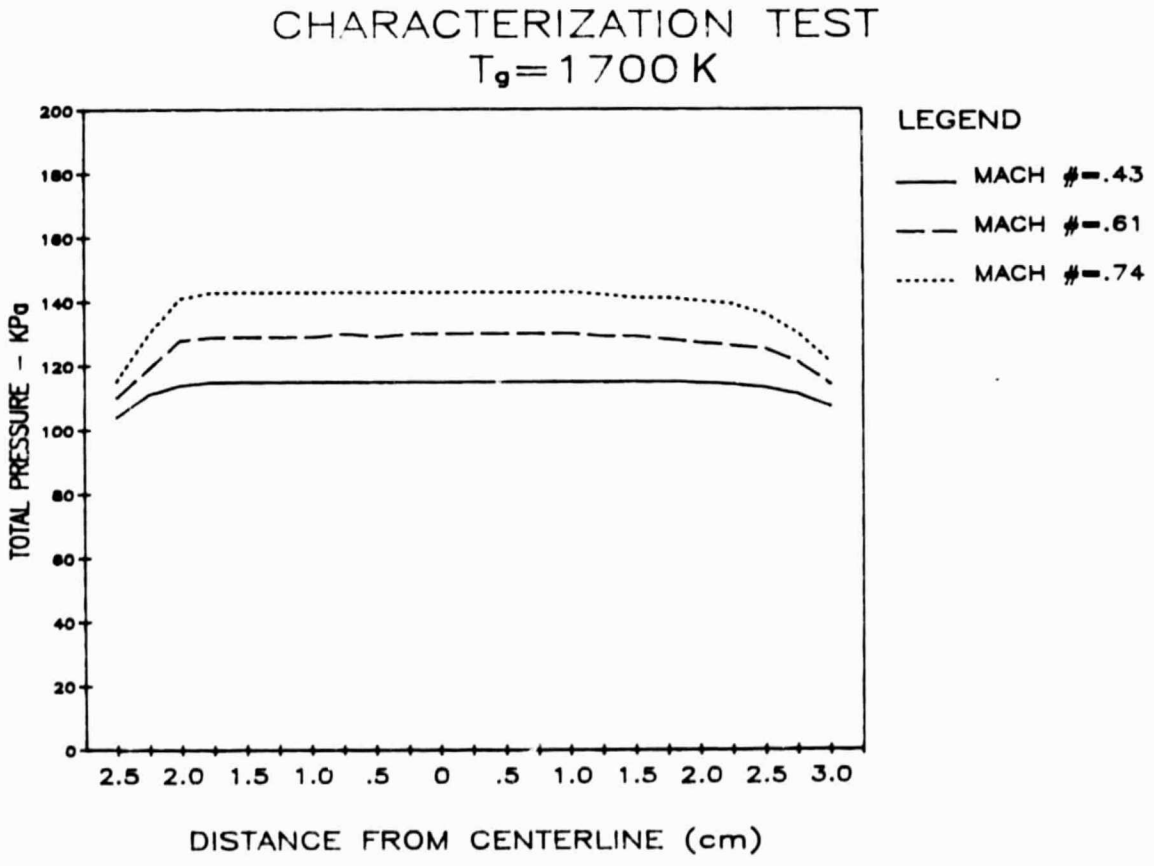

Figure 34 Combustor Total Pressure Profiles at 1700K Combustor Exit Temperature - Horizontal Traverse

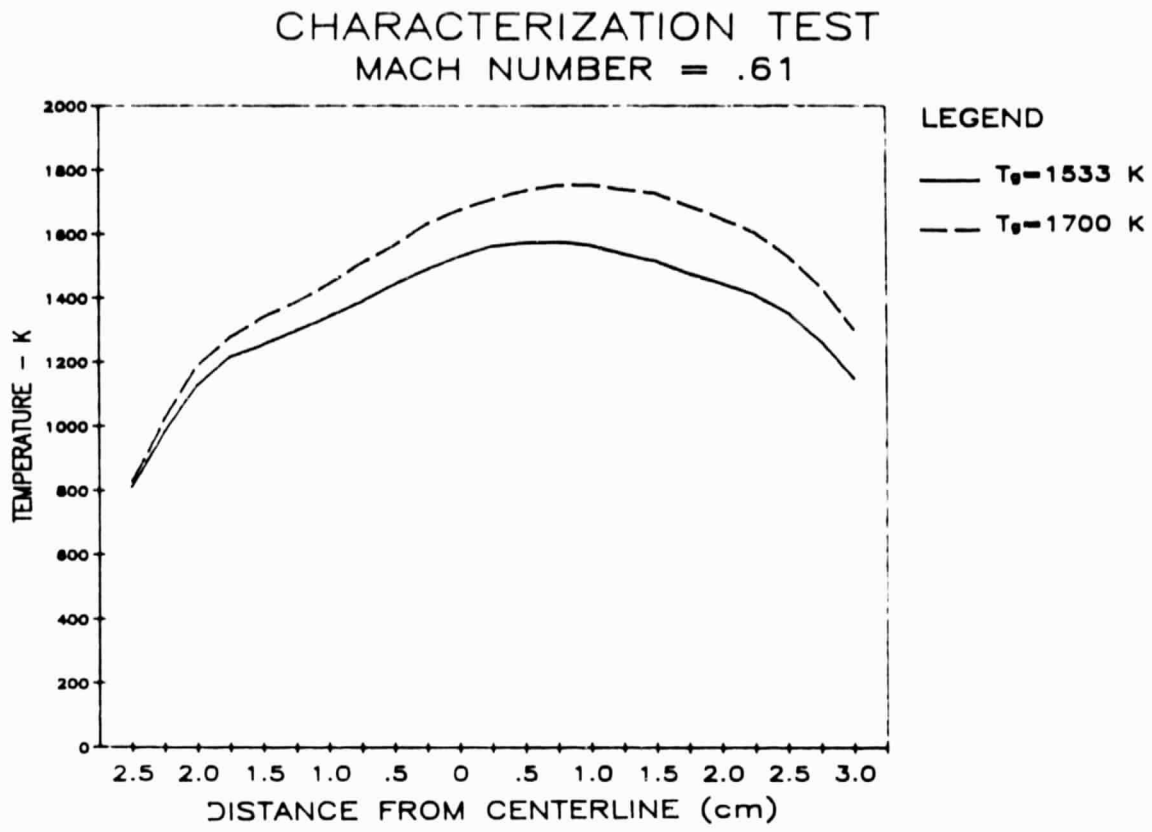

Figure 35 Combustor Temperature Profiles at Mach Number = 0.61 - Horizontal Traverse

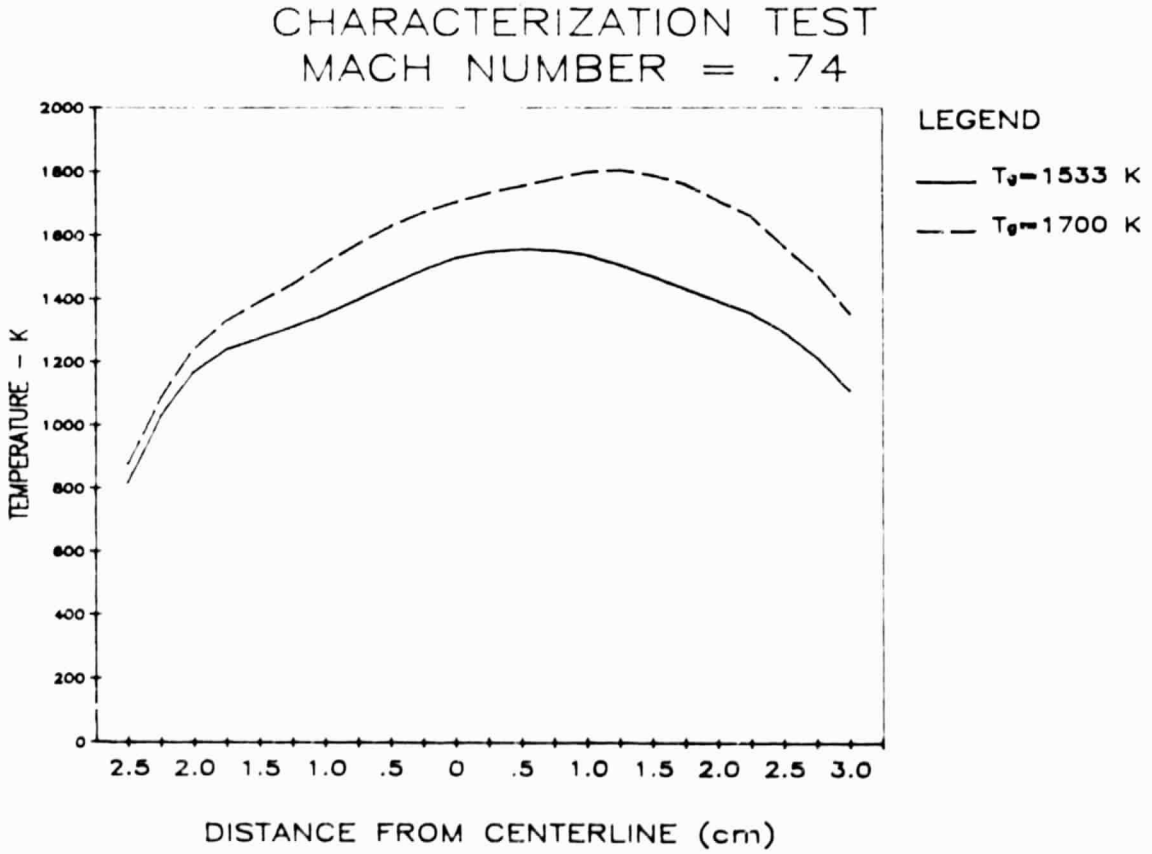

Figure 36 Combustor Temperature Profiles at Mach Number = 0.74 - Horizontal Traverse

Data was taken on a horizontal traverse for various Mach number settings. The pressure data showed that the pressure profile was essentially flat across the nozzle area. The temperature profile showed that the hot spot was not at the center of the nozzle, but had shifted 1.25 cm from the center. This profile was seen at all set points. Therefore, all data for the cylinder sensors were taken at 1.25 cm. from the center of the nozzle. Characterization data was also taken during vertical traverses at the same settings as shown in Figures 37 through 40. This data showed flat pressure profiles and temperature profiles that peaked at the center of the nozzle. From these results, it was determined that all cylinder data be taken from a horizontal traverse with the sensor at a position 1.25 cm from the center of the nozzle.

In order to evaluate the effect of radiant heat load from the combustor fireball on the cylinder in cross flow tests, a test program was conducted on a similar combustor. A radiometer was used to measure the radiant heat load to the combustor liner. The radiant heat load was found to vary from 30 to 70 Kw/m^2 depending on the run condition. The view factor from the cylinder to the fireball will be less than the view factor from the cylinder to the combustor nozzle which is 0.2. The radiant heat load to the cylinder will, therefore, be less than 0.2 X 70 = 14 Kw/m^2. That is approximately two percent of the convective heat load to the cylinder. Since the radiant heat load to the cylinder is less than two percent of the convective heat load, it will not be included in the analysis of the data.

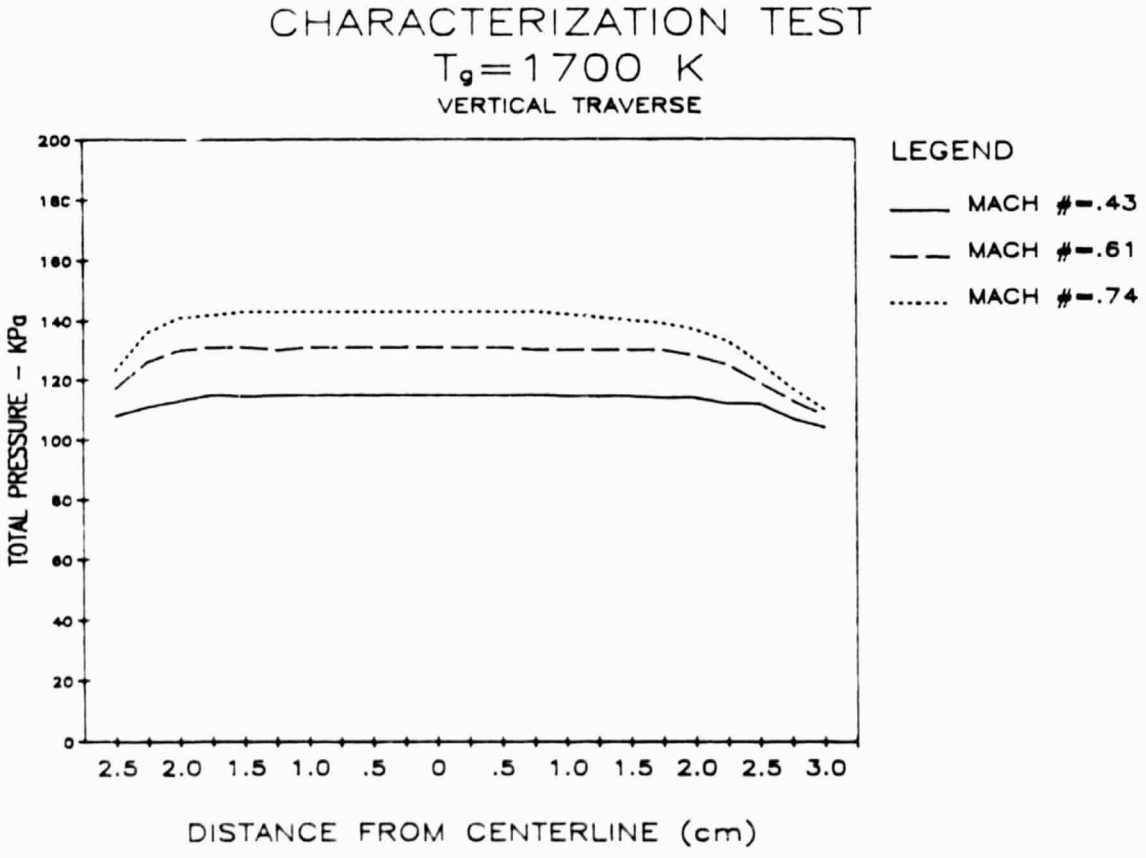

Figure 37 Combustor Total Pressure Profiles at 1700K Combustor Exit Temperature - Vertical Traverse

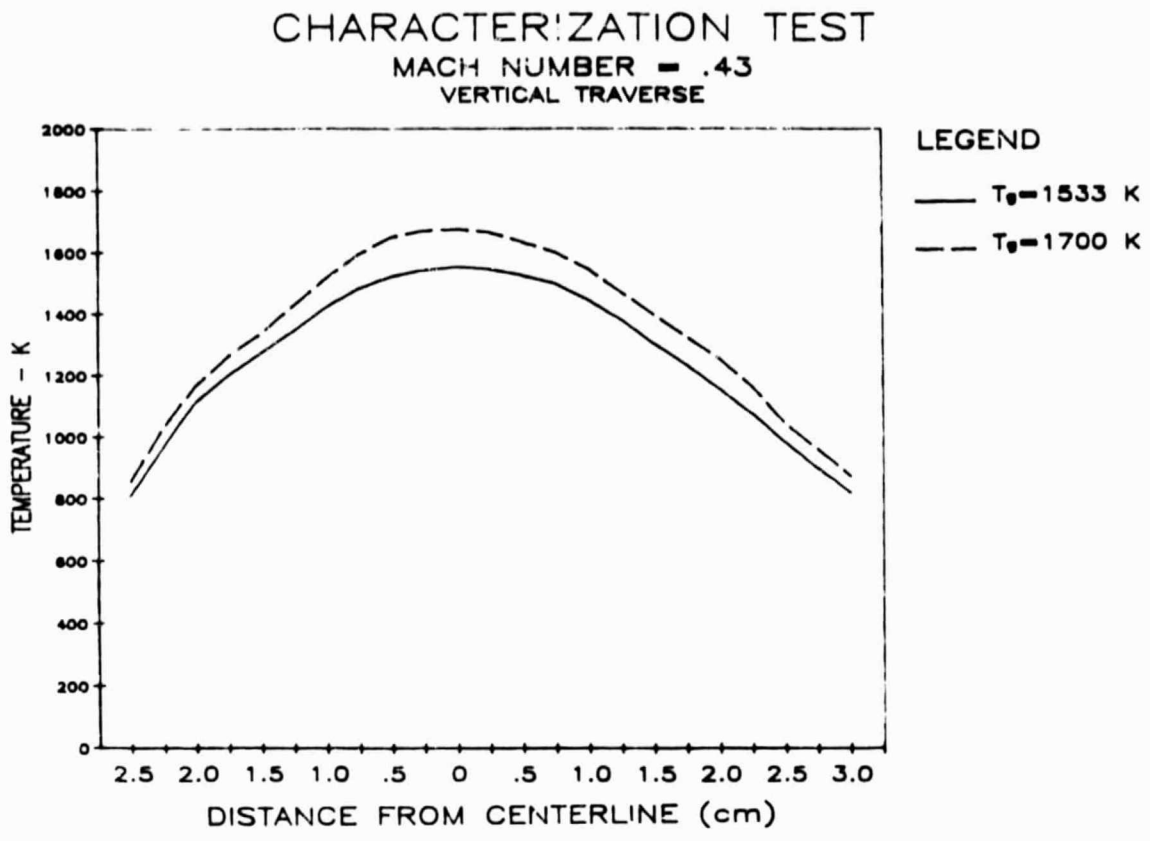

Figure 38 Combustor Temperature Profiles at Mach Number = 0.43 - Vertical Traverse

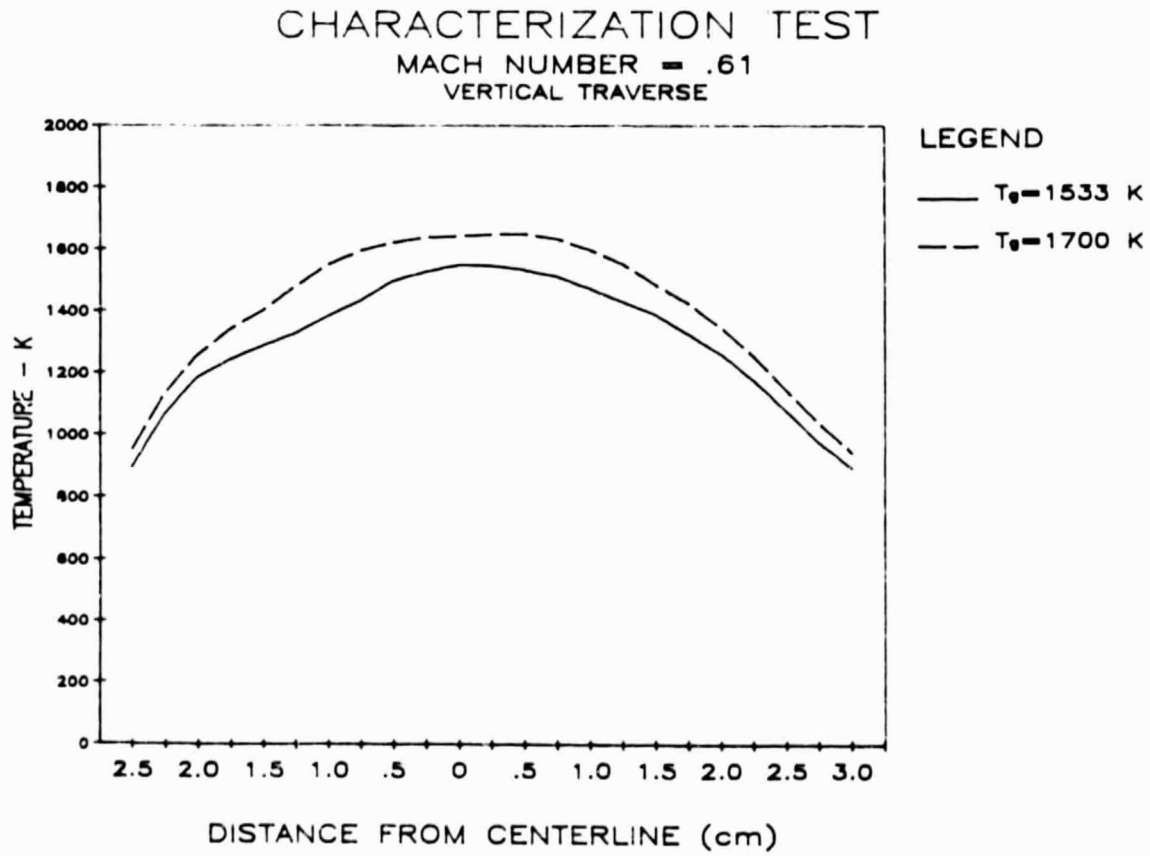

Figure 39 Combustor Temperature Profiles at Mach Number = 0.61 - Vertical Traverse

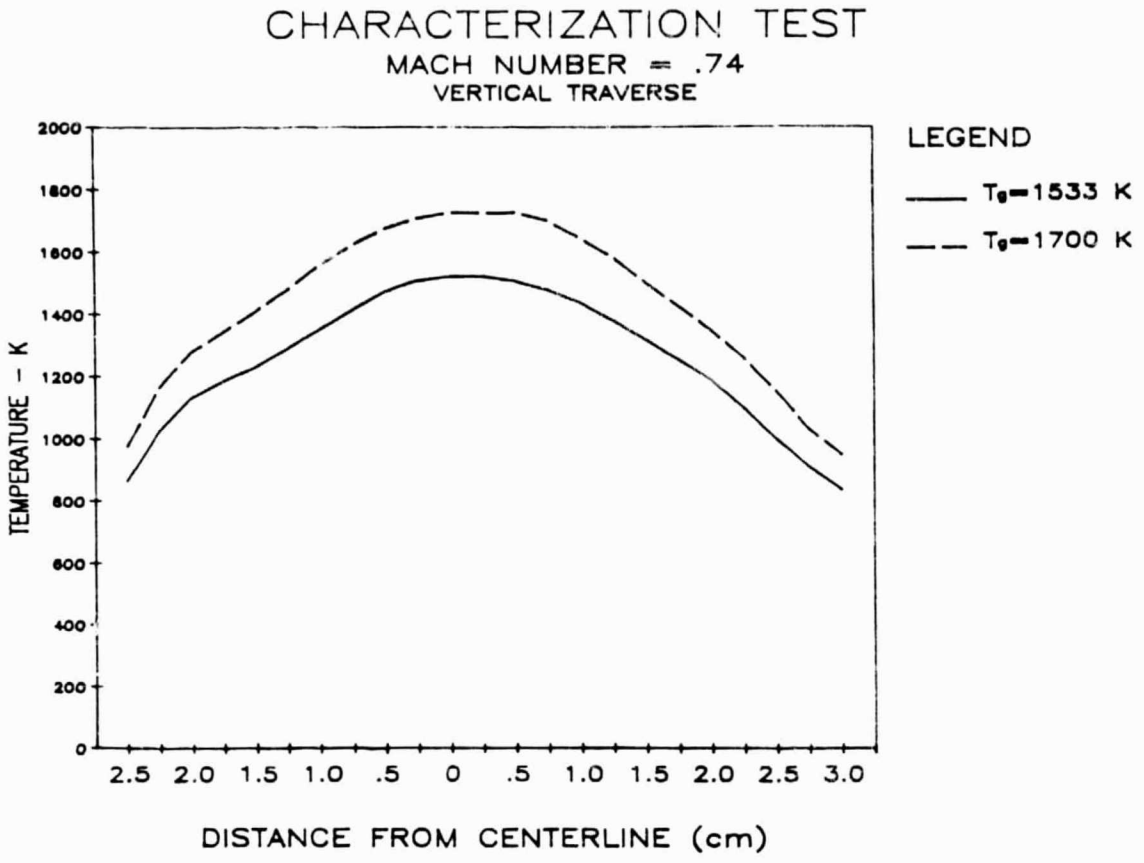

Figure 40 Combustor Temperature Profiles at Mach Number = 0.74 - Vertical Traverse

During a separate program, NASA Lewis obtained laser doppler velocimetry (LDV) data behind a similar Becon burner. It was found that once the cylinder was over 4 cm. downstream from the combustor exit, there was no interaction between the bow wake of the cylinder and the combustor exit nozzle. Figures 41 and 42 show the LDV results 5 cm. and 10 cm. downstream from the nozzle throat. The first graph in each figure shows the average velocity profile across the centerline of the flow while the second graph in each figure shows the turbulence level (standard deviation of the velocity measurements). It can be seen that 5 cm. from the nozzle both the average velocity and turbulence level are quite uniform within 1 cm. of the centerline of the flow. The data 10 cm. downstream from the nozzle exit shows the velocity profile to be more peaked and the turbulence level to be higher and less uniform.

Based on the pressure and temperature traverse data obtained at Pratt & Whitney as well as the LDV data obtained at NASA, the location 5 cm. downstream from the nozzle exit was chosen for the test location for the cylinder in cross flow experiments.

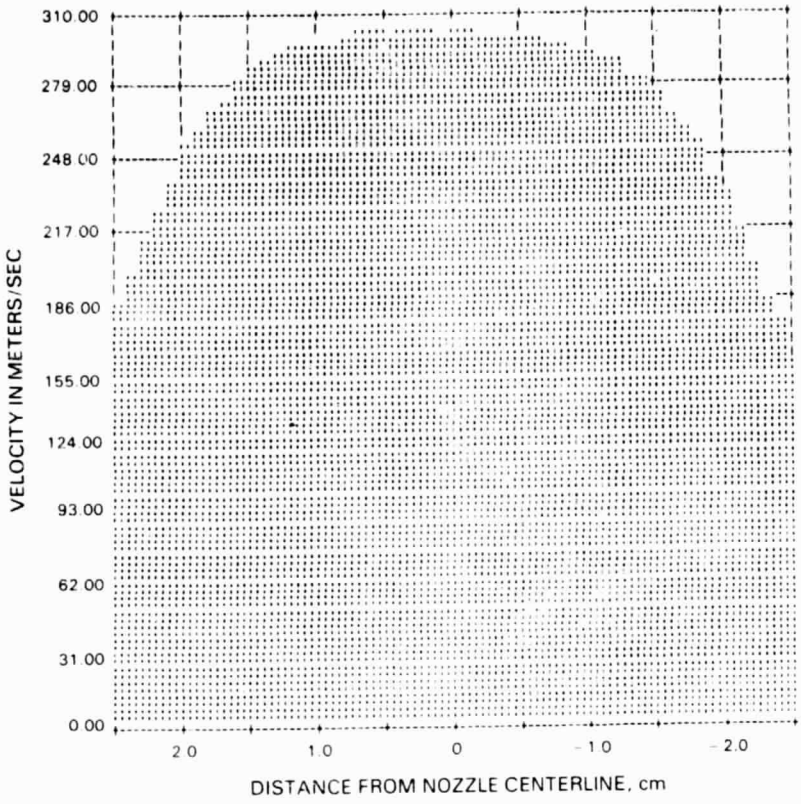

Figure 41a Laser Doppler Velocimeter Results 5 cm. Downstream from Combustor Nozzle

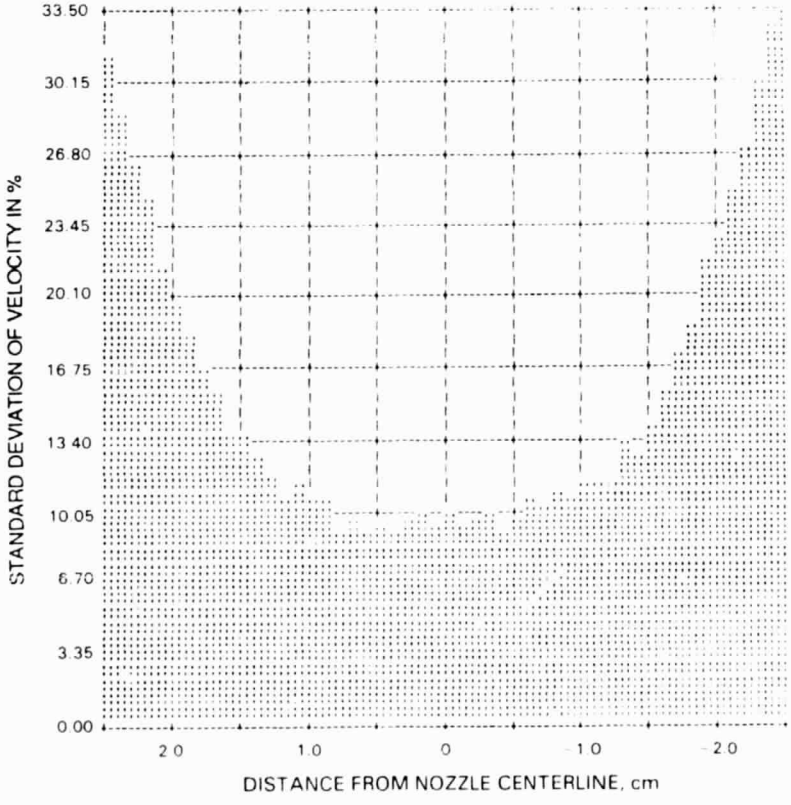

Figure 41b Laser Doppler Velocimeter Results 5 cm. Downstream from Combustor Nozzle

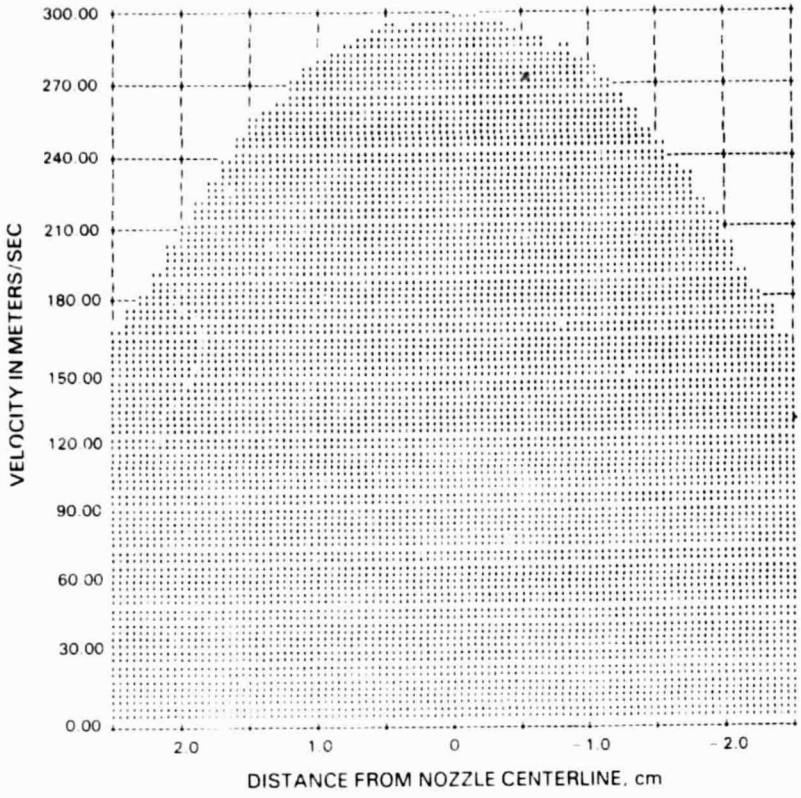

Figure 42a Laser Doppler Velocimeter Results 10 cm. Downstream from Combustor Nozzle

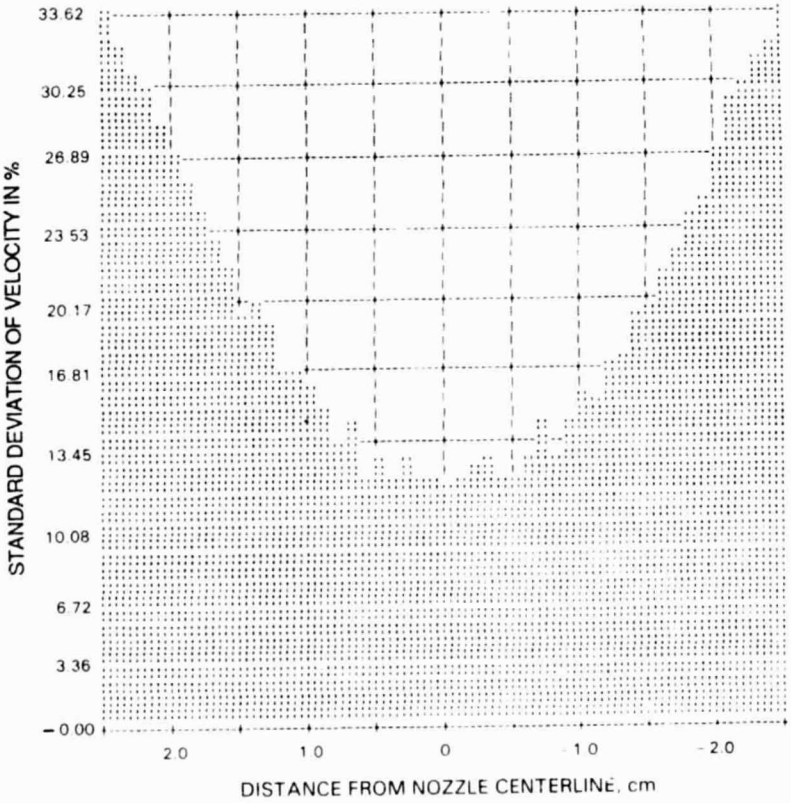

Figure 42b Laser Doppler Velocimeter Results 10 cm. Downstream from Combustor Nozzle

CYLINDER IN CROSS FLOW EXPERIMENT

Figure 43 shows an overall picture of the instrumented cylinder positioned in the combustor rig. The aspirating probe was traversed vertically and was left in the gas path until the desired temperature and Mach number were reached. The aspirating probe was then withdrawn and the instrumented cylinder was traversed to the desired Gardon gauge or embedded thermocouple sensor locations. Figure 44 shows a closeup of the cylinder at the embedded thermocouple location during testing. Cooling air was held constant for the embedded thermocouple and Gardon gauge sensors. To run the slug calorimeters for transient data, the traverse mechanism was loosened and the cylinder was manually moved rapidly into the gas path after the desired set point was reached. Coolant air, which was initially off, was later turned on under computer control to prevent the sensor from over heating. The cylinder was then withdrawn from the hot gas. The Gardon gauge was also used as a transient sensor and was traversed using the same method.

All data for the slug, Gardon gauge and embedded thermocouple sensors were taken by computer. The computer system shown in Figure 45 included a voltmeter, scanner and printer. This allowed for data inspection in near real time.

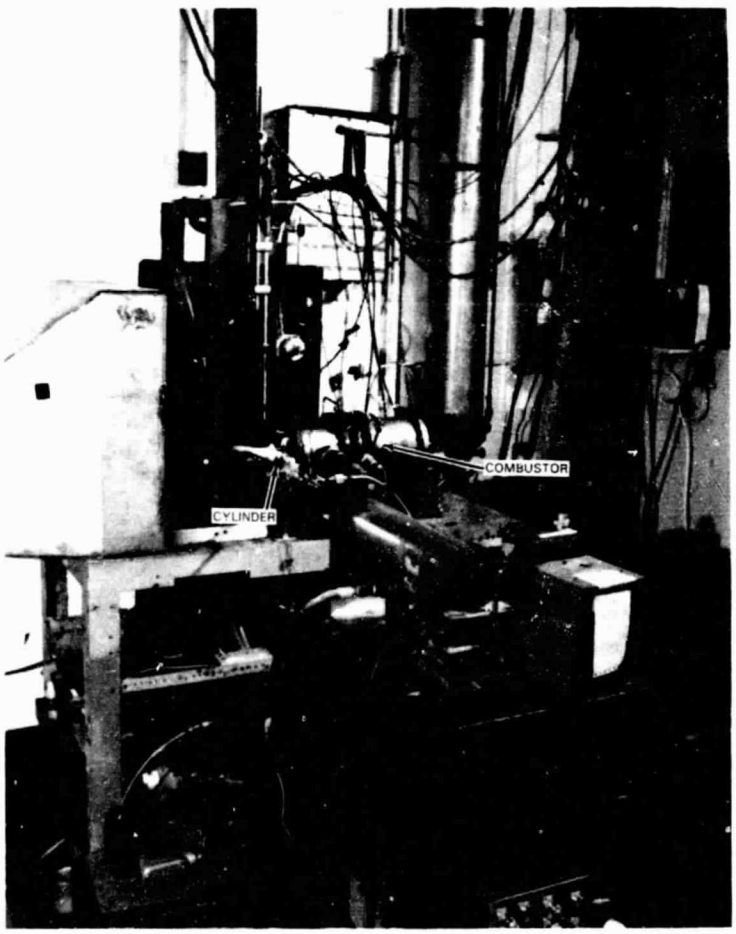

Figure 43 Overview of Cylinder Installed in Combustor Rig

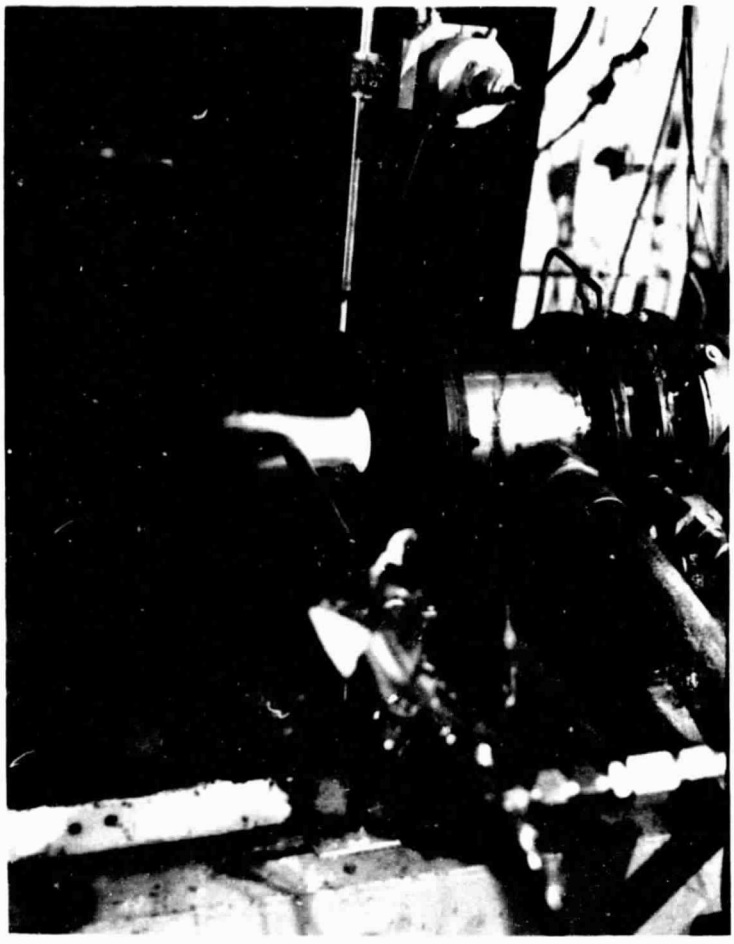

Figure 44 Closeup of Cylinder Installed in Combustor Rig

Data for the three sensors were taken, initially, with the sensors pointed directly into the gas flow. This point was arbitrarily designated as the 0 degree data point. Differences between the results given by the Gardon gauge sensors on the two test pieces prompted a study in the effects of angular variation. The embedded thermocouple sensors were rotated from 0 degree to 180 degrees as well as $\pm$ 90 degrees from the 0 degree position and the Gardon gauge sensors were rotated $\pm$ 90 degrees from the 0 degree position. Data was taken at 15 degrees intervals for both angular rotations.

The next step in the cylinder in crossflow experiment used state-of-the-art instrumentation techniques to make heat transfer measurements for comparisons with the heat flux sensors. The planned technique was to measure the ratio of the variation in the gas temperature and the cylinder surface temperature. From this ratio the heat transfer coefficient could be determined. The two probes were used at the same time and positioned as close as possible, without interfering with each other, in the gas stream. Figure 46 shows these probes during the test.

The dual wire probe was traversed into position with the traverse mechanism used for the cylinder with the heat flux sensors installed. The sputtered thermocouple probe was manually lowered into position at the same time. Data from these probes were taken and stored on a Group II wide band FM tape recorder for later analysis.

Figure 45 Computer Controlled Data Acquisition System Used for Cylinder in Cross Flow Experiment

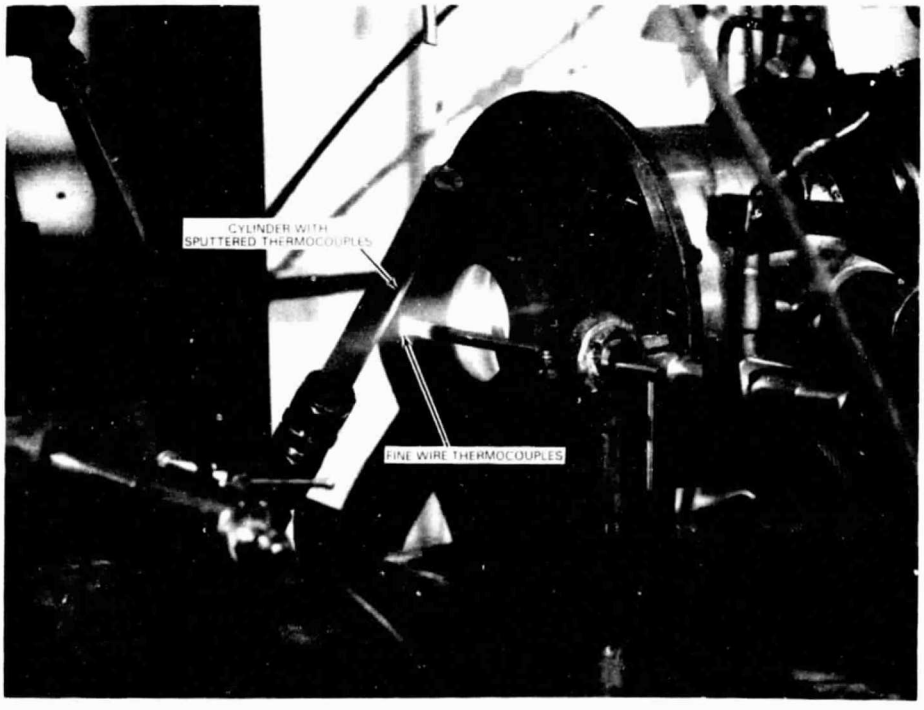

Figure 46 Cylinder with Sputtered Thermocouples and Dual Fine Wire Temperature Probe at Test

SECTION 8.0
RESULTS

RESULTS FROM HEAT FLUX SENSORS

Data for the embedded thermocouple, Gardon gauge and slug calorimeter sensors were taken at various temperature and Mach number set points. The data was initially taken at the stagnation point of the cylinder. Figures 47 and 48 show the results for each sensor on the two test cylinders. The data is presented as heat transfer coefficient vs free stream Mach number.

The Mach number was calculated based on measured pressure data using the relationship:

$$MACH = \sqrt{\frac{2}{\gamma - 1}\left[\left(\frac{P_t}{P_s}\right)^{\frac{\gamma-1}{\gamma}} - 1\right]}$$

where: P_t = total pressure
P_s = static pressure
γ = ratio of specific heats = 1.284 for the combustion products

The heat transfer coefficent was obtained from the relationship:

$$h\,(T_g - T_c) = Q/A \text{ to cylinder}$$
$$\text{or } h = Q/A \text{ to cylinder}/(T_g - T_c)$$

Where:

h = heat transfer coefficent
Q/A = heat flux to cylinder
T_g = free stream gas temperature
T_c = cylinder temperature

The heat flux to the cylinder is composed of two terms:

$$Q/A \text{ to cylinder} = Q/A_{\text{transmitted}} + Q/A_{\text{reradiated}}$$

$Q/A_{\text{transmitted}}$ is calculated from the output of the heat flux sensors. To get $Q/A_{\text{reradiated}}$, the cylinder cold side temperature and the transmitted heat flux were used to calculate cylinder hot side temperature. The reradiated heat flux was then calculated as the emittance of the cylinder times the Stefan-Boltzman constant times the difference in the fourth power of the cylinder hot side temperature and ambient temperature.

The data from the slug calorimeters was reduced by dividing the rate of change of temperature of the slug by the slug calibration constant to obtain heat flux to the slug. That heat flux was divided by the difference between gas temperature and slug temperature to obtain the heat transfer coefficient. Since the data was taken during the early part of the transient when the slug was still relatively cool, a reradiation term is not required.

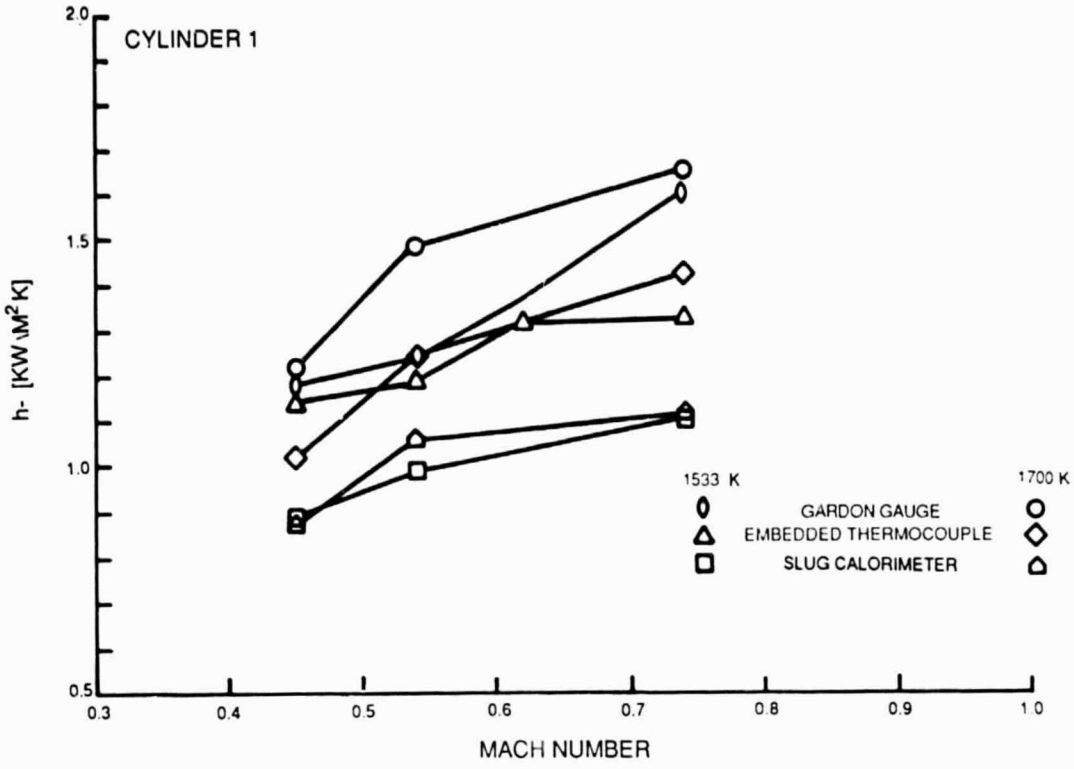

Figure 47 Test Results for Cylinder 1

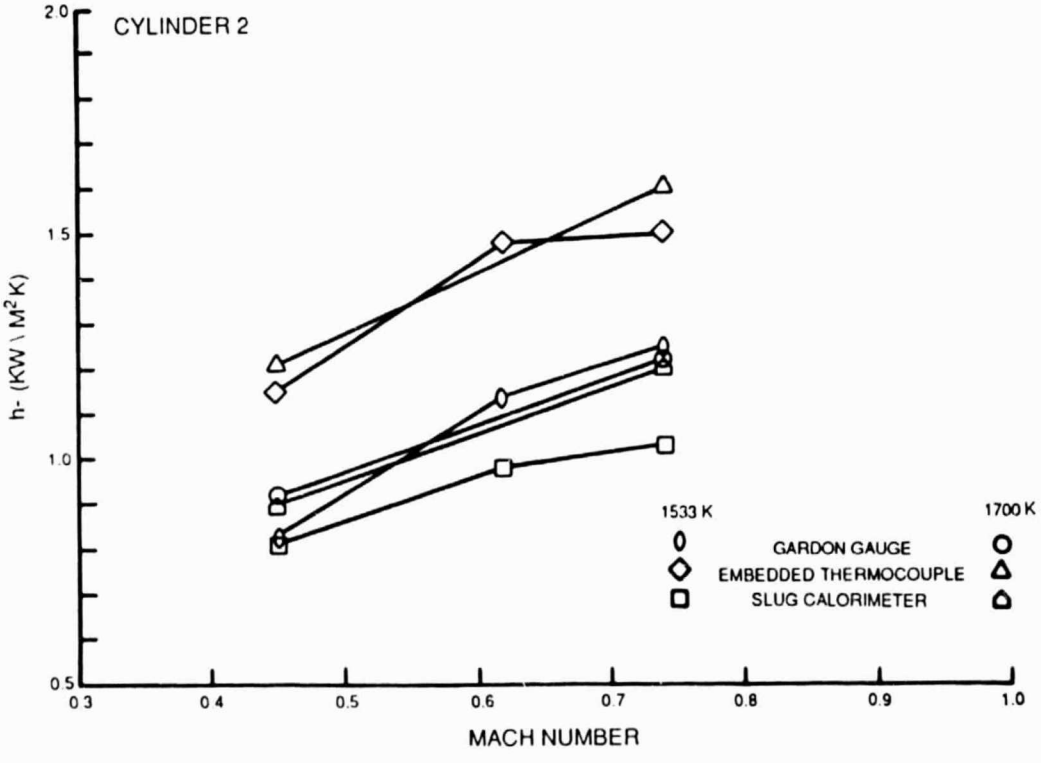

Figure 48 Test Results for Cylinder 2

It can be seen that while the trends look reasonable (heat transfer coefficient increases with increasing Mach number), there is a bias between sensors and in some cases scatter within the data from a single sensor. To clarify the situation, the embedded thermocouple and Gardon gauge on cylinder 1 were re-run. This data is shown in Figure 49. While the amount of scatter in the Gardon gauge data decreased, the systematic difference between sensors remained. The Gardon gauge sensor on cylinder 1 yielded significantly higher results than the embedded thermocouple on the same cylinder. On cylinder 2, the results are the opposite with the Gardon gauge yielding significantly lower results than the embedded thermocouple sensor. On both cylinders the slug calorimeter yielded lower results than the other sensor types. Figures 50 through 52 show comparisons between sensors of the same type. From Figure 50, it can be seen that although there is some scatter and the results from cylinder 2 are slightly higher than the results from cylinder 1, the two embedded thermocouple sensors are in reasonable agreement. Figure 51 shows a clear bias between the Gardon gauge sensors on the two cylinders with the Gardon gauge on cylinder 1 showing a much higher heat transfer coefficient than the gauge on cylinder 2. Figure 52 shows that, while the slug calorimeters read lower than the other sensor types, they yield repeatable results.

A test program was conducted during which data was acquired away from the stagnation point of the cylinders. The cylinders were rotated and data was taken at 15 degree increments. Data taken between the $\pm$ 90 degree positions are shown in Figures 53 and 54 for one embedded thermocouple and both Gardon gauge sensors. The embedded thermocouple sensor gave a bell shaped curve with the highest heat transfer coefficient at the stagnation point, as was expected. The Gardon gauge sensors, however, yielded sine wave shaped curves that were mirror images of each other. These curves also showed that the highest indicated heat flux occurred at + 60 degrees away from the stagnation point. Moreover, negative heat flux results were observed at + 75 degrees from the stagnation point. The embedded thermocouple sensors were then rotated from the stagnation point 180 degrees to the rear of the cylinder. The data from the two cylinders is shown in Figure 55. The data from the two cylinders is in good agreement with the maximum heat transfer coefficient at the stagnation point. It is also interesting to note that for these test conditions, the heat flux coefficient is virtually constant over the rear half of the cylinder. There is only a slight rise from the minimum heat transfer coefficient at the 105 degree point to the 180 degree point.

While rotational data was being taken, slippage was seen in the traverse mechanism. While this slippage was carefully observed during these rotation tests, it had not been closely monitored during the stagnation point test runs. Therefore, the stagnation point tests were re-run with careful attention paid to the traverse mechanism. It was also decided to acquire data at the 180 degree point as well as the stagnation point to take advantage of the uniform heat flux coefficient on the rear of the cylinder. Futhermore, transient data was obtained from the Gardon gauge sensors to allow comparison with the earlier slug calorimeter data. This data was reduced using the same data reduction procedures discussed earlier.

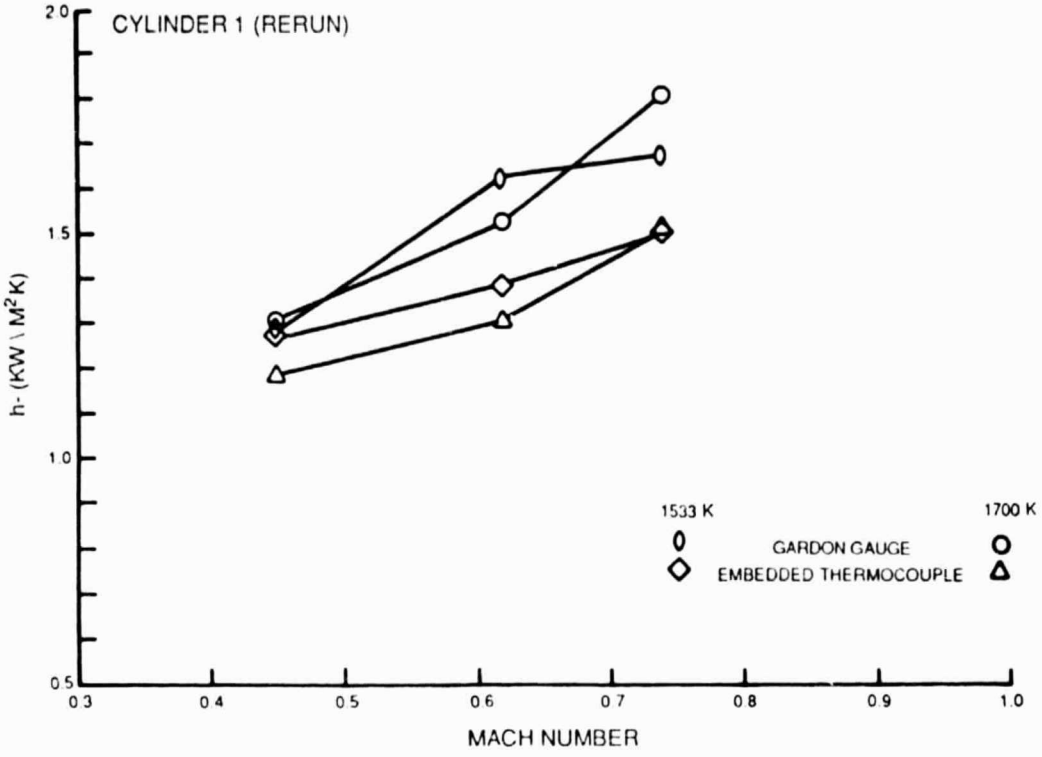

Figure 49 Test Results for the Rerun of Cylinder 1

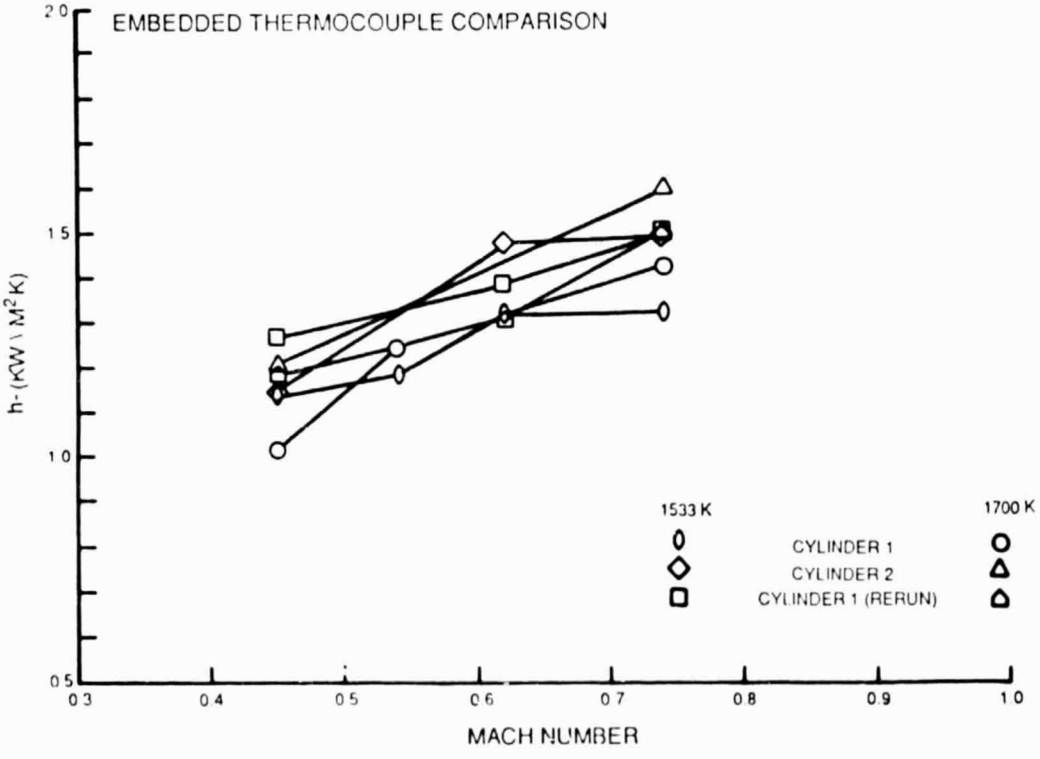

Figure 50 Comparison of Results from The Two Embedded Thermocouple Sensors

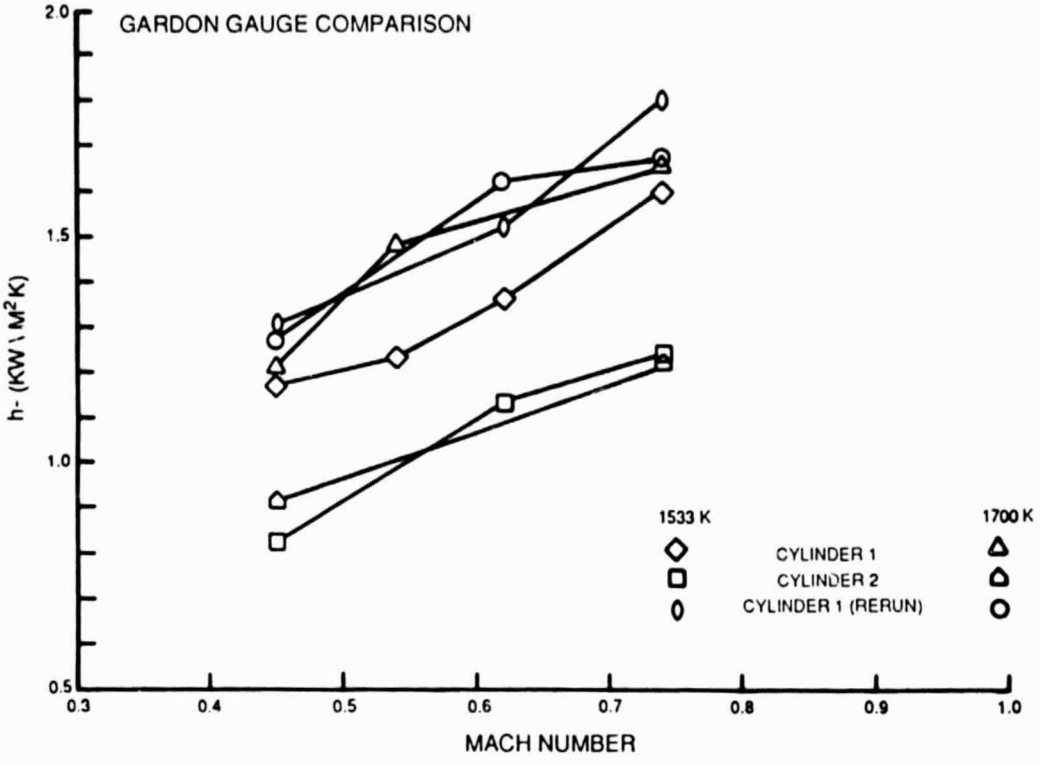

Figure 51 Comparison of Results from the Two Gardon Gauge Sensors

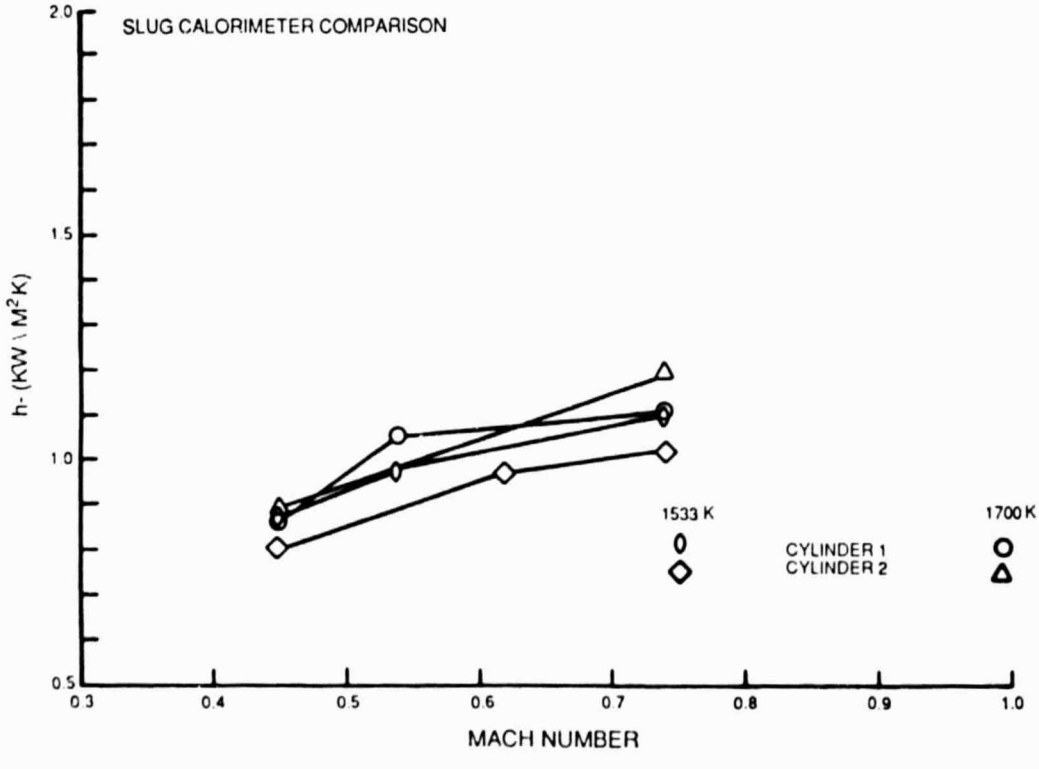

Figure 52 Comparison of Results from the two Slug Calorimeters

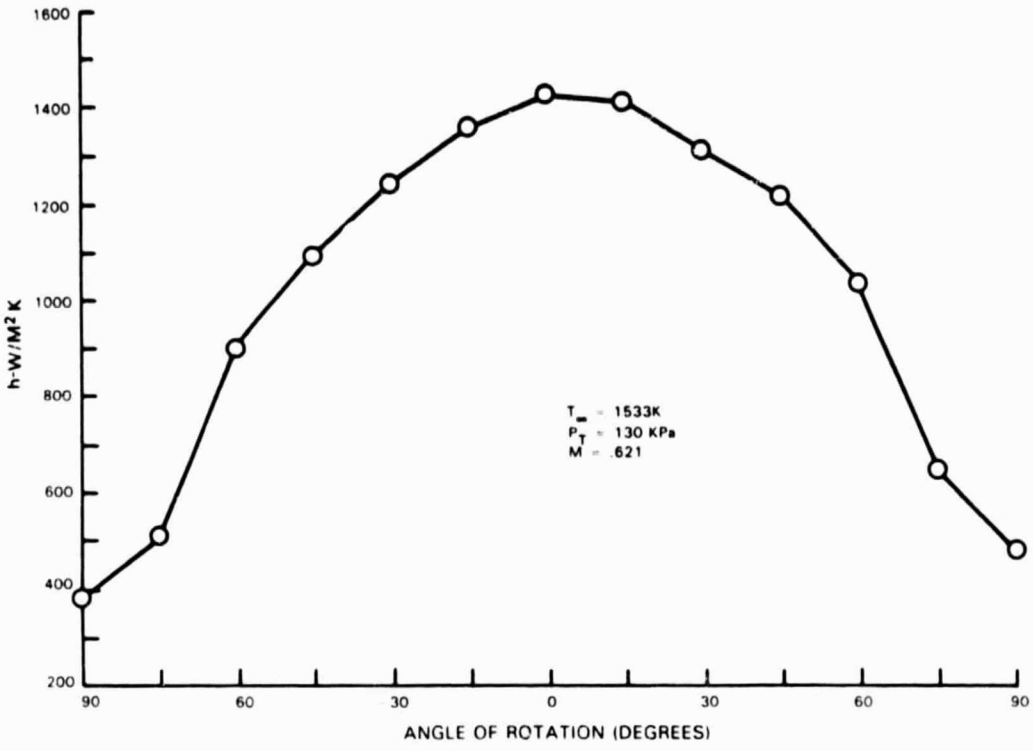

Figure 53 Effect of Rotation on Heat Flux Measured by the Embedded Thermocouple Sensors

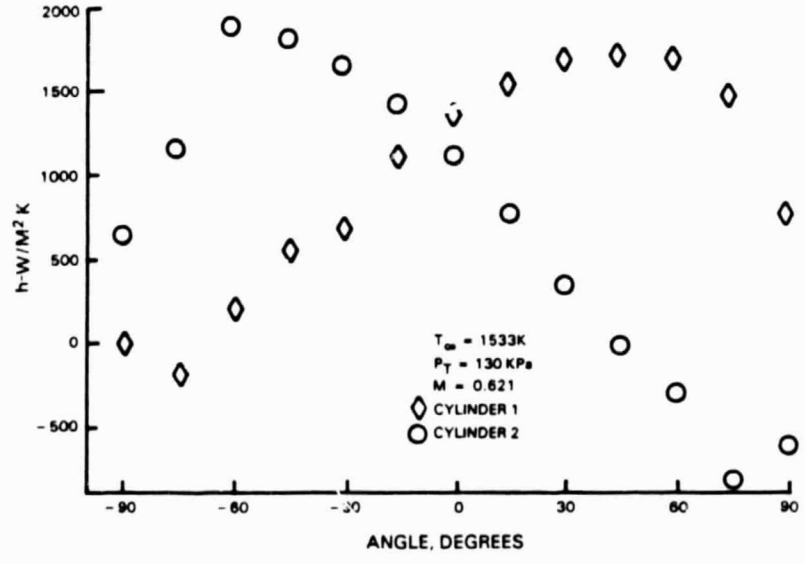

Figure 54 Effect of Rotation on Heat Flux Measured by the Gardon Gauge Sensors

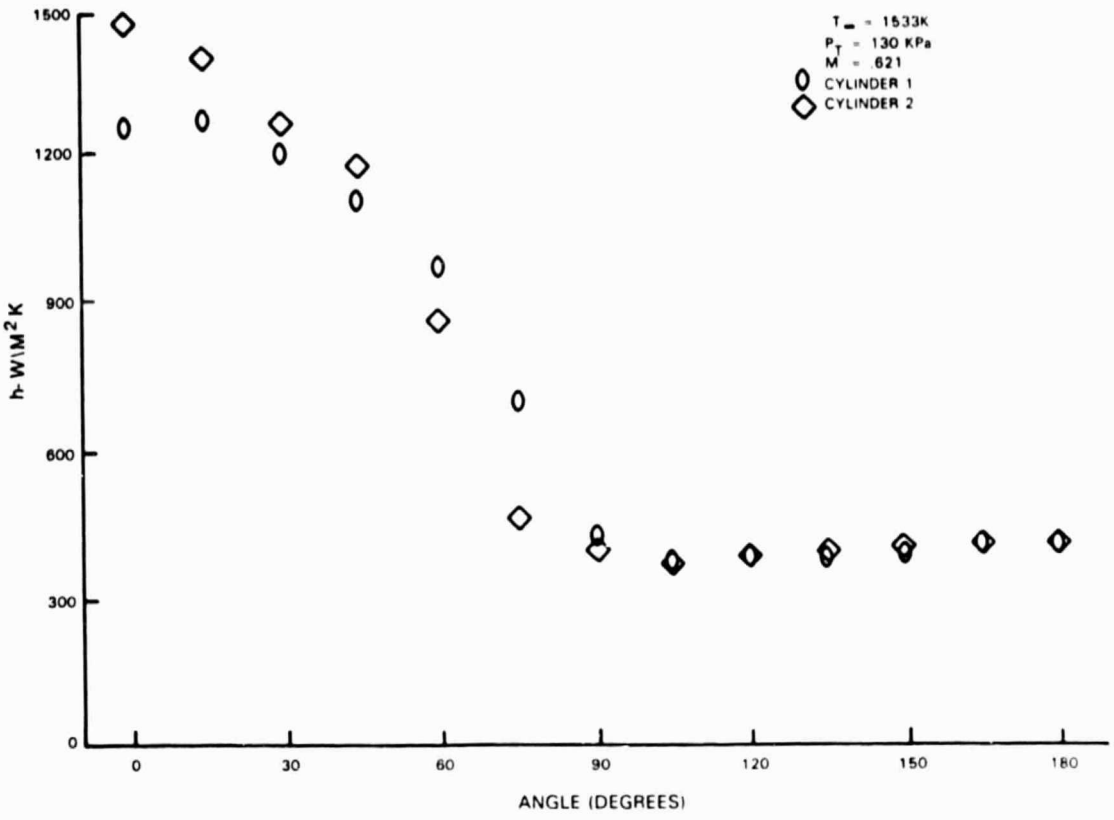

Figure 55 Data From 180 Degree Rotation of the Embedded Thermocouple Sensors

The resulting test data from cylinder 1 is shown in Figures 56 and 57 for the stagnation point and 180 degree data respectively.

It can be seen that, in general, the scatter in the data for each sensor has been reduced. At the stagnation point the Gardon gauge and embedded thermocouple are in reasonable agreement. The transient Gardon gauge data were significantly lower than the data from steady state sensors. At the 180 degree point the steady state Gardon gauge data were somewhat lower than the embedded thermocouple data. The reason for the difference between the behavior of the two sensor types at the two locations is not known.

Comparable data from cylinder 2 is shown in Figures 58 and 59. For cylinder 2, the Gardon gauge data were still significantly lower than the embedded thermocouple data at both the stagnation and 180 degree points. The scatter of the data within each sensor has, however, been reduced. The transient Gardon gauge data was low and similar to the results from the transient Gardon gauge in cylinder 1. An interesting observation is that the data from all four steady state sensors run at the 180 degree point show a decrease in heat transfer coefficient with increasing Mach number.

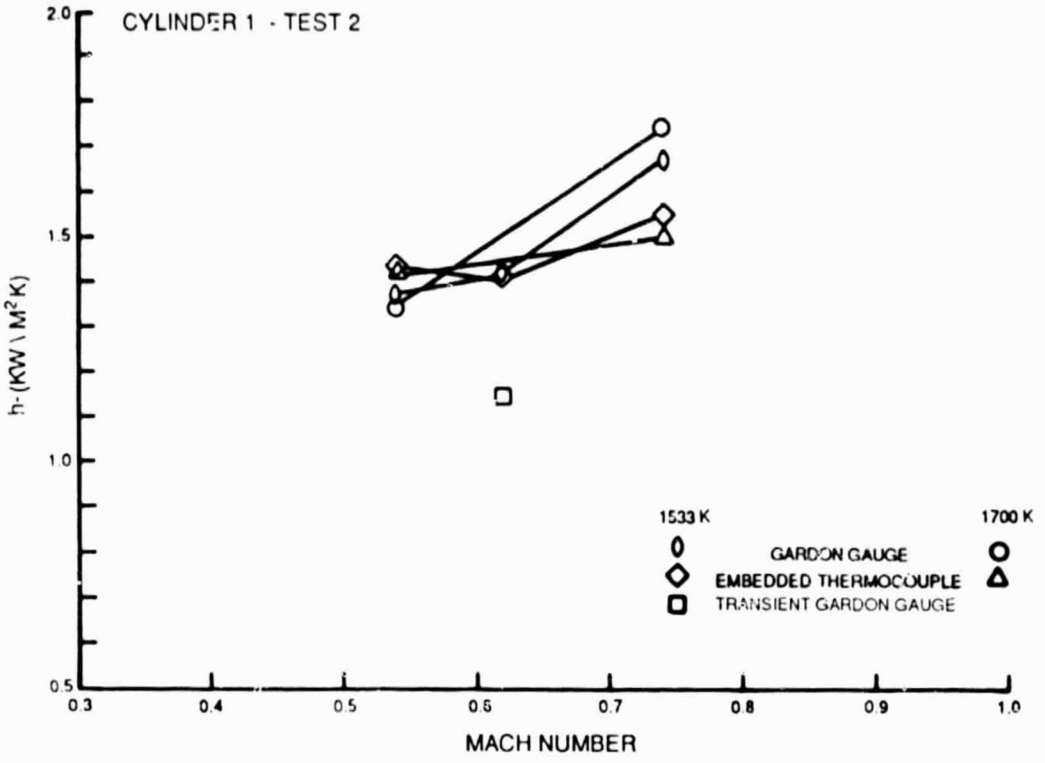

Figure 56 Stagnation Point Test Results for Cylinder 1 - Second Test Series

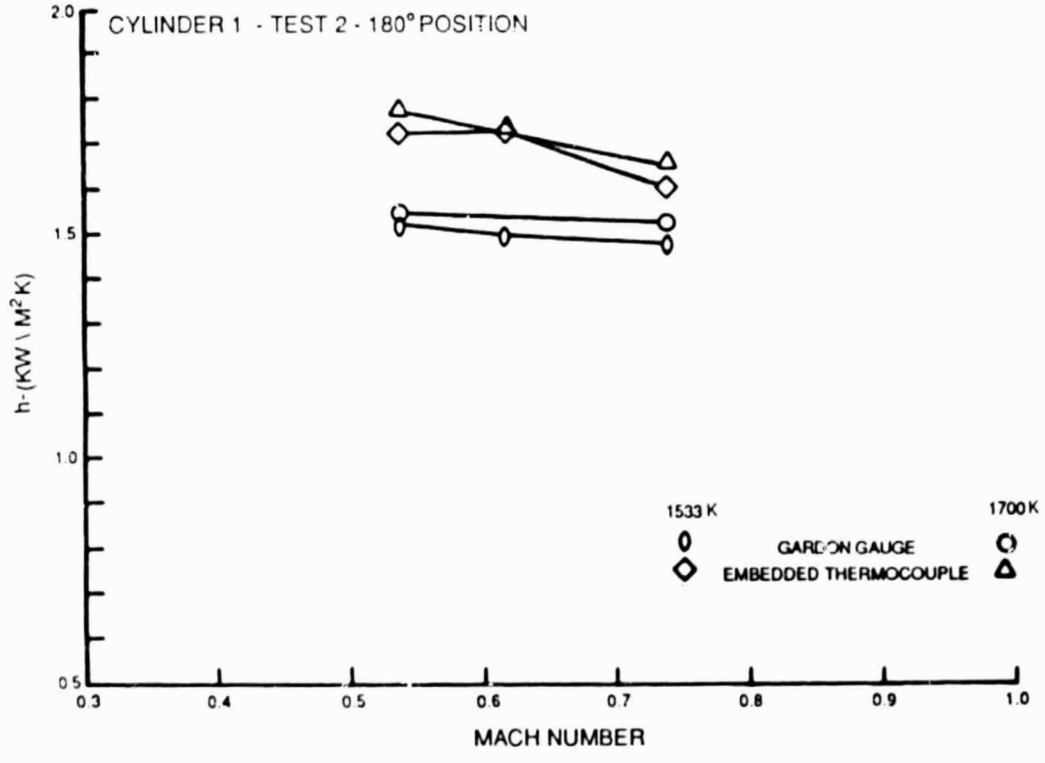

Figure 57 Data from Cylinder 1 at 180 Degrees - Second Test Series

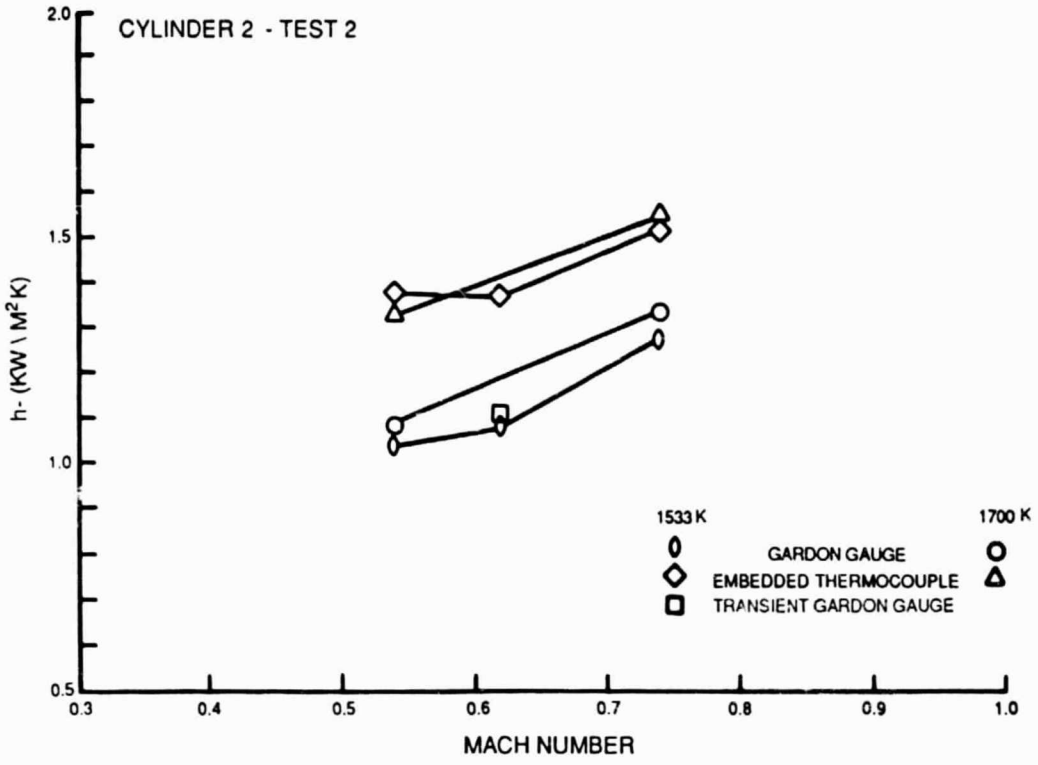

Figure 58 Stagnation Point Test Results For Cylinder 2 - Second Test Series

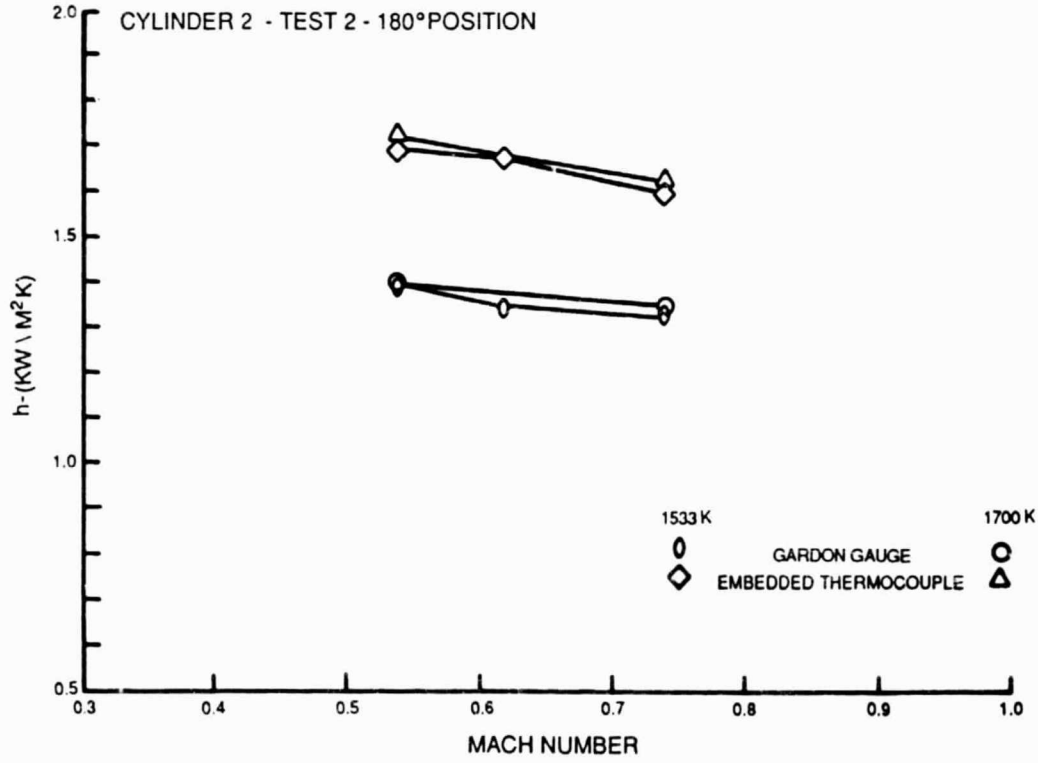

Figure 59 Data from Cylinder 2 at 180 Degrees - Second Test Series

Figures 60 to 64 show a comparison of the various sensors of the same type on different cylinders. Figures 60 and 61 show that the two embedded thermocouple sensors agree very well at both the stagnation and the 180 degree points. Figures 62 and 63 show the same data from the Gardon gauge sensors. There is a considerable disagreement between the Gardon gauge sensors on the two cylinders. The Gardon gauge on cylinder 1 compared well with the embedded thermocouple sensors. The Gardon gauge on cylinder 2 read much lower and compared fairly well with the data from the transient sensors. All of the transient sensors gave data that was significantly lower than the embedded thermocouple data and more or less in the agreement with the steady state data from the Gardon gauge in cylinder 2. Figure 64 shows a comparison of the transient data taken earlier from the slug calorimeters and the data from the transient Gardon gauges. It can be seen that the data from all the transient sensors were lower than the steady state sensors with the exception of the Gardon gauge on cylinder 2. In the repeated experiment there was a clear division of the data. The two embedded thermocouple sensors agreed well with the Gardon gauge on cylinder 1. On the other hand, the slug calorimeters from the first test series as well as the transient Gardon gauge data from the second test series agreed well with the Gardon gauge on cylinder 2.

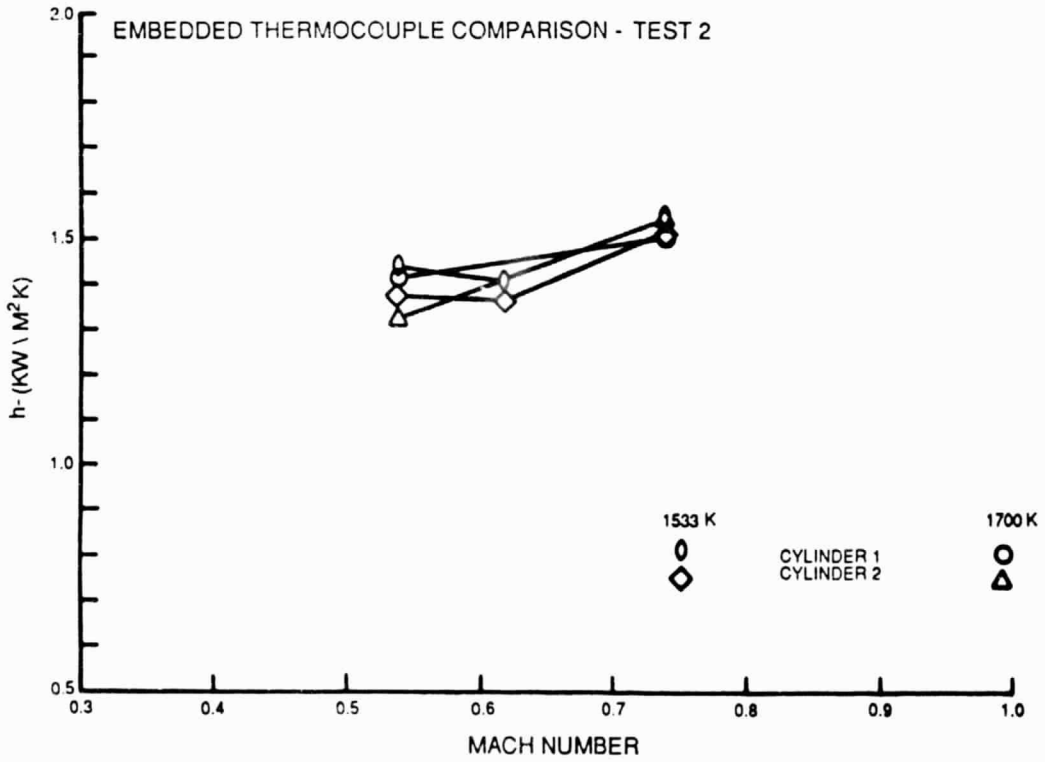

Figure 60 Comparison of Stagnation Point Results From the Two Embedded Thermocouple Sensors - Second Test Series

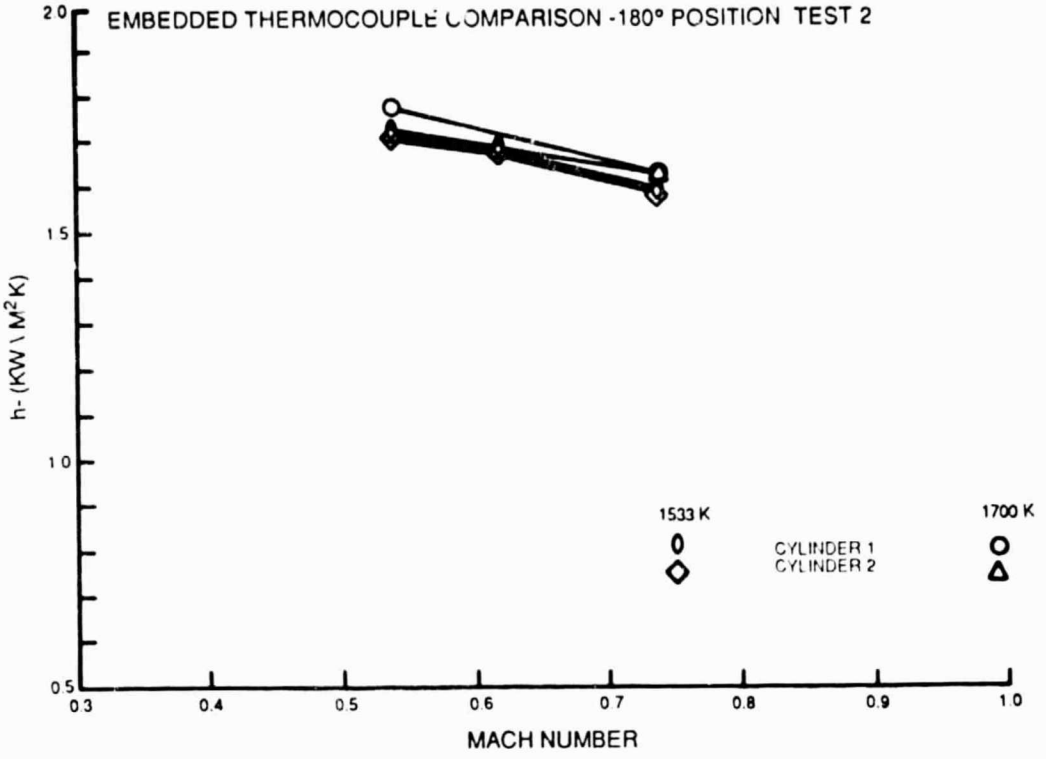

Figure 61 Comparison of Results from the Two Embedded Thermocouple Sensors at 180 Degrees

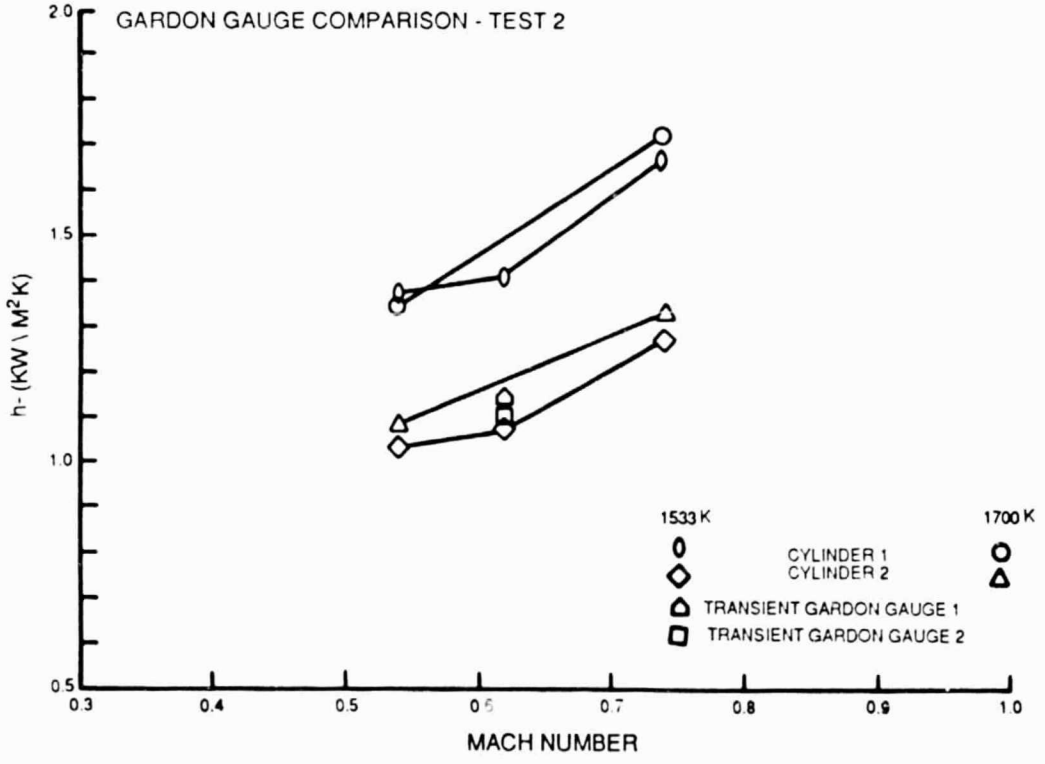

Figure 62 Comparison of Stagnation Point Results from the Two Gardon Gauge Sensors - Second Test Series

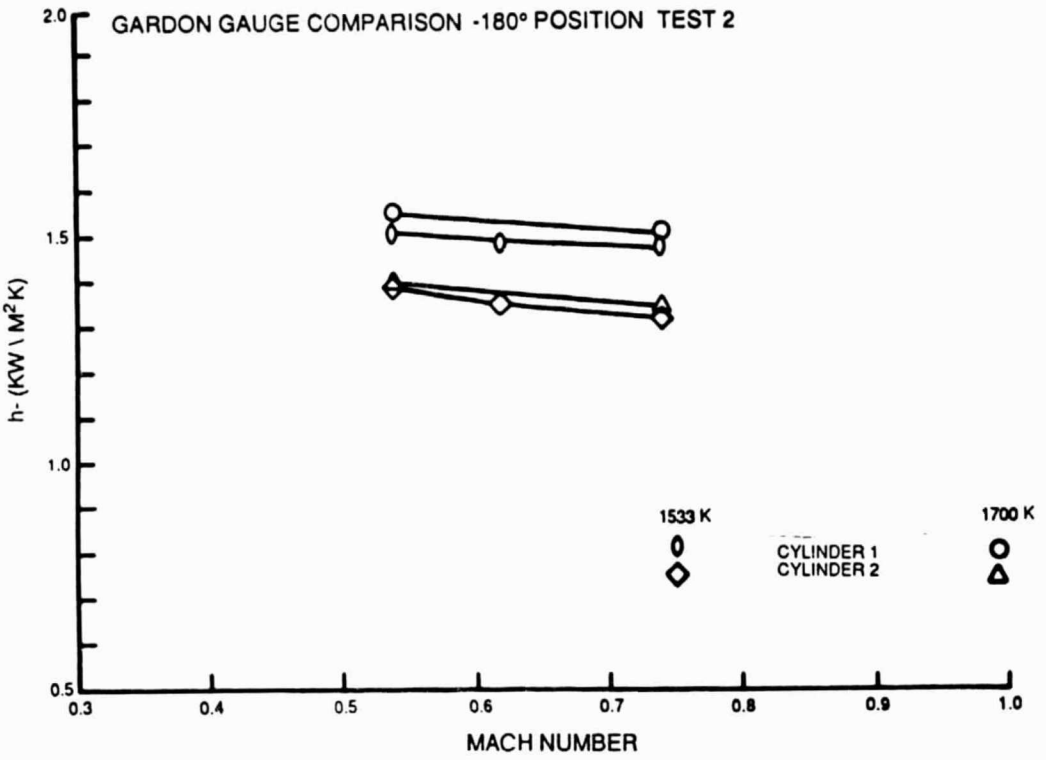

Figure 63 Comparison of Results from the Two Gardon Gauge Sensors at 180 Degrees

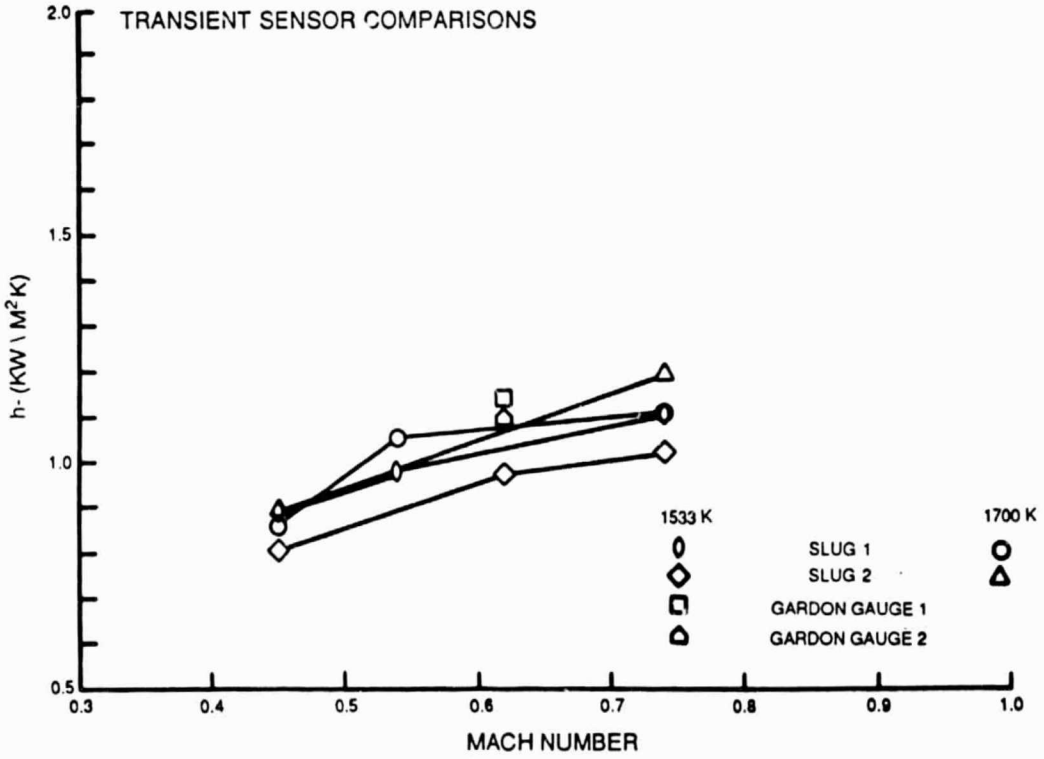

Figure 64 Comparison of Stagnation Point Data from the Four Transient Sensors

RESULTS FROM SPUTTERED THERMOCOUPLE AND DUAL FINE WIRE PROBES

After data was taken with the instrumented cylinders, tests were run with the sputtered thermocouple and dual fine wire probes. The purpose of this part of the experiment was to obtain heat transfer measurements and compare the results from this method with the data obtained from the instrumented cylinders. The combined use of fine wire gas thermocouples and sputtered surface thermocouples is an interesting extension of the one-dimensional transient sensor involving the measurement of the dynamic temperature variation under "steady state" operating conditions.

The variation in the gas temperature is determined with a fine-wire thermocouple while the variation in surface temperature is measured with a foil or sputtered thin film thermocouple applied to the surface. It can be shown that the relative amplitude of the two temperature oscillations at any given frequency is given by:

$$\left| \tilde{T}_s / \tilde{T}_g \right| = 1 \Big/ \sqrt{1+2\beta+2\beta^2}$$

where:

$\beta = (1/n) \sqrt{\pi (f)(Cp)(\rho)(K)}$,
$\tilde{T}_s$ = amplitude of component surface temperature oscillation,
$\tilde{T}_g$ = amplitude of free stream gas temperature fluctuation,
h = surface heat transfer coefficient,
f = frequency of the periodic wave,
Cp, ρ, K = material properties.

For all conditions of interest in this program $\beta \gg 1$. Therefore,

$$\left| \tilde{T}_s / \tilde{T}_g \right| \approx 1/\sqrt{2\beta^2}$$

$$\left| \tilde{T}_s / \tilde{T}_g \right| \approx n/\sqrt{2\pi (f)(Cp)(\rho)(K)}$$

Therefore, for a solid with known material properties, in any frequency band the ratio of the magnitude of the surface thermal wave to the gas stream thermal wave is linearly related to the heat transfer coefficient. The heat transfer coefficient can, therefore, be directly calculated from the relative wave amplitudes. The useful part of the gas temperature wave is that containing components which:

1. contain sufficient power to induce measurable surface temperature fluctuations;

2. are of wavelengths sufficiently long that the heat transfer coefficient at each temperature can be considered steady and equal to the time averaged heat transfer coefficient;

3. have thermal wavelengths $\lambda_T = 2\sqrt{\pi (K)/(f)\ (\rho)(Cp)}$ in the solid small enough for the solid to be considered semi-infinite and to give adequate spatial resolution but large enough for the thermal wave to be uneffected by minute irregularities in the solid.

For the cylinder in cross flow test, the spatial resolution desired from the measurement (1.5mm) dictates a λ_T of less than 1.5 mm. This dictates f is greater than 20 hertz. Signal strength considerations will dictate a maximum frequency of approximately 100 hertz or $\lambda_T \approx .7$mm.

Two sets of probes were used in this experiment. However, due to various experimental problems little useful data was produced. In the first test series, the dual wire temperature probe was hit by a carbon particle from the combustor and failed (Figure 65) before any useful data could be collected. The thermocouple probe was replaced and testing continued. Data was obtained during the second test series. Data from the thermocouples were amplified and recorded on magnetic tape. Post test, the data was played back through various bandpass filters.

The frequency spectra from a typical test point are shown in Figures 66 through 68 for the .076 mm, .25 mm, and sputtered thermocouple.

Figure 65 Damaged Fine Wire Thermocouple Probe

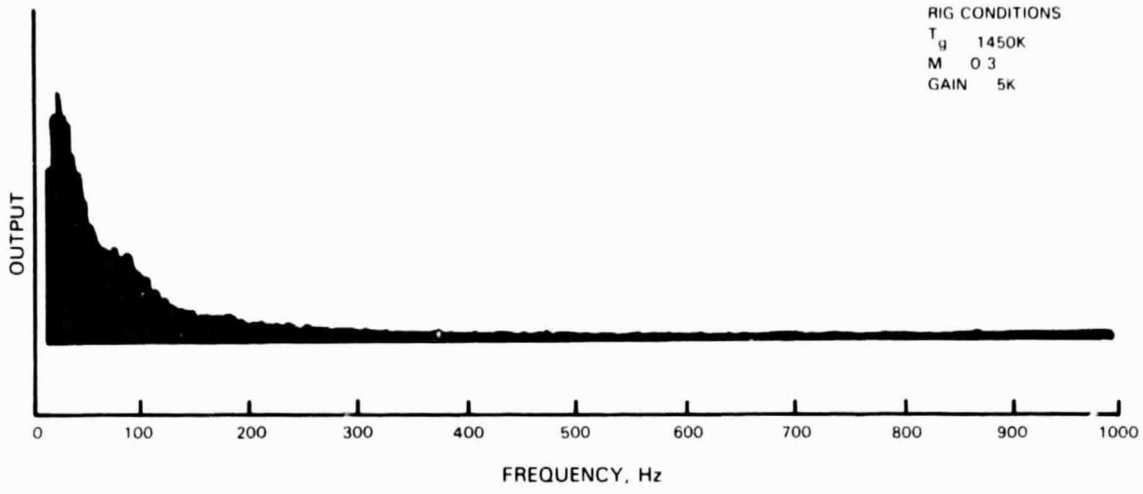

Figure 66 Frequency Spectrum from .076 mm Fine Wire Thermocouple

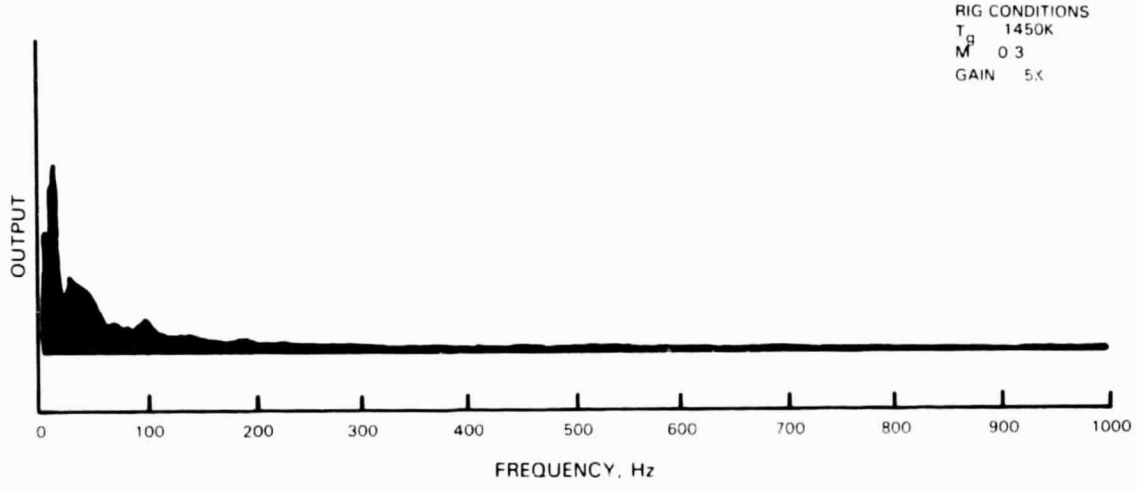

Figure 67 Frequency Spectrum from .25 mm Fine Wire Thermocouple

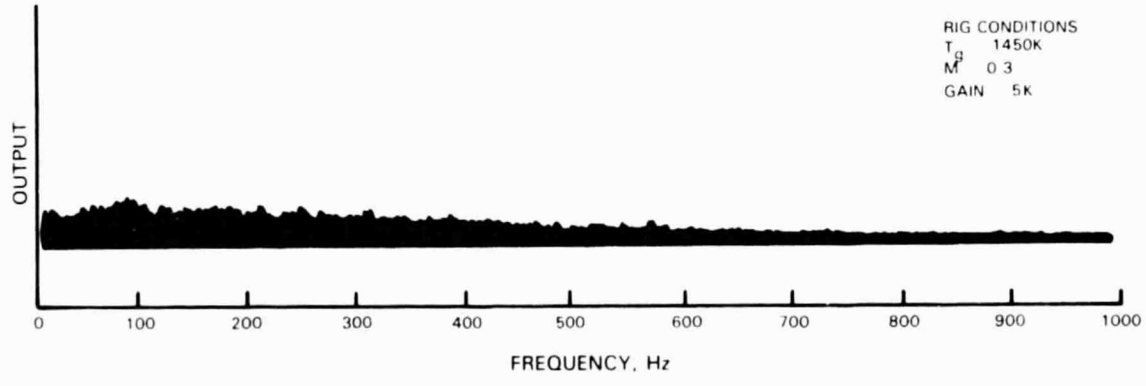

Figure 68 Frequency Spectrum from Sputtered Thermocouple Surface Temperature Sensor

In order to obtain the true RMS variation in gas stream temperature, it is necessary to correct the raw fine wire thermocouple data for the finite time response of the fine wire thermocouples. Dils and Follansbee (Reference 24) showed that the time response of fine wire thermocouples can be calculated as

$$\tau = \frac{\rho_w C_w d_w 1.5}{1.92 K_g \sqrt{\frac{\rho_g V}{\mu_g}}}$$

where:

ρ_w	=	Wire density	Kg/m^3
C_w	=	Wire specific heat	J/KgK
d_w	=	Wire diameter	m
K_g	=	gas thermal conductivity	J/m sec K
ρ_g	=	gas density	Kg/m^3
μ_g	=	gas viscosity	Kg/m sec
V	=	Free stream velocity	m/sec

The material properties used are listed in Table I, as are the resulting thermocouple time constants. It can be seen that there is negligible difference between the 1530 K and 1700 K results. From the time constant, the thermocouple cutoff frequency, $f_c = \frac{1}{2\pi\tau}$, can be calculated.

TABLE I
DATA RELATED TO RESPONSE OF FINE WIRE THERMOCOUPLES

Parameter	.076 mm Wire			.25 mm Wire			UNITS
T_{gas}	1530	1530	1700	1530	1530	1700	K
Mach	.32	.45	.32	.32	.45	.32	
ρ_w			19085				Kg/m^3
c_w	191.8	191.8	196.8	191.8	191.8	196.8	J/KgK
d_w		7.6×10^{-5}			2.5×10^{-4}		m
K_g	.0855	.0855	.0896	.0855	.0855	.0896	$\frac{J}{m\ Sec.\ K}$
ρ_g	.234	.234	.211	.234	.234	.211	Kg/m^3
μ_g	5.35×10^{-5}	5.35×10^{-5}	5.54×10^{-5}	5.35×10^{-5}	5.35×10^{-5}	5.54×10^{-5}	$\frac{Kg}{m\ Sec}$
V	239	335	251	239	335	251	m/sec
τ	.0144	.0122	.0148	.0876	.0742	.0901	sec
f_c	11.0	13.0	10.8	1.82	2.14	1.77	Hz

Above this cutoff frequency, the response of the thermocouples will fall off 6 Db per octave. Figure 69 shows the resulting thermocouple response curves. This data can then be used to correct the data from the fine wire thermocouples to obtain an estimate of the true RMS variation in gas temperature. That data, as well as the RMS variation in surface temperature measured by the sputtered thermocouple sensor, is shown in Table II.

The density of the NiCoCrAlY rod was determined experimentally. Neither the specific heat nor the thermal conductivity of NiCoCrAlY is know exactly, but it was felt that these parameters could be estimated reasonably accurately based on the similarity of this alloy to materials with known properties.

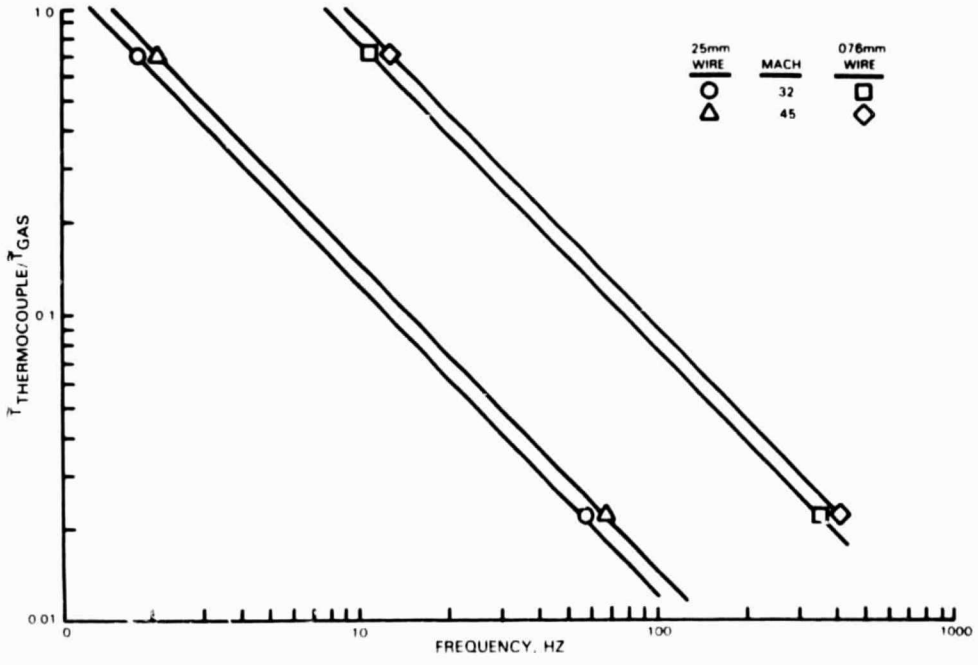

Figure 69 Calculated Response Functions For Fine Wire Thermocouple Probes

Figure 70 shows the estimated properties used for NiCoCrAlY. The thermal data from Table III can be combined with the material properties in Figure 70 to calculate the heat transfer coefficient using the result derived earlier:

$$h = |\tilde{T}_s/\tilde{T}_g|\sqrt{2\pi f C_p \rho K}$$

The resulting data is shown in Table III. It can be seen that the heat transfer coefficient calculated based on the gas temperature variation measured by the 0.25 mm wire averages approximately 70% higher than the heat transfer coefficient calculated based on the 0.076 mm fine wire. All of the data obtained by this technique yielded results that were much higher (often by more than an order of magnitude) than the results from any of the other methods used to determine the heat transfer coefficient.

Because of the unrealistically high data obtained from the first sputtered cylinder, it was decided to run a second cylinder to try to repeat the data. Some of the films on the second cylinder had peeled off pretest and, unfortunately, all the remaining films failed (Figure 71) during the first heating cycle, before any data could be obtained.

TABLE II
FINE WIRE AND SPUTTERED THERMOCOUPLE DATA

T_{gas} K	Mach Number	Frequency Band Hz	.076 Mil Fine Wire TC			.25 Mil Fine Wire TC			Sputtered Surface TC	
			μVolts	$\tilde{T}$uncorrected K	$\tilde{T}$corrected K	μVolts	$\tilde{T}$uncorrected K	$\tilde{T}$corrected K	μVolts	$\tilde{T}$ K
1530	.32	25±2.5	25	2.34	7.82	7	0.66	13.11	35	1.79
		50±5	20	1.88	12.36	5	0.47	19.05	60	3.14
		100±10	125	11.73	135.	35	3.28	274.	260	13.33
1700	.32	25±2.5	25	2.34	7.82	7.5	0.71	14.11	16.3	0.84
		50±5	18.75	1.76	11.59	5	0.47	19.05	30	1.54
		100±10	131.3	12.32	142.	30	2.82	235.	130	6.67
1530	.45	25±2.5	20	1.88	5.14	7	0.66	10.93	5	0.33
		50±5	18.75	1.76	9.78	4	0.38	12.59	9.4	0.61
		100±10	112.5	10.56	117.	30	2.82	191.	40	2.61

TABLE III
HEAT TRANSFER BASED ON FINE WIRE AND SPUTTERED THERMOCOUPLE DATA

T_{gas} K	Mach Number	$T_{Cylinder}$ K	Bandwith Hz	Cp J/KgK	ρ Kg/m^3	K J/m sec K	.076 Mil Wire		.25 Mil Wire	
							$\tilde{T}s/\tilde{T}g$	h KW/m^2 K	$\tilde{T}s/\tilde{T}g$	h KW/m^2 K
1530	.32	1170	25±2.5	643	7100	23.4	.23	29.7	.14	17.9
			50±5				.25	46.5	.16	30.2
			100±10				.10	25.5	.049	12.6
1700	.32	1210	25±2.5	653		23.9	.11	14.2	.060	7.9
			50±5				.13	24.8	.081	15.1
			100±10				.047	12.4	.028	7.5
1530	.45	980	25±2.5	534		18.6	.064	6.8	.030	3.2
			50±5				.062	9.3	.048	7.2
			100±10				.022	4.7	.014	2.9

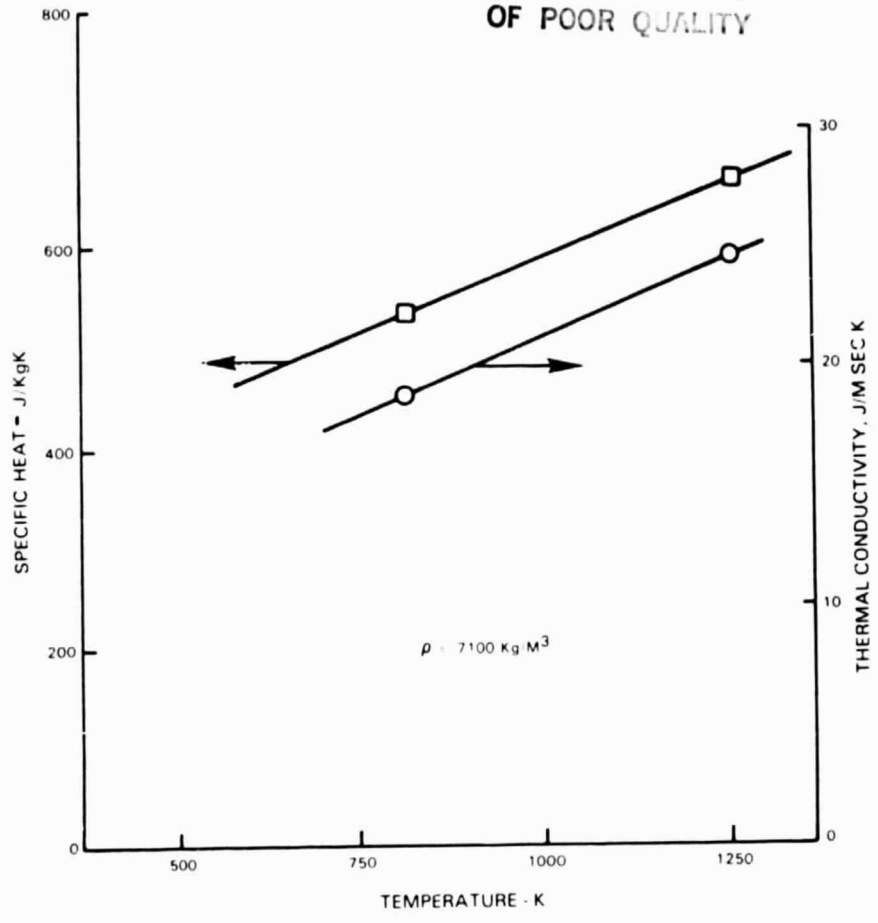

Figure 70 Estimated Properties for NiCoCrAlY

Figure 71 Cylinder with Failed Sputtered Thermocouple Sensors

SECTION 9.0
POST TEST ANALYSIS

After the rig testing was complete, a program of laboratory testing and analysis was initiated. The purposes of the post test program were to compare the data we obtained with other test data and theoretical results and to investigate the causes of some of the unusual test results.

INSPECTION AND POST-TEST CALIBRATION

After the cylinder in crossflow experiment was completed, all probes were inspected. The heat flux sensors on both test cylinders had survived the test and were in good condition. As mentioned earlier, the first dual fine wire thermocouple had failed during test while the second probe survived intact. One of the cylinders with sputtered thermocouples seemed to have survived the test program, while all sputtered sensors on the other cylinder had failed. During post test inspection of the sputtered sensors on the surviving cylinder, it was found that there was a reversal of the leadwires. The rhodium wire was attached to the platinum film and the platinum wire was attached to the rhodium film. This would result in an erroneous temperature based on differential temperatures. This does not, however, explain the unrealistically high heat transfer coefficient result obtained based on the sputtered thermocouples.

Post test calibrations were performed on all steady state heat flux sensors on the two cylinders. All sensors repeated well. Figures 72 to 75 show comparisons of the pretest and post test calibrations of the four steady state sensors. It can be seen that there is no significant difference between the pre and post test results.

COMPARISON WITH THEORY AND OTHER DATA

Frossling (Reference 5) showed that for nonturbulent flows the Nusselt number and the Reynolds number are related by the simple relationship: $Nu = .9443\sqrt{Re}$ at the stagnation point of a cylinder in cross flow. So:

$$\frac{hd}{K_f} = .9443\sqrt{\frac{V_\infty d \rho_f}{\mu_f}}$$

where:

- h = Heat transfer coefficient
- d = diameter of cylinder
- K_f = gas thermal conductivity evaluated at film temperature
- V_∞ = free stream gas velocity
- ρ_f = gas density evaluated at film temperature
- μ_f = gas viscosity evaluated at film temperature

or:

$$h_{theory} = .9443\ K_f\sqrt{\frac{V_\infty \rho_f}{d \mu_f}}$$

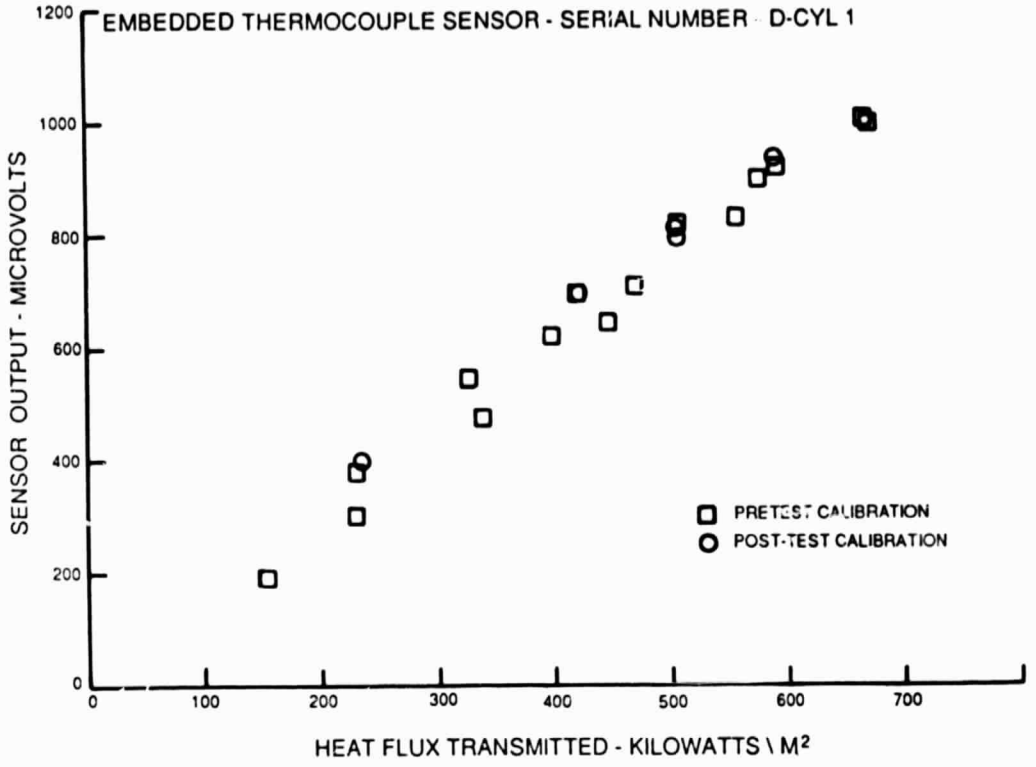

Figure 72a Post Test Calibration of Embedded Thermocouple Sensor in Cylinder 1

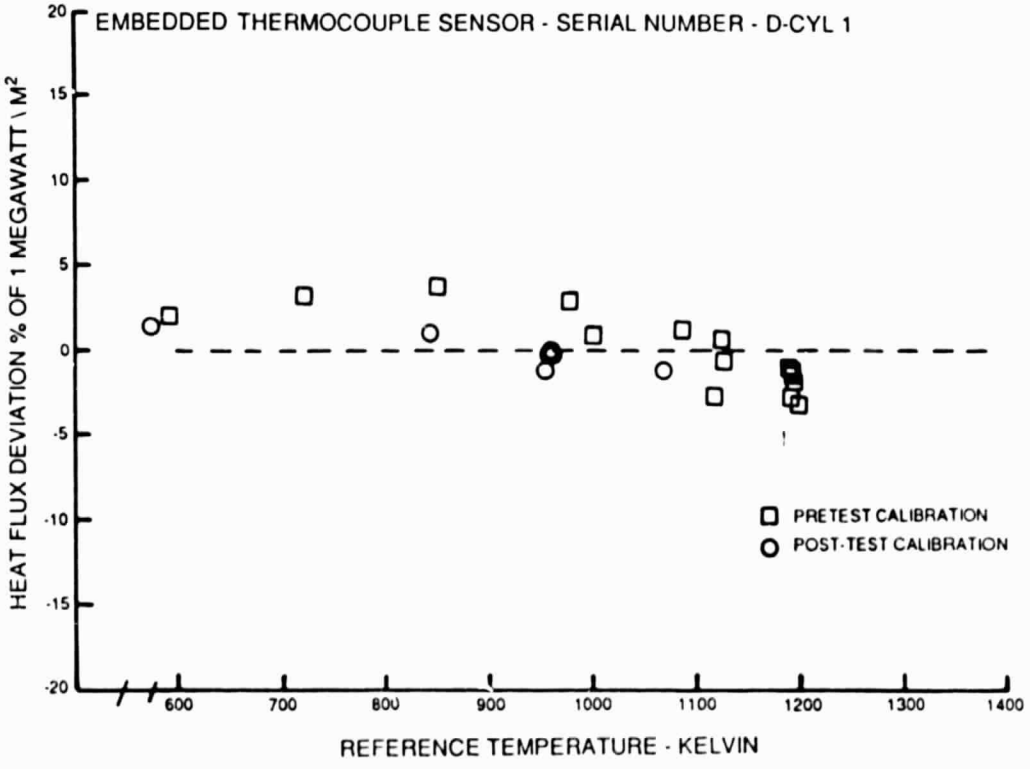

Figure 72b Post Test Calibration of Embedded Thermocouple Sensor in Cylinder 1

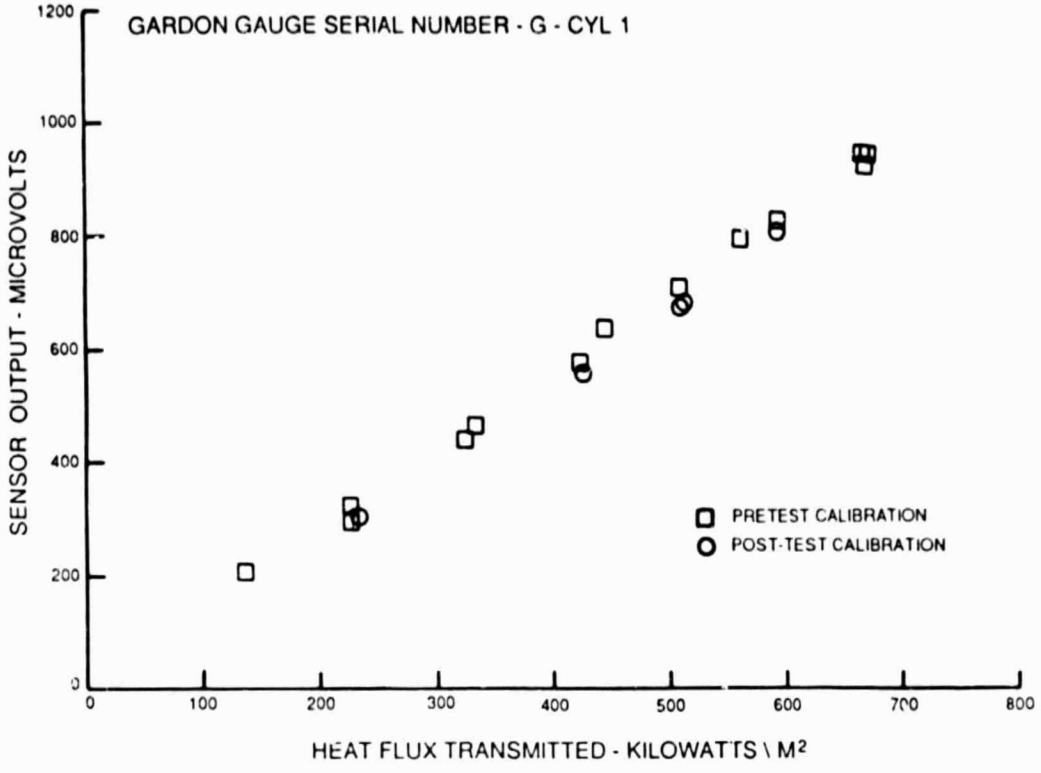

Figure 73a Post Test Calibration of Gardon Gauge Sensor in Cylinder 1

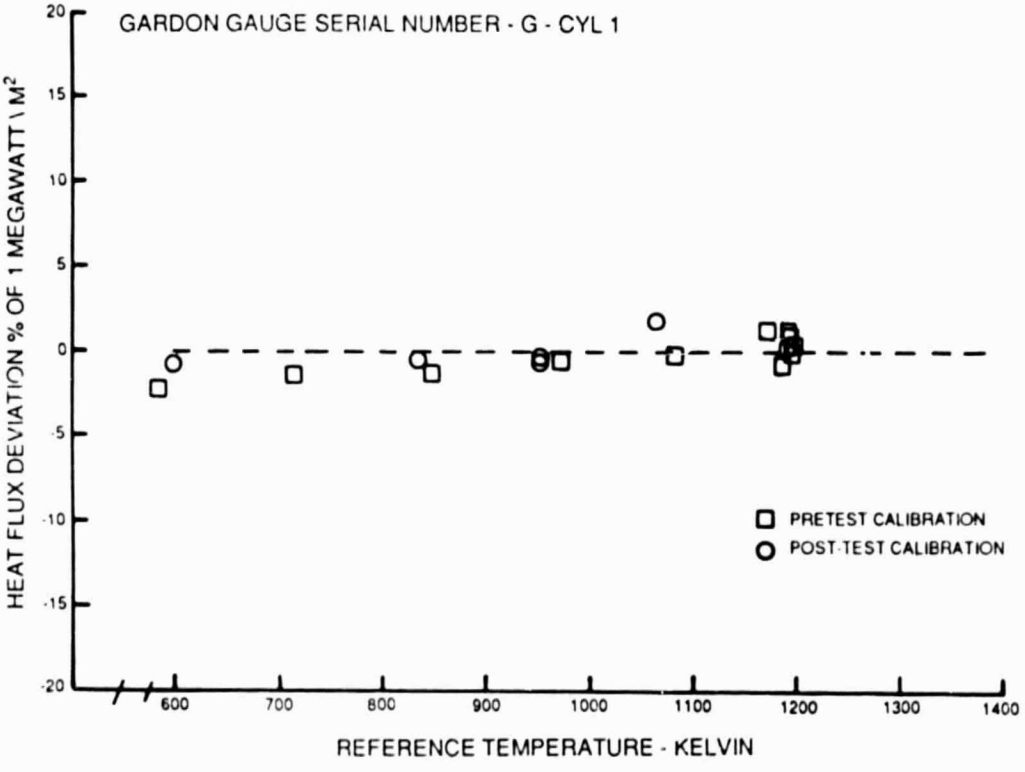

Figure 73b Post Test Calibration of Gardon Gauge Sensor in Cylinder 1

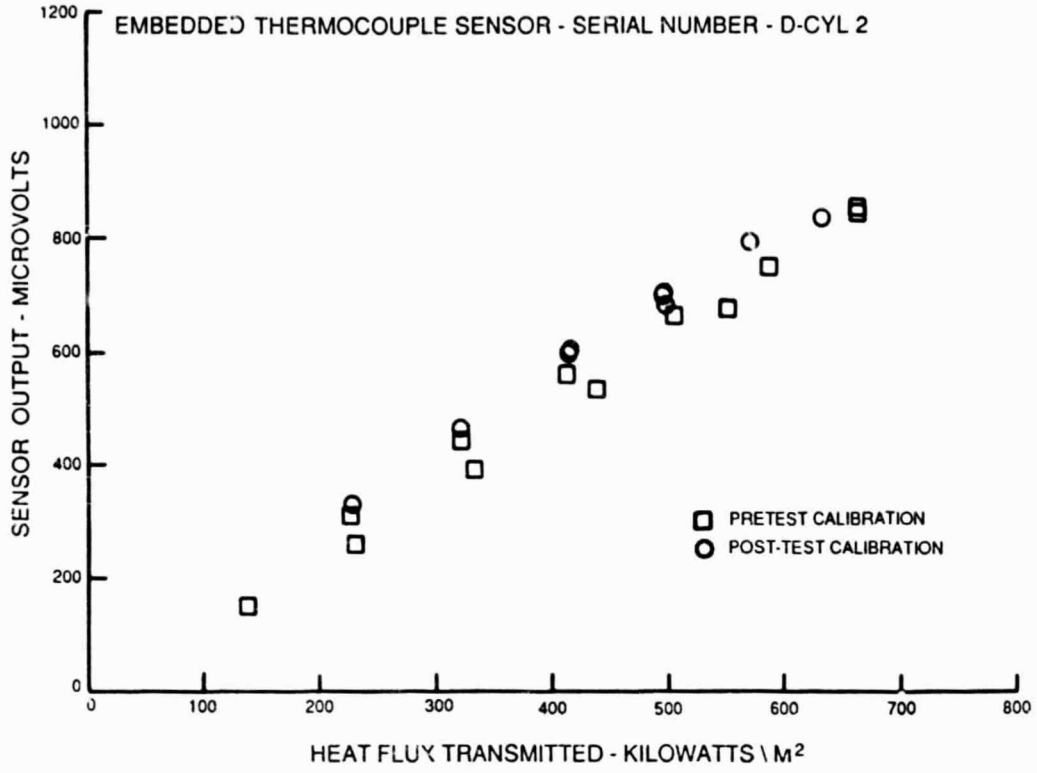

Figure 74a Post Test Calibration of Embedded Thermocouple Sensor in Cylinder 2

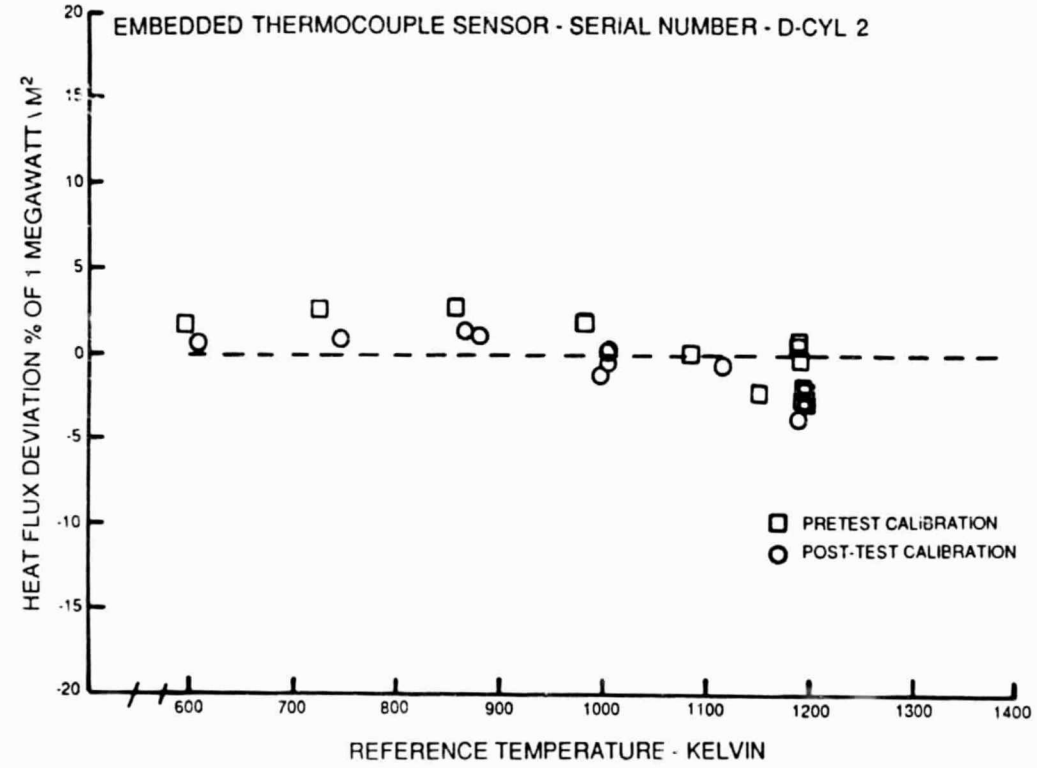

Figure 74b Post Test Calibration of Embedded Thermocouple Sensor in Cylinder 2

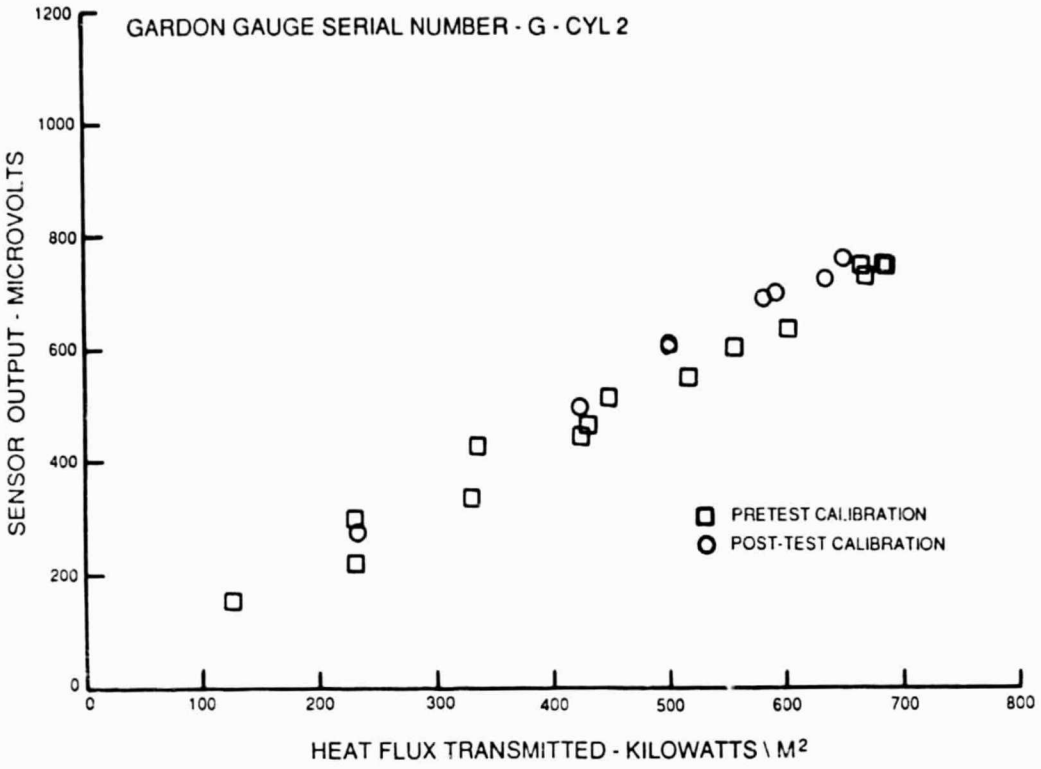

Figure 75a Post Test Calibration of Gardon Gauge Sensor in Cylinder 2

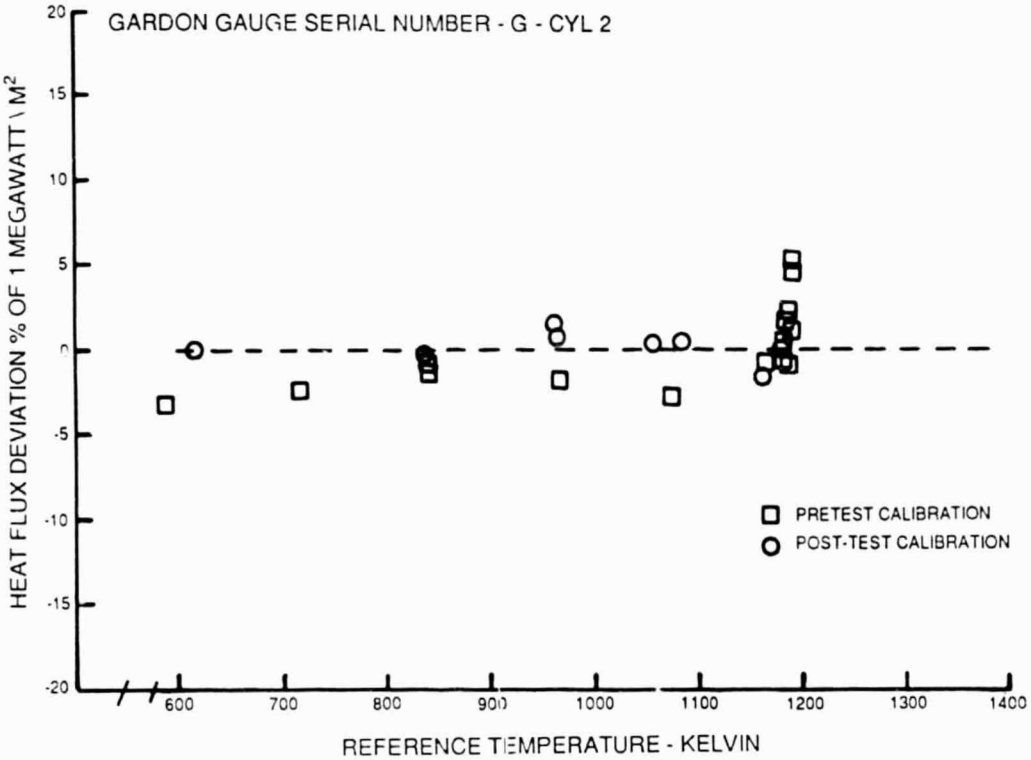

Figure 75b Post Test Calibration of Gardon Gauge Sensor in Cylinder 2

Figures 76 through 80 show comparisons of the heat transfer coefficient data shown earlier with the theoretical results. The plots show the ratio of the experimentally obtained heat transfer coefficient and the theoretical result vs Mach number. Data from all five plots show the same general trends. Figures 79 and 80 contain the data where the stagnation point angular orientation was carefully monitored. For that data, the two embedded thermocouple sensors and the Gardon gauge on cylinder 1 yielded heat transfer coefficients 45% to 65% higher than the nonturbulent theoretical results. The Gardon gauge on cylinder 2 and all transient sensors yielded data 10% to 30% higher than the nonturbulent theoretical results. Figure 81 from reference 7 shows data and theoretical results from a number of sources showing the effect of turbulence on the heat transfer to the stagnation point of a cylinder in cross flow. If we assume 10% turbulence, based on the NASA LDV data, the parameter $T_u R_e^{1/2}$ had values over the range 17 to 23 for these cylinder in cross flow tests. Based on Figure 81, we would expect the experimental heat transfer coefficient to be higher than the theoretical nonturbulent value by 40-60%. This is in good agreement with the data from the two embedded thermocouple sensors and the Gardon gauge on cylinder 1.

Over the front 70 degrees of a cylinder, the heat transfer at any angle Θ can be calculated quite accurately (Reference 30) as:

$$h_\Theta = h_\sigma \left[1 - \left(\frac{\Theta}{90}\right)^3\right]$$

where:

Θ = angle from stagnation point
$h\sigma$ = stagnation point heat transfer coefficient
$h\Theta$ = heat transfer coefficient at angle

Figure 82 shows the variation in heat transfer coefficient measured by the embedded thermocouple sensor on cylinder 2 as it was rotated. Also shown is the curve predicting the change in heat transfer coefficient with angle, based on the above equation, with h set equal to the experimentally measured result. It can be seen that within 70 degrees of the stagnation point. the shape of the experimental curve agrees very well with the theoretical results.

Figure 83 shows a comparison of the rotational data from the embedded thermocouple sensor on cylinder 1 with similar data taken elsewhere (Reference 30). The shape of the curves is much as one would expect. Over the front half of the cylinder, the current heat flux data taken at Reynolds Numbers of approximately 40,000 looks much like the data from the literature at Re = 70,000. Across the back of the cylinder, the current data is significantly lower. That probably is because the free stream turbulence has the most effect augmenting the heat transfer on the front of the cylinder where the boundary layer is laminar. Beyond the separation point, considerable turbulence will always exist over the rear of the cylinder so the additional free stream turbulence will have little effect.

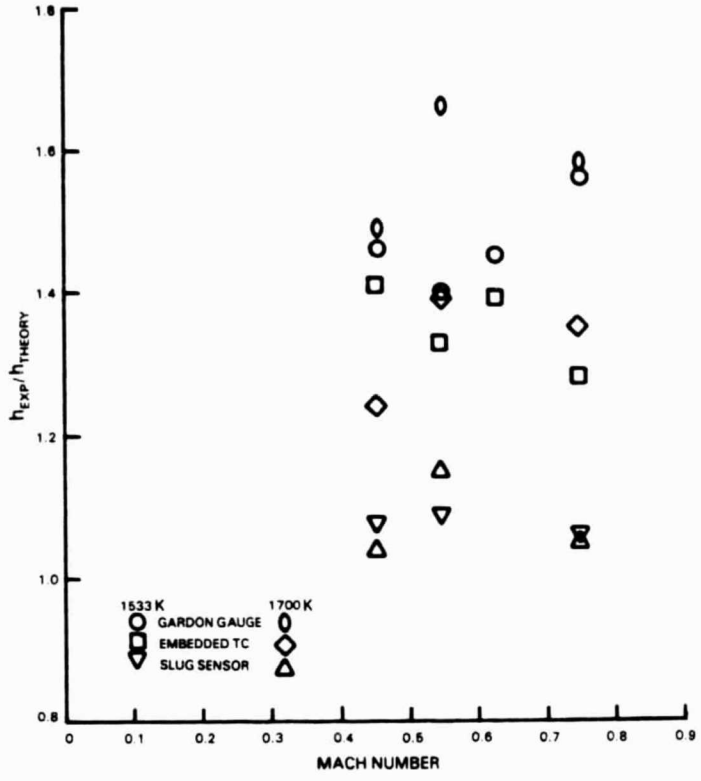

Figure 76 Comparison of Results from Cylinder 1 With Theoretical Results for Non-Turbulent Flow

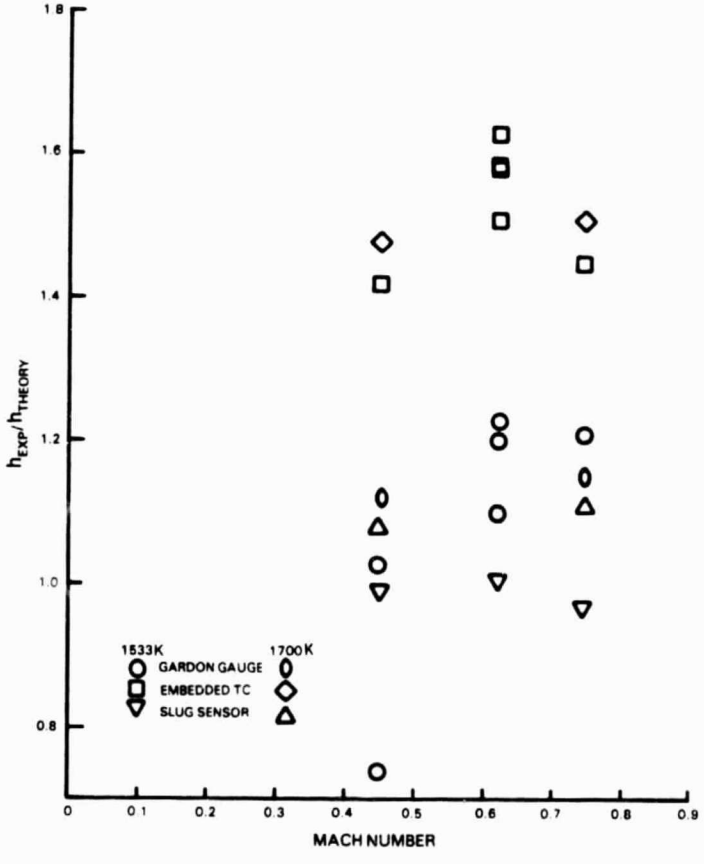

Figure 77 Comparison of Results from Cylinder 2 With Theoretical Results for Non-Turbulent Flow

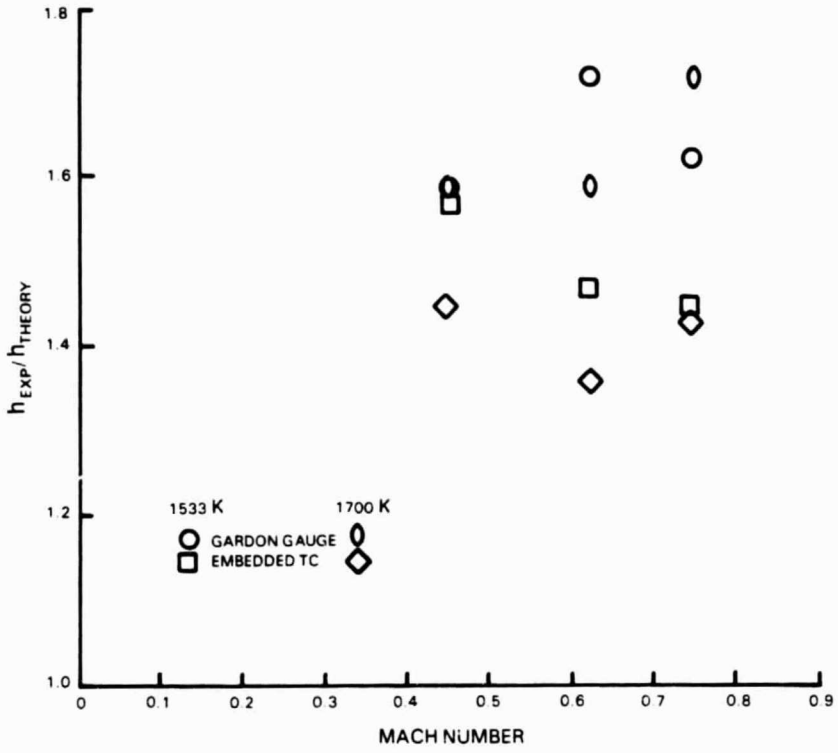

Figure 78 Comparison of Results from Rerun of Cylinder 1 With Theoretical Results for Non-Turbulent Flow

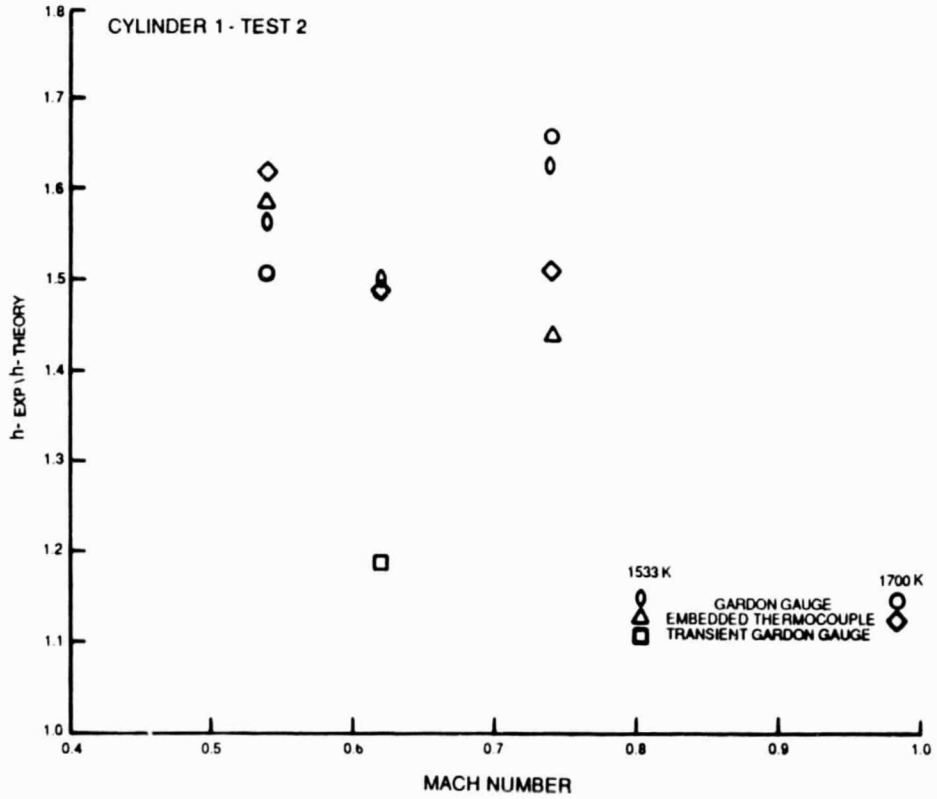

Figure 79 Comparison of Results from Cylinder 1 - Second Test Series with Theoretical Results for Non-Turbulent Flow

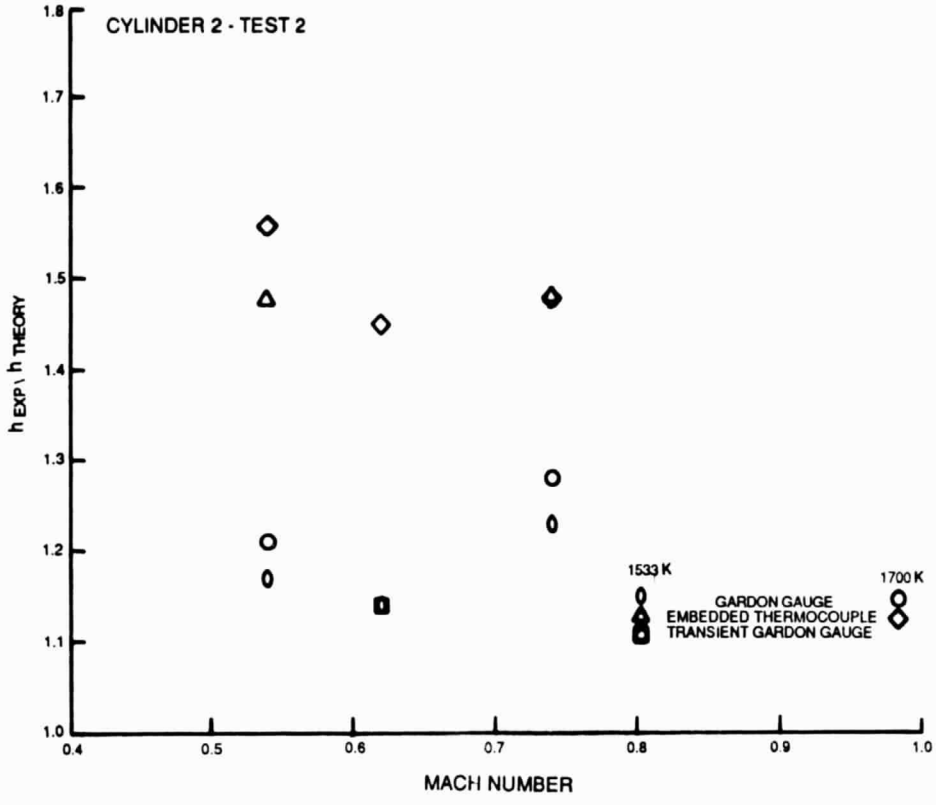

Figure 80 Comparison of Results from Cylinder 2 - Second Test Series with Theoretical Results for Non-Turbulent Flow

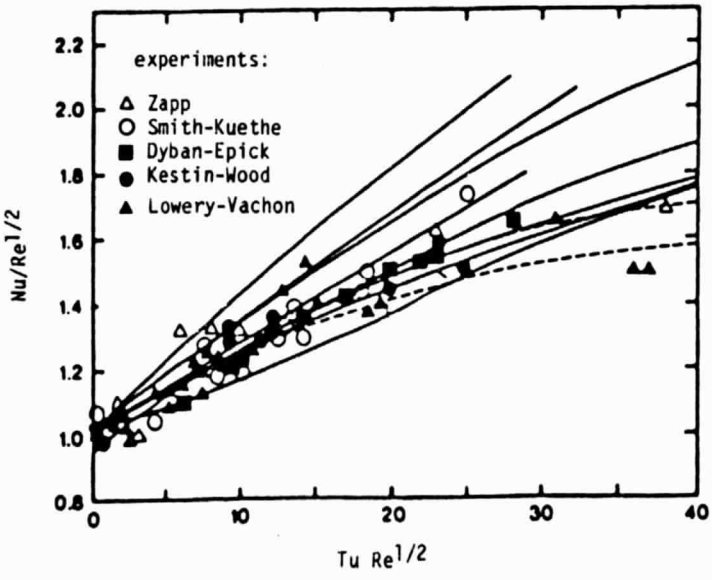

Figure 81 Effect of Turbulence on Heat Transfer To Stagnation Point of Cylinder in Cross Flow Adapted from Reference 7

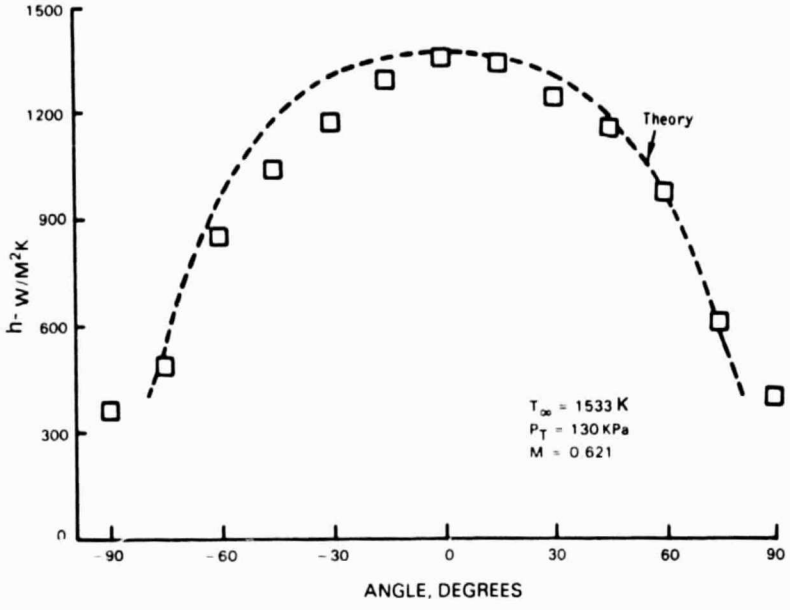

Figure 82 Comparison of Variation In Heat Flux with Rotation Measured by the Embedded Thermocouple Sensor in Cylinder 2 and Predicted by Theory

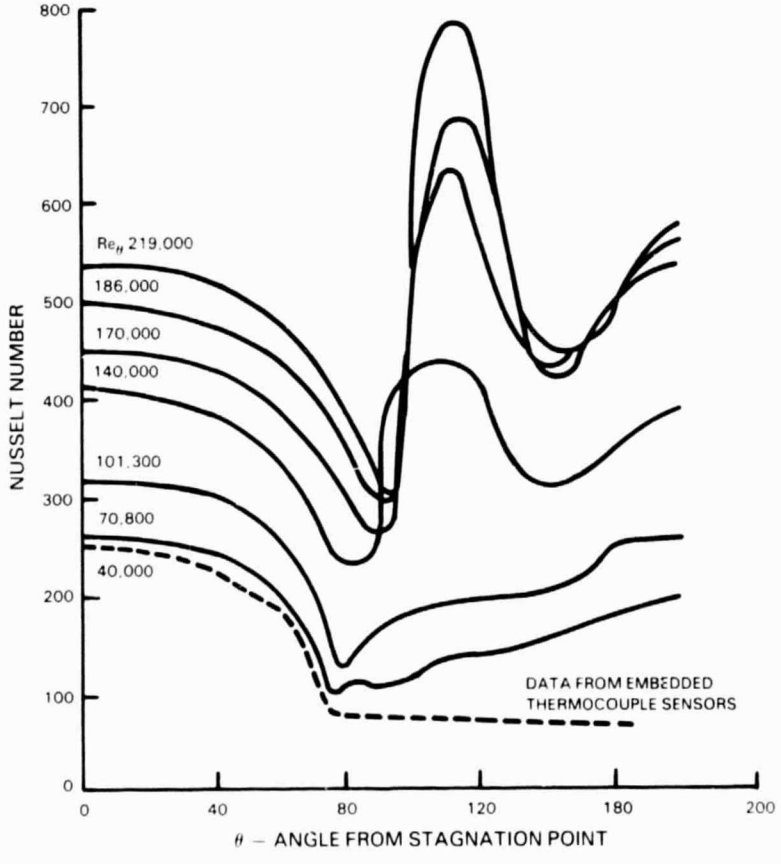

Figure 83 Comparison of Rotation Data Measured by Embedded Thermocouple Sensor in Cylinder 1 With Other Data From The Literature

ADDITIONAL LABORATORY TESTS

In order to investigate the strange data obtained when rotating the Gardon gauge sensors and the unrealistically high data obtained from the sputtered thermocouple sensor, additional laboratory tests were conducted. Rotation tests were conducted in the quartz lamp bank calibration facility. The variation in heat flux with angle in the quartz lamp bank facility is not exactly the same as it was in the cylinder in cross flow test, but the profiles are qualitatively similar. Initially, an embedded thermocouple sensor was installed in front of the quartz lamp bank. After stable conditions were reached, data were taken at every 15 degrees of rotation. The output, shown in Figure 84, looks as expected. The highest value is at 0 degrees with the sensor directly facing the lamp. Minimum output is near 180 degrees and the curve is symmetric about the axis of symmetry of the rig.

The same test procedure was used with the Gardon gauge sensors. The results are shown in Figure 85. These calibration rig tests yielded the same type of mirror image, nonsymmetical, sinusoidal curves observed during the cylinder in cross flow tests. This confirms that the strange behavior observed from the Gardon gauges during the cylinder in cross flow tests is due to the Gardon gauge design and not the cylinder in cross flow rig.

The hot end of the surviving sputtered thermocouple probe was placed in a laboratory oven and the resistance to ground of the sputtered film was monitored as the probe was heated. The results are shown in Figure 86. While the film was well off ground (9 megohms) at room temperature, the resistance to ground decreased to 300 ohms at 950K. This is comparable to the loop resistance of the sputtered film so the thermocouple was, in effect, directly shorted to ground at high temperature. Based on these results, there appears to be several possible explanations for the unrealistically high sputtered thermocouple readings during the cylinder in cross flow tests. One possible explanation is that when the sputtered thermocouple was heated and shorted to ground during the test, ground loops occurred that would not have been in existence during the various system checks when the sputtered thermocouple was cold and, therefore, insulated from ground. These ground loops could introduce a high level of noise into the sputtered thermocouple signal. Other possibilities include nonsteady secondary junction between the sputtered film and the base material, noise produced by vibration of the leadwire attachment to the sputtered films, and catalytic reactions between the noble metal films and the incomplete combustion products.

FINITE DIFFERENCES CALCULATIONS

Figure 87 shows a schematic of the Gardon gauge sensor. In all cases wire A is Alumel. Wires B and C are one Chromel and one Alumel. It is believed that in cylinder 1 wire B was Chromel and wire C was Alumel while in cylinder 2 wire B was Alumel and wire C was Chromel. In that case, if the ceramic in the Gardon gauge cavity acted as a thermal barrier, that barrier could be the cause of the mirror image S shaped curves obtained when the cylinders were rotated.

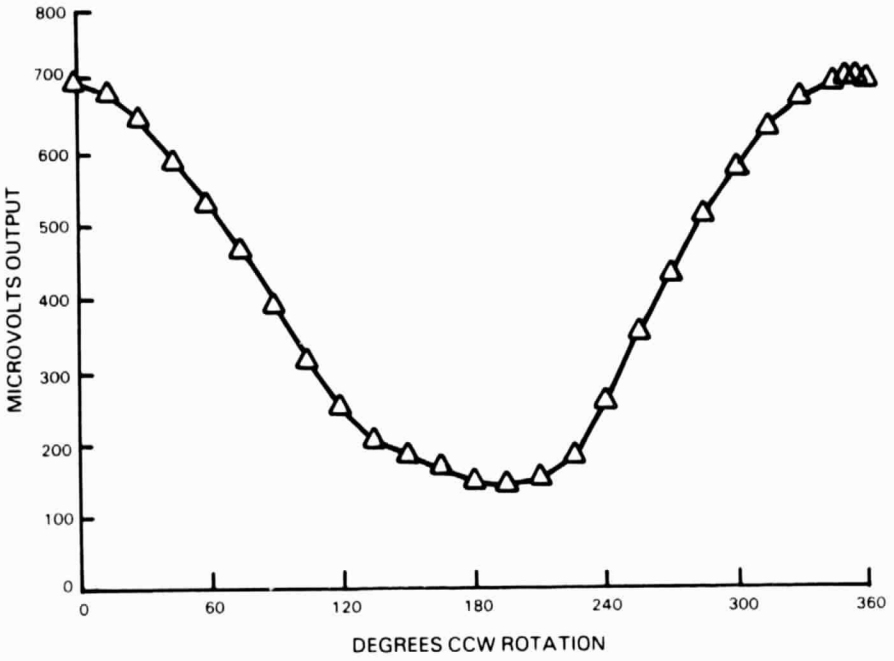

Figure 84 Data from Rotation of Embedded Thermocouple Sensor in Cylinder 2 in the Calibration Rig

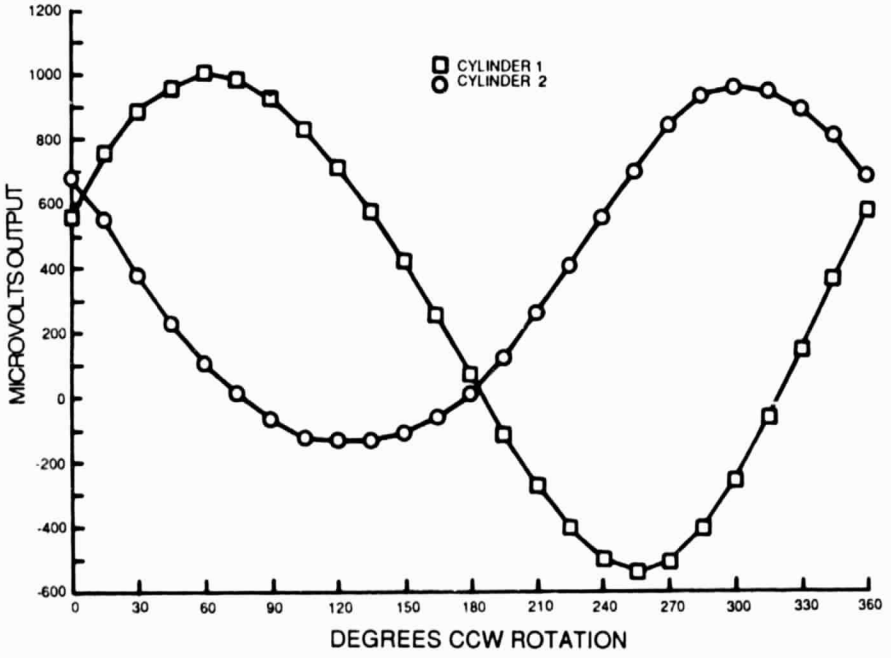

Figure 85 Data From Rotation of the Gardon Gauge Sensors in the Calibration Rig

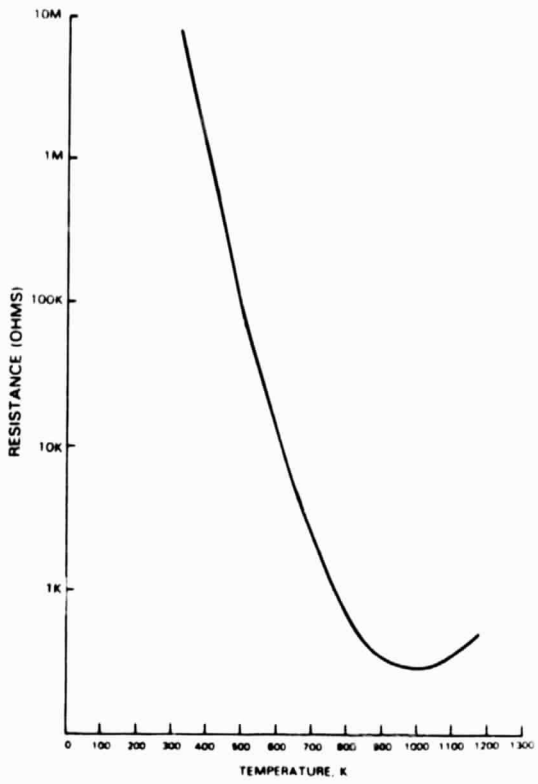

Figure 86 Resistance to Ground Results for Sputtered Thermocouple Sensors When Heated

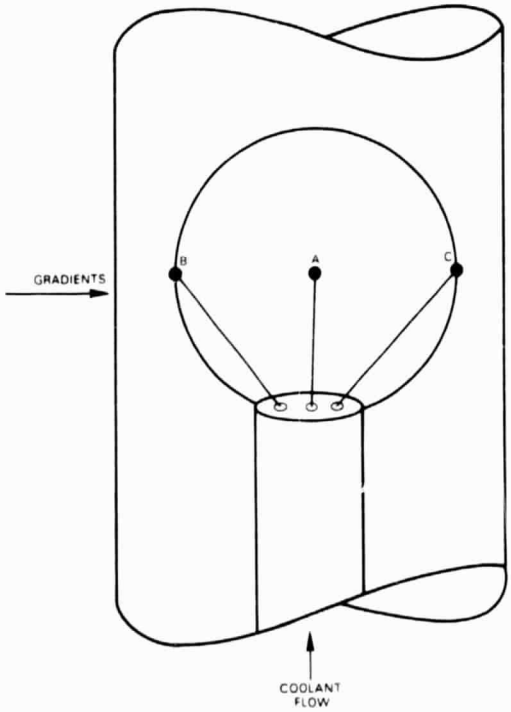

Figure 87 Schematic of Gardon Gauge Sensor

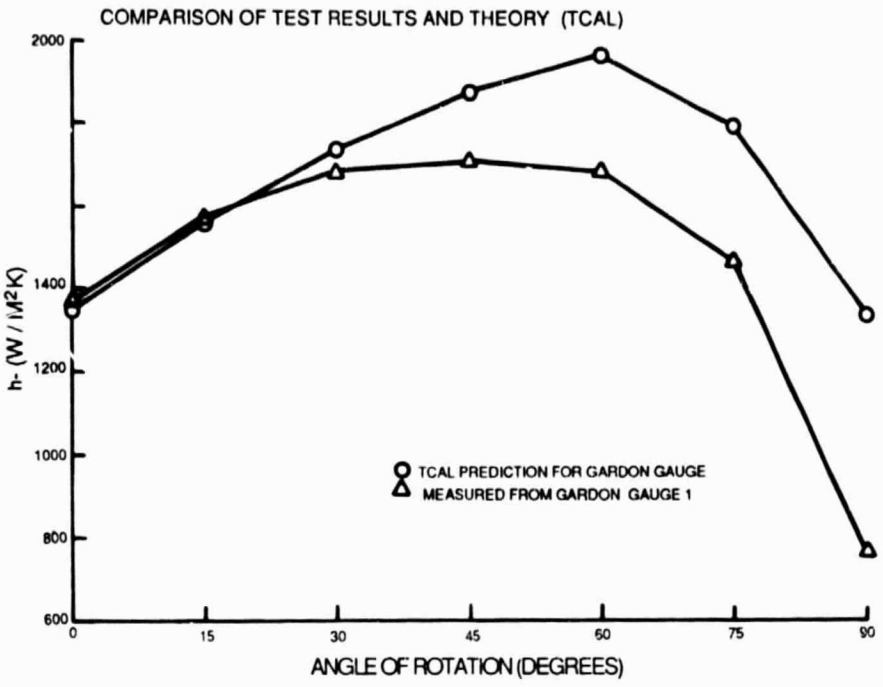

Figure 88 Comparison of Test Results with TCAL Calculated Results for the Gardon Gauge in Cylinder 1

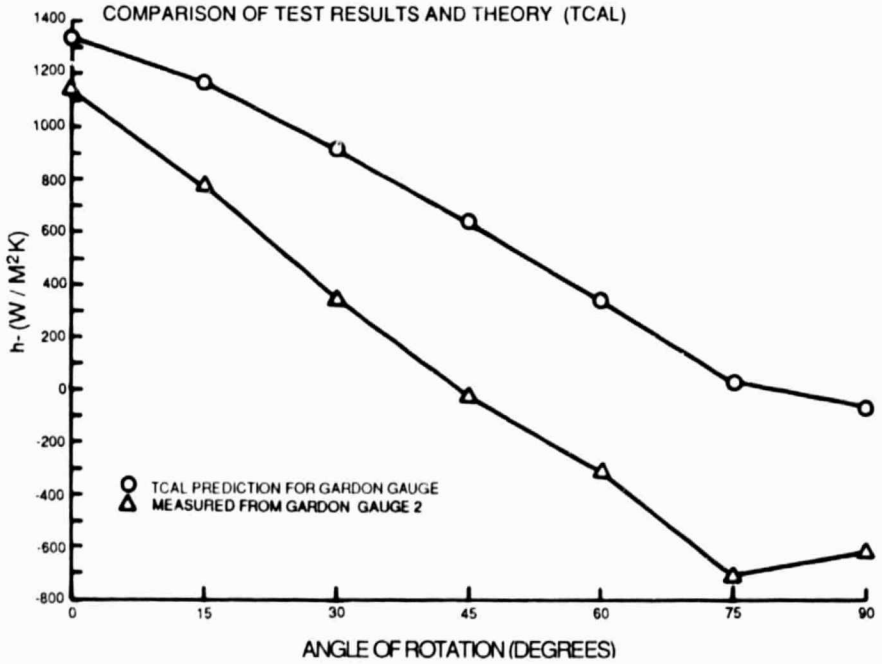

Figure 89 Comparison of Test Results with TCAL Calculated Results for the Gardon Gauge in Cylinder 2

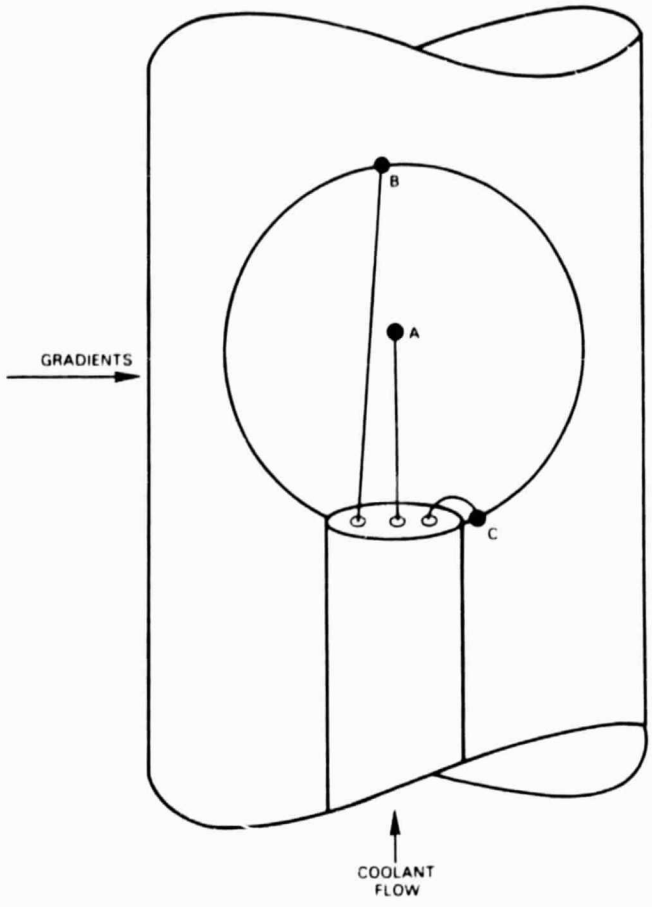

Figure 90 Schematic of Modified Gardon Gauge Sensor

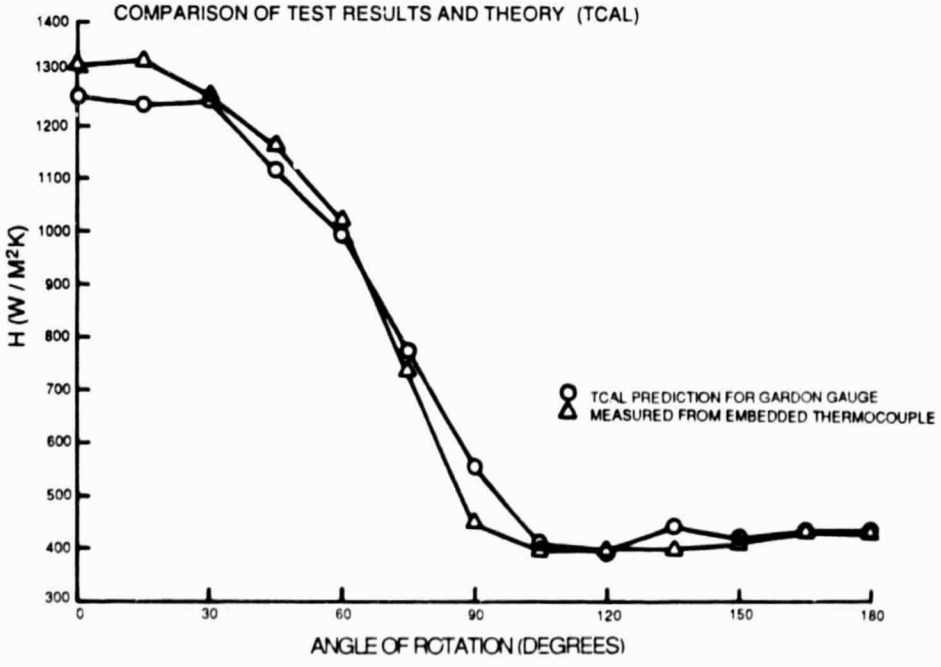

Figure 91 Comparison of Test Results from the Embedded Thermocouple Sensor with TCAL Predicted Results for the Modified Gardon Gauge Sensor

To investigate this possibility, a set of calculations was performed using the Pratt & Whitney temperature calculation computer program (TCAL). TCAL is a three dimensional finite difference calculation routine that provides for variations in input geometries, materials, and boundary conditions. The program was used to predict the effect of rotation on heat transfer results from the Gardon gauge sensors. The cool side heat transfer coefficient was held constant. For the hot side boundary condition, the heat transfer coefficients measured by the embedded thermocouple sensors (Figure 55) was used. Figures 88 and 89 show a comparison of the predicted TCAL results withthe test results obtained earlier. The TCAL of predictions are in good qualitative agreement with the actual test data. Thermal blockage by the ceramic in the Gardon gauge can clearly cause problems in areas with steep thermal gradients. In retrospect, it would have been wiser to have built the Gardon gauge as shown in Figure 90. In this configuration, the leads are perpendicular to the thermal gradient rather than parallel to it. The TCAL program was used to predict the results that would be obtained from this configuration. This predicted result is compared with the data that was measured with the embedded thermocouple sensor in Figure 91. These are in excellent agreement.

SECTION 10.0
CONCLUSIONS AND RECOMMENDATIONS

The transient and steady state measurements of the heat transfer coefficient at the stagnation point of the cylinders were consistent and in reasonable agreement with theory. The measured values were up to 70% higher than theoretical values for zero turbulence. This would be anticipated from the approximately 10% turbulence observed in the airstream by the LDV measurements. There were systematic biases between the sensors. The results from the two embedded thermocouple sensors and one Gardon gauge yielded results in good agreement with other studies of cylinders in cross flow. The other Gardon gauge and all the transient sensors gave heat transfer coefficients lower than expected. The cause of those results is unknown. On repeat runs, the sensors produced values that repeated within 10%. This scatter can be explained partially by sensitivity to positioning in the airstream which changes the non-one-directional flow characteristics. Post test calibrations of the sensors agreed to within 3% of the pretest results, indicating that the sensor outputs were stable and that the test program environmental conditions did not cause shifts in the sensor outputs. The heat transfer coefficients calculated from the sputtered thermocouple and dynamic gas temperature data were high by orders of magnitude. Examination of the data revealed that the sputtered thermocouple temperature fluctuations were much greater than anticipated. This could be caused either by ground loops resulting from the sputtered thermocouple shorting to ground when it was heated or from other factor such as intermittent secondary junctions. The durability of the sputtered thermocouples was very poor on these cylinders and sufficient test data could not be obtained to fully characterize the exact problems.

In light of the experience gained from this test program, the following recommendations are offered:

1. The use of the sensors developed during Phase I of this contract should be limited to areas on the airfoil that approximate flat plate geometries and where temperature gradients are minimal. In these situations the sensors will yield valid results.

2. If measurements must be made in areas with moderate thermal gradients, embedded thermocouple heat flux sensors should be used. Where the direction of the gradient is known the Gardon gauges should be fabricated with the leadwires attached perpendicular to the direction of the gradient.

3. Methods of calibrating heat flux sensors in areas with sharp curvature and large temperature gradients should be developed. These methods may consist of either imposing a known gradient during calibration or using an analytical correction applied to the data to account for the temperature gradients. This is necessary for measurements in the leading edge area of airfoils and in areas adjacent to internal ribs or heat transfer augmentation structures.

4. The durability of the sputtered thermocouples should be improved and a test program conducted to evaluate the use of sputtered sensors within a flame.

APPENDIX A

I. Cylinder-in-Crossflow References

1. Almostino, D., McAlister, K. W.; "Water-Tunnel Study of Transition Flow Around Circular Cylinders"; NASA Technical Memorandum 85879, 1984.

2. Boulos, M. I.; Pei, D.C.T.; "Dynamics of Heat Transfer from Cylinders in a Turbulent Air Stream"; International Journal of Heat and Mass Transfer; Vol. 17, pp. 767.

3. Brunson, F. W.; "Local Heat Transfer Coefficients Around a Cylinder in Oscillating Flow"; Naval Post Graduate School, Monterey, CA, Dec., 1981.

4. Dils, R. R.; Follansbee, P. S.; "Heat Transfer Coefficients Around Cylinders in Crossflow in Combustor Exhaust Cases"; ASME paper 77-GT-9.

5. Frossling, N.; "Verdunstrung Warmeubertragung und Geschwindigkeitsverteilung bei zweidimensionaler und Rotations - symmetrischer Grenzschichlstromung"; 1940.

6. George, M. C ; "High Reynolds Number Cylinder Flow Studies"; Office of Naval Research under Contract N00014-81-K-0479, Jan. 10, 1983.

7. Gorla, R. S. R.; Nemeth, N., "Effects of Free Stream Turbulence Intensity and Integral Length Scale on Heat Transfer From a Cylinder in Crossflow". Heat Transfer 1982; Proceedings of Seventh International Conference; Muniek West Germany; September 6-10, 1982; Volume 3.

8. Hijikata, K.; Yoshida, H.; Mori, Y.; "Theoretical and Experimental Study of Turbulence Effects on Heat Transfer Around the Stagnation Point of a Cylinder". Heat Transfer 1982, Proceedings of Seventh International Conference; Muniek West Germany; September 6-10, 1982, Volume 3.

9. Kestin, J.; Maeder, P. F.; "Influence of Turbulence on Transfer of Heat from Cylinders"; NASA Paper TN4018; October, 1957.

10. Kestin, J.; Maeder, P. F.; Sogin, H. H.; "The Influence of Turbulence on the Transfer of Heat to Cylinders near the Stagnation Point", Zectschrift Fuer Augew Andte Mathematik und Physik; Vol. 12; 1961, pp. 115.

11. Nagamatsu, H. T., Duffy, R. E.; "Investigation of the Effects of Pressure Gradient, Temperature and Wall Temperature Ratio on the Stagnation Point Heat Transfer for Circular Clyinders and Gas Turbine Vanes"; NASA CR-174667; April, 1984.

12. Ota, T.; Kon, N.; Hatakeyama, S.; Sato, S.; "Measurements of Turbulent Shear Stress and Heat Flux in an Axisymmetric Separated and Re-attached Flow over a Longitudinal Blunt Circular Cylinder". Bulletin of JSME; Vol. 23, No. 184; October, 1980.

13. Remy, N.; Martin, M.; "Influence Sur le Transient de Chaleur en Ecoulement Pulse d'une ailette place sur la generatrice l'arret amount d'une cylindre"; Comptes Rendus Acadamie des Science; October 14, 1974.

14. Rodriguez, O.; "The Circular Clylinder in Subsonic and Transonic Flow"; AIAA Journal Vol. 22, No. 12, December 1984.

15. Sadeh, W. Z.; Saharon, D. B.; "Turbulence Effect on Crossflow Around a Circular Cylinder at Subcritical Reynolds Number"; NASA Contractor Report 3622, 1982.

16. Seban, R. A.; "The Influence of Free Stream Turbulence on the Local Heat Transfer from Cylinders"; Journal of Heat Transfer; May, 1960; pp. 101.

17. Shih, W. C. L.; "High Reynolds Number Cylinder Flow Workshop"; Final Report to Office of Naval Research Under Contract N00014-79-C-0893; August 17, 1981.

18. Stepka, F. S.; Gaugler, R. E.; "Comparison of Predicted and Experimental External Heat Transfer Around a Film Cooled Cylinder in Crossflow"; ASME Paper 83-GT-47.

19. Van Der Hegge Zijnen, B. G.; "Heat Transfer from Horizontal Cylinders to a Turbulent Air Flow"; Applied Science Research. Applied Scientific Research; Vol. 7; Section A; August, 1957.

20. Wang, C. R.; "Turbulence and Surface Heat Transfer Near the Stagnation Point of a Circular Cylinder in Turbulent Flow"; NASA-TM-83732; 1983.

II Miscellaneous References

21. Atkinson, W. H.; Strange R. R.; "Development of Advanced High Temperature Heat Flux Sensors"; NASA CR-165618 NASA Lewis Research Center; September 1982.

22. Atkinson, W. H.; Cyr, M. A.; Strange R. R.; "Turbine Blade and Vane Heat Flux Sensor Development Phase 1 - Final Report"; NASA CR-168297; NASA Lewis Research Center; August 1984.

23. Blair, M. F.; "Influence of Free-Stream Turbulence on Turbulent Boundary Layer Heat Transfer and Mean Profile Development - Part II Analysis and Results"; Journal of Heat Transfer, February, 1983; Vol. 105; P. 41

24. Dils R.; Follansbee P.; "Wide Bandwith Gas Temperature Measurements in Combustor and Combustor Exhaust Gases"; ISA 1975

25. Elmore, D; "Dynamic Gas Temperature Measurement System", Turbine Engine Hot Section Technology, NASA TM 83022, 1982.

26. Gaugler, R. E.; Russell, L. M.; "Flow Visualization Study of The Horseshoe Vortex in a Turbine Stator Cascade", NASA Tech Paper 1884, June, 1982.

27. Grant, H. P.: Przybyszewski, J.S; Claing, R.G.; "Turbine Blade Temperature Measurements Using Thin Film Temperature Sensors", NASA CR-165201; March 1981.

28. Jansen, B. J., Jr.; Mueller, T. J.; "Experimental Studies of the Boundary Layer on an Airfoil at Low Reynolds Numbers"; AIAA 16th Fluid and Plasma Dynamics Conference; July 12-14, 1983; Danvers, MA

29. Keenan J. H., Kaye, Gas Tables , J. Wiley 1961.

30. Kreith F.; Principles of Heat Transfer; 1964

31. Krishnamoorthy, V.; "Effect of Turbulence on the Heat Transfer in a Laminar and Turbulent Boundary Layer Over A Gas Turbine Blade"; ASME Paper 82-GT-146.

32. Luckey, D. W.; L'ecuyer, M. R.; "Stagnation Region Gas Film Cooling - Spanwise Angled Injection from Multiple Row of Holes"; NASA Contracts Report 165333; April, 1981.

33. Miles, J. H.; Wasserbauer, C. A.; Krejsa, E. A.; "Cross Spectra Between Temperature and Pressure in a Constant Area Duct Downstream of a Combustor"; NASA Technical Memorandum 83351 Lewis Research Center; April, 1983.

34. Wannenwetsch, G.; "Experimental Investigation of Discrete Heat Transfer Measurement Techniques for Tunnel A Applications"; Arnold Engineering Development Center; July, 1981.

35. Woo, Y. K.; "Transient Heat Transfer Measurement Technique in Wind Tunnel and Data Analysis Technique Using System Identification Theory"; Thesis presented to Air Force Institute of Technology; December, 1982.